UNIVERSIDAD DE EXTREMADURA

Método de estimación de las pérdidas de los conductores y del núcleo de componentes inductivos asimétricos mediante la técnica de análisis por método de elementos finitos en 3D

Jorge Rafael González Teodoro

2020

UNIVERSIDAD DE EXTREMADURA

Método de estimación de las pérdidas de los conductores y del núcleo de componentes inductivos asimétricos mediante la técnica de análisis por método de elementos finitos en 3D

Jorge Rafael González Teodoro

La conformidad de los directores de la tesis consta en el original en papel de esta Tesis Doctoral

Dr. Enrique Romero Cadaval
Departamento de Ingeniería eléctrica, electrónica y automática
(Universidad de Extremadura)

Dr. Rafael Asensi Orosa
Departamento de Automática, Ingeniería Eléctrica y Electrónica e Informática Industrial
(Universidad Politécnica de Madrid)

2020

Patricia y Víctor
Luz de mi alma
Camino de mi esperanza

Abstract

In electrical engineering, power converters, as devices that are able to transform a defined current and voltage from an energy source, have a critical role in different fields as renewable energy, electric vehicles or aerospace engineering.

The magnetic components are relevant elements in power converters because determines the current filtering and conversion functions and converter efficiency and performance. One of the critical parameters that influence in the efficiency of converters are the losses in the magnetic components that depends on particular effects as they are the skin, proximity, air-gap and edge effects. These effects are more relevant in the high frequency ranges where the power converters are usually operated.

The optimization of the power converter requires of the detailed analysis of the magnetic component and the involved frequency effects according to the application when particular requirements are needed, mostly in the medium and high frequency.

Transmission, storage and losses of magnetic and electric energy analysis is relevant in this context and are determined by the Maxwell´s equations whose resolution is a complex task. There are three main methods to solve this equation system: analytical method, finite element method analysis and experimental methodology.

The first method consists on the analytical resolution of the equations with the necessary simplifications, being the most common approach the assumption of the magnetic field distribution in one or two dimensions to solve the equations system, however this simplification does not allow determining the magnetic field into the conductors.

The second approach uses the Finite Element Method, solving the Maxwell equations in every finite element of the component, but is not possible to simulate some complex magnetic components because it requires a high computational time, being not useful for power electronics designers.

The third method, based on experimental lab tests, allows to obtain the electrical parameters for any magnetic component. Nevertheless, the time cost is also huge and it is only used for adjustments in the final stage.

Most of the power electronics designers and scientists use the analysis of the magnetic components based on Finite Element Method doing the available simplification taking into account the magnetic field distribution and the symmetry of the magnetic component.

If the magnetic component has not any symmetric, a 3D model is necessary to determine the electromagnetic or thermal parameters for the electrical equivalent circuit and the magnetic

component optimization, as well as a detailed study for skin effect and proximity effect, even more if the magnetic components work at high frequency.

In this work, it is proposed a new method based in 3D Finite Element Analysis with a low computational time that allows obtaining the electrical equivalent model parameters for asymmetric magnetic components from the estimation of winding and core power losses.

Resumen

Dentro del campo de la ingeniería eléctrica, los convertidores electrónicos de potencia, que permiten generar una tensión y corriente de unas determinadas características a partir de una fuente de energía, juegan un papel crítico en las energías renovables, vehículos eléctricos o la ingeniería aeroespacial.

Los componentes magnéticos constituyen uno de los elementos esenciales en los convertidores de potencia determinando el filtrado de corriente, la operación y la eficiencia del convertidor. Uno de los parámetros más críticos que influyen en la eficiencia de los convertidores son las pérdidas de los componentes magnéticos que dependen de determinados efectos electromagnéticos como el efecto pelicular, de proximidad, de entre-hierros y de borde. Estos efectos son aún más relevantes en rangos de alta frecuencia, a la que suelen operar habitualmente los convertidores electrónicos de potencia.

La optimización del convertidor de potencia requiere un análisis detallado de los componentes magnéticos y de los efectos de frecuencia producidos en función de cada aplicación particular, y sus requisitos específicos, principalmente en los rangos de media y alta frecuencia.

La trasmisión, almacenamiento y pérdidas de energía eléctrica y magnética son relevantes en este contexto y están determinadas por las ecuaciones de Maxwell, cuya resolución es compleja. Existen tres importantes enfoques para la resolución de estas ecuaciones: métodos analíticos, análisis utilizando herramienta de elementos finitos y por realización de ensayos.

El primero de ellos consiste en la resolución analítica de las ecuaciones, con las necesarias simplificaciones, siendo la más habitual el asumir simetrías en las distribuciones de los campos magnéticos para poder resolver las ecuaciones de Maxwell en una o dos dimensiones. Como desventaja, dicha simplificación no permite determinar la distribución del campo magnético dentro de los conductores.

El segundo enfoque utiliza un método de elementos finitos, resolviendo las ecuaciones de Maxwell en cada elemento finito, no siendo posible simular algunos componentes magnéticos complejos por precisar un tiempo de simulación sea muy elevado, haciendo que esta solución no resulte práctica para los ingenieros de desarrollo.

El tercer enfoque, basado en la realización de ensayos de laboratorio, permite obtener los parámetros eléctrico de cualquier componente magnético. No obstante, el tiempo necesario es también alto y sólo es usado para los ajustes finales.

La mayoría de los ingenieros electrónicos y científicos usan los análisis basados en elementos finitos de los componentes magnéticos realizando las posibles simplificaciones teniendo en cuenta la distribución de campo magnético y la simétrica del componente.

Cuando el componente magnético no presenta ninguna simetría, deben utilizarse modelos 3D para la determinación de sus parámetros del circuito eléctrico equivalente y la optimización magnética del componente, así como un detallado estudio de los efectos pelicular y de proximidad, que son especialmente relevantes cuando el componente trabaja en alta frecuencia.

En este trabajo, se proponer una metodología basada en elementos finitos en 3D con un bajo tiempo de simulación que permite obtener los parámetros que del modelo eléctrico equivalente para componentes magnéticos asimétricos a partir de la estimación de las pérdidas del bobinado y del núcleo.

THESIS INDEX

ACKNOWLEDGMENTS

THE LIST OF SYMBOLS

μ_o	Vacuum Permeability
μ_r	Relativity Permeability
μ_e	Effective Permeability of equivalent toroid of magnetic core of the model component
I_{eff}	Effective Current
V	Voltage
$\emptyset$	Magnetic Flux
Re	Real part of the vector
Im	Imaginary part of the vector
$*$	The conjugate of the vector
$\vec{B}$	Magnetic Field density
$\vec{D}$	Electric displacement vector
$\vec{E}$	Electric field
$\vec{H}$	Magnetic field in the magnetic component
$\vec{J}$	Total Current density of the winding
$\vec{M}$	Magnetic Moment per unit volume
S	Surface of the magnetic problem
γ	Curve which limits the surface S
γ_1	Volts-seconds
E	Stored Energy
Z	Impedance
Z_{cc}	Impedance of the short-circuit test
X_{cc}	Inductance of the short-circuit test
R_{cc}	Resistance of the short-circuit test
R	Electrical Resistance
$R_{effective}$	Effective resistance of the conductor according to the frequency
S	Surface of the cross-section conductor
$S_{effective}$	Effective Surface of the cross-section conductor according to the frequency
L	Magnetic Inductance
C	Capacitance
le	Effective length of the equivalent toroid of the magnetic core of the model component
σ	Electrical conductivity of the material
ρ	Electrical resistivity of the material
ε	Permittivity
f	Frequency
ω	Angular frequency
δ	Skin depth for circular sections
δ_i	Skin depth for polygonal sections
δ_{sk}	Depth due to the skin effect
δ_{cl}	Depth due to the current loop effect
r_1	Radius of the circular cross section
F_{pol}	Coefficient to compensate the resistance between the circular and polygonal cross section due to the current loom impact
AWG	American wire gauge
FE	Finite Elements
FEA	Finite Elements Analysis
FEM	Finite Elements Method
CPU	Central Process Unit
RAM	Random Access Memory
$1D$	1 dimensions. Problems whose solution depending on 1 geometrical coordinates
$2D$	2 dimensions. Problems whose solution depending on 2 geometrical coordinates
$3D$	3 dimensions. Problems whose solution depending on 3 geometrical coordinates
k	The correction factor
k_{skin}	The correction factor from the skin effect

k_{prox}	The correction factor from the proximity effect
k_C	Number of combination without repetition
EQ_R	Comparison between the resistance from the real model and the Polygonal model
A_{pol}	Division between the surface of the circular cross section and the polygonal cross section
RC	Standard Component
Av	Average
v_t	Volume of the magnetic component
v_g	Volume of the air-gap
v_c	Volume of the core
v_w	Volume of the windings
ED	Edge length in a square winding
m	Number of the edges in a polygonal cross section
i	Any Component
N	Number of the windings
n	Number of the turns
a	Ratio of turns between primary and secondary
I	Winding Current
S_{HL}	Surface of the hysteresis loop
A_c	Area of the Toroidal surface in the Toroidal component (A=width x height)
α	angle between windings (degree)
R_m	Main Radius=$(R_{max}-R_{min})/2$
L_i	Distance between the core and the winding
AC	Alternating current
DC	Direct current
P_{CPL}	Core power Losses
P_{HL}	Hysteresis power Losses
P_{ECL}	Eddy Current power Losses
B_r	Residual Flux Density
B_{sat}	Saturation value of the Magnetic field density
H_c	Coercive Field Force
sin	Sinus of the angle
MEC	Magnetic equivalent circuit
$MCEC$	Magnetic component equivalent circuit

1 Introduction

1.1 Magnetic components in power electronics

Power electronics can be defined as the technology that addresses the conversion and control of electrical power with switching mode electronic devices for applications as conversion from AC to DC or DC to AC, conversion of an unregulated DC voltage to a regulated DC voltage, and conversion of an AC power source from one amplitude and frequency to another amplitude and frequency.

This technology includes applications from circuit theory, control theory, electronics, electromagnetics, microprocessors for control, and heat transfer [1].

Power electronics engineers need to use magnetic components as an important part of their converters whose efficiency is an important specification that determines their success on the market. Losses of magnetic components are a critical part that influence greatly the overall efficiency, and even the operation capabilities of the converter.

Magnetic components can be broken down depending the frequency operation and the material isolation. According to the frequency [2]:

- Low frequency is considered to be between 50 and 500 Hz and usually connected to 220 ± 10% V (AC) single phase in Europe or 120± 10% V (AC) overseas. The typical applications are line filtering, motor drives, uninterruptable power supplies, pumping, conveyor systems, linear power supplies and electricity metering.

- Medium (500 Hz – 50 kHz) and High frequency (from 50 kHz up to GHz) applications are mobile devices, LED lighting, televisions, computers, communications equipment and even some systems in electric cars (energy and powertrain systems).
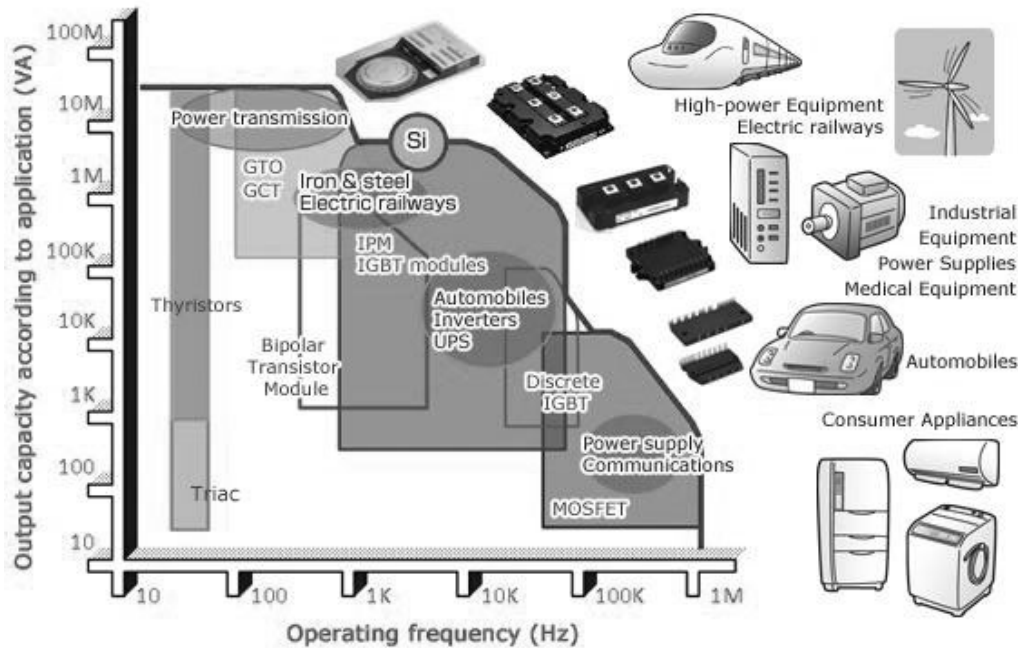
Figure 1. Power Electronics [3].

According to the isolation of the magnetic components, systems can be classified in:

- Non-isolated systems are utilized to reduce noise or store energy, filters and some transformers. These components usual work at 400 V (AC) or 415 V in UK and they give a 230 V AC output.

- Isolated components used to prevent human contact, where the primary side is separated from the secondary side, the internal windings would have one or more layers of insulation, which are usually manufactured with plastic bobbin.

In summary, the study of power converters is an essential task nowadays in many different engineering fields as power supplies, electrochemical processes, heating and lighting control, electronic welding, harmonic compensators, high-voltage systems, photovoltaic and fuel cell power conversion, high-frequency heating, cell phones charges, electrical vehicles, motor drives electronic devices and other fields in AC or DC [2] (Figure 1).

Power converters can be classified in rectifiers (AC/DC), choppers (DC/DC), inverters (DC/CA) and direct converters (CA/CA), as schematically shown in Figure 2.

There are also another different classifications for power converters depending on the commutation type and the application.
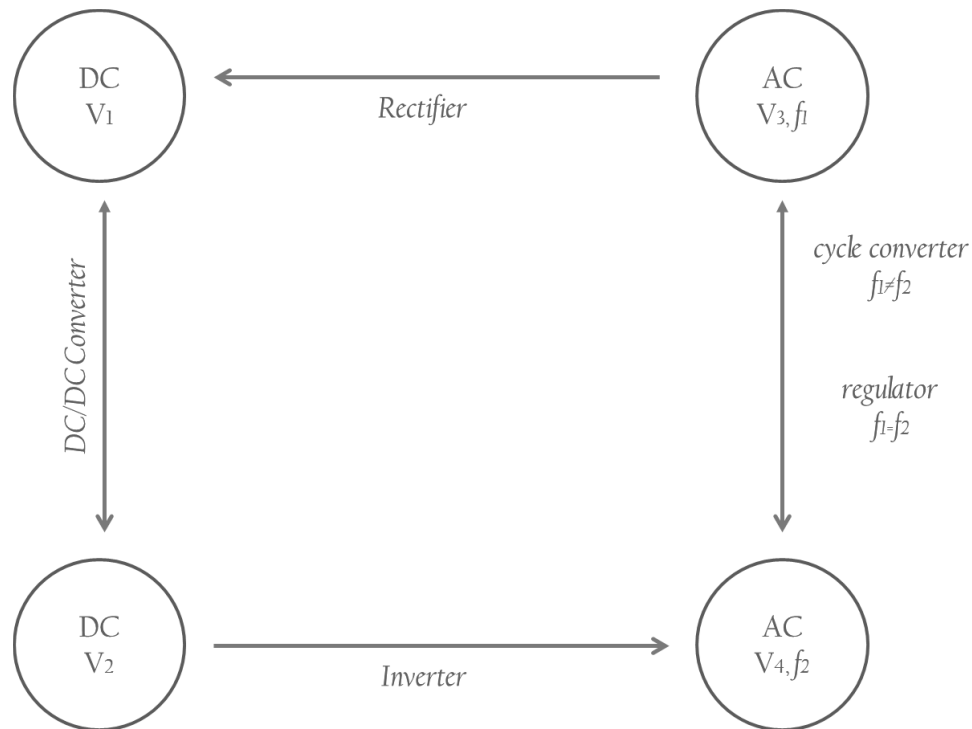
Figure 2. Power Converters.

Depending on the commutation, two main types are defined:

- Natural Commutation: the source of the primary voltage makes easy the outage of semiconductor devices. In addition, these semiconductors are in conduction state switching the same frequency than the voltage input.

- Forced Commutation: The controlled semiconductors are usually switched at bigger frequency than the grid frequency.

The classification depending on the application could be summarized as:

- Not Controlled Rectifiers: Devices that transform the AC voltage in DC voltage. They are composed by diodes.
- Controlled Rectifiers: Devices that transform the AC voltage in DC voltage. They are composed by thyristor. They can be reversible structures.

- AC regulators: Devices that transform the AC voltage in AC voltage with the same frequency.

- Cycle Converters: Devices that transform the AC voltage in AC voltage with different frequency.

- Inverters: Devices that transform the DC voltage in AC voltage

- Choppers: Devices that transform the DC voltage in DC variable voltage

One of the main factors for any power converter design is the energy efficiency because it could highly affect the converter operation. To minimize the converter losses electronic switches are used which main features are the following:

- They work in two different defined states. One is a block state (high impedance) and one is a conduction state (low impedance) giving the availability to support high voltage when it is blocked and high current when it is in conduction state,

- They switch from one state to another with the minimal time.

In addition, magnetic component used in power converters can have the role of providing galvanic isolation, energy storage or current filtering. The inductor used in a power converter, as in the example of Figure 3, can be modelled by an autoinductance and an associated resistance that produces a voltage drop in the winding that is proportional to the conductor current and limits the converter efficiency.

The inductor resistances limit the performance as can be follow in the example of Figure 4, where the impact of R_L/R index on the power converter efficiency of the power converter, being R_L the resistance of the inductor and R is the equivalent resistance at the output power converter terminals.
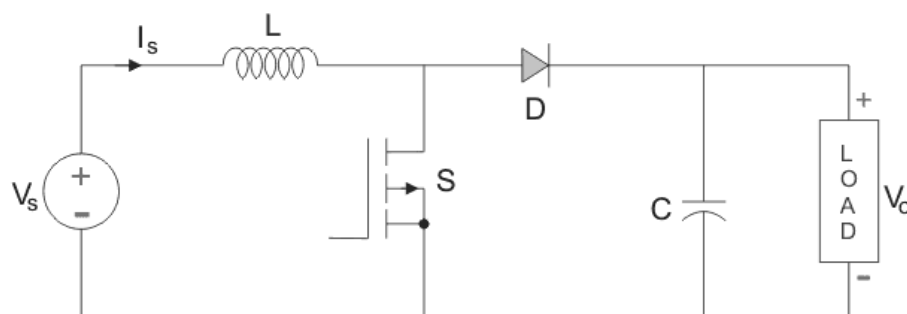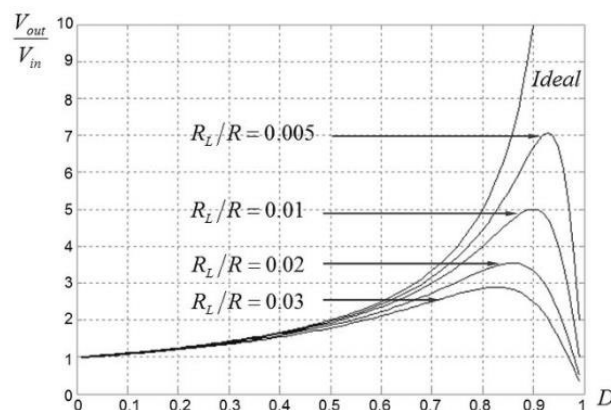

Figure 3. Boost Converter [4].

Figure 4. Output voltage vs. duty cycle of the boost converter circuit for different inductance parasitic resistance values [5].
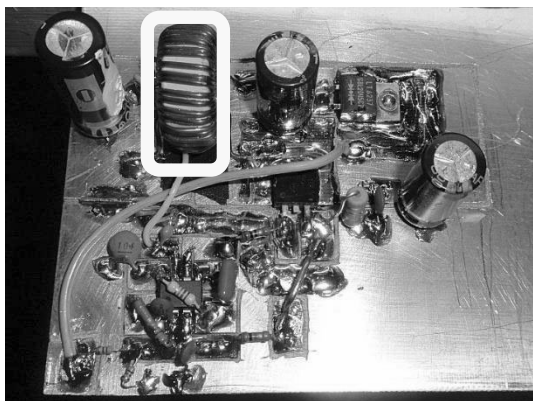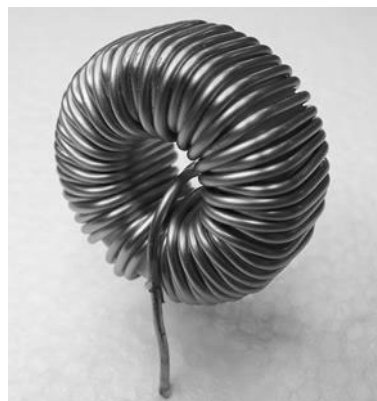
Figure 5. Example of Toroidal Core Inductor (a) Example of Power Converter I [6] (b) Example of Inductive Component I.
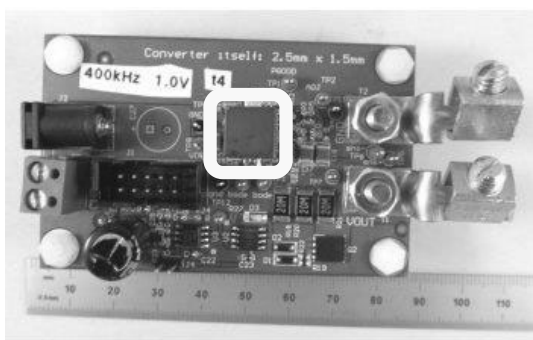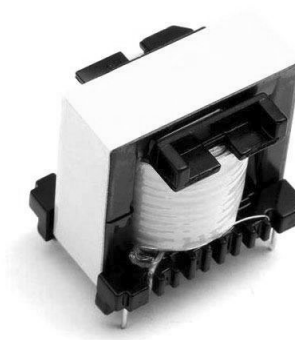
Figure 6. Example of EE Core Inductor (a) Example of Power Converter II [7] (b) Example of Inductive Component II [8].

Figure 5 and Figure 6 show real examples of power converters highlighting the inductor components. This work will focus on inductors with Toroidal (Figure 5b) and EE (Figure 6b) cores because they are the most common in power electronics due to the cooling is easy and the losses are not so high due to the core shape.

1.2 Doctoral thesis motivation

An original parameter extraction for the electrical equivalent model of a magnetic component that includes the high-low frequency effects (skin effect, proximity effect, interleaving, core gap) and other effects that can be only analysed in 3D for non-symmetric magnetic components will be proposed. The electrical parameters like resistance and inductance (self and mutual ones) are frequency dependent, then, this model represents the frequency behaviour of windings in detail. This work is focused in EE and Toroidal cores because they are very common in power electronics, however, this research could extend to other magnetic components without a great effort.

For asymmetric magnetic components, a 2D models are not precise enough and the current computations limitation do not allow the 3D finite element analysis (FEA) or they are not operative for design power engineers. The application of the new methodology to several magnetic components is going to demonstrate its usefulness and accuracy covering operation frequencies from 1 kHz to 1 GHz being the range of switching frequencies used by power electronics converters based on Si, SiC or GaN semiconductors.

The thesis is based on two previous works where an original parameter extraction procedure and deep analysis for all effects in high-low frequency are developed using 2D models.

- *Modelado de Componentes Magnéticos en alta frecuencia mediante la aplicación de la técnica de análisis por elementos finitos* by Rafael Asensi in 1998. The major original contribution is the winding modeling using Finite Element tools proposing an equivalent circuit using parameters extracted from the Finite Element Method (FEM). In addition, the parameter extraction procedure is universal (valid for every magnetic component) and simple for models in 2D [9]- [11].

- *Análisis y Optimización de Componentes Magnéticos Mediante Técnicas de Elementos Finitos* by Roberto Prieto in 1999. In this work, a study of magnetic components using an original methodology by FEM tools to quantify the effects due to the geometrical parameters of the magnetic component and different magnetic field distributions is performed. This thesis describes the double 2D method, giving an alternative solution between 2D and 3D models for asymmetric components) [12]- [15].

1.3   Doctoral thesis objectives

The main thesis goal is the proposal of an original parameter extraction for the electrical equivalent model for inductors that cannot be analysed in 2D or the required CPU time is not operative for the optimization of the magnetic component in the design phase by the power electronics engineers. The proposed 3D model includes all frequency effects like skin, proximity, air-gap, winding interleaving, edge effects that cannot be analysed with 2D models. Thus, an electrical equivalent circuit using an original methodology for the parameter extraction using 3D FEM will be defined. In the path of this research, some specific objectives have been selected to obtain the main purpose:

1. Understanding of the hardware computer limitations due to the number of finite elements used at the FE tool (Maxwell Ansys in this thesis).

2. Selection of the most operative simplifications on the component model for reducing to the CPU time.

3. Proposal of the new methodology for determining the electrical parameters for the equivalent circuit divided in: (1) modelling, (2) simulation and (3) result-processing with the correction factor and experimental validated. The electrical parameters determination has taken into account the skin and proximity effect as other frequency effects for the winding losses

4. Analysis of the hysteresis and eddy current losses in the inductor core using the per-unit method to identify which geometrical parameters of the inductor have more influence in the core power losses.

5. New procedure to determine the core power losses in any inductor based on 3D models separating the influence of the hysteresis losses and the eddy current losses and presentation of a new equation based on this original procedure for the core power losses in saturation or no saturation of the toroidal cores.

1.4 Doctoral thesis structure

In the first chapter, the motivation, structure and main contributions of the thesis are presented.

In the second chapter, an introduction for magnetic component modeling using FEM is described in detail, with the main frequency effects for understanding why a magnetic component should be modelled in 3D. Also the conclusions for the first objective of the thesis are shown. Also, computer limitations that avoid all 3D models can be simulated in a FE tool will be described. Therefore, several simplifications will have to be introduced only to be available the FE simulation achieving the second objective of the thesis.

In the third one, a parameter extraction for electrical equivalent circuit for the windings (in EE and Toroidal core inductors) is presented using 3D FEM, that is divided in model simplifications in the pre-modeling phase and use of the correction factor at the post-modeling phase for the skin and proximity effect to compensate errors between the real and simplified model values obtaining the third objective of the thesis.

In the fourth chapter, the core power loss model will be set forth. There will be a short introduction for two main procedures to predict the core losses: hysteresis model and empirical equations. A new method that uses only coil and core geometrical and material parameters determine the core power losses and it is used to define the equation for Toroidal components to accomplish the fourth and the fifth objective of the thesis.

In the chapter five, the conclusions will be presented and several future research directions will be identified.

The chapter six is summarized the publications and work related to the thesis. In addition, there is a professional curriculum performed in parallel to the thesis' work.

The last chapter is dedicated to the references used in this thesis.

1.5   Doctoral thesis results and original contributions

The main result of the thesis is a new methodology for the electrical parameters extraction of equivalent model of magnetic component using 3D FEM being published in a journal publication (Q4, [see chapter 6, publication B]). The methodology includes in the modeling phase some simplifications to reduce the computational limitations (the modification of the conductor cross-section from circular to polygonal one and its correlative material conductivity adjustment to have the same resistance at DC), enabling to obtain the results with the required precision in an acceptable execution time. At the result-processing, a correction factor is used for the electrical parameters due to the skin and proximity effects have different behavior at high frequency, being published the work focused in skin factor in a journal publication (Q3, [see chapter 6, publication D]).

In order to develop this methodology, the computational limitation for non-symmetric components (EE and Toroidal cores) was calculated. The definition of this limitation will allow proposing the hexagonal section for the wiring conductor in the windings as the best choice in the model simplification according to the executive CPU time. Several conference publications are divulgating these conclusions [see chapter 6, publications, F, G, H].

Another major original contribution has been the core power losses determination method which it does not need any previous analysis or calculus of the magnetic field density (it is determined indirectly) into the core as the current models being published in a journal publication (Q1, [see chapter 6, publication C]). The proposed model splits the losses by nature, hysteresis losses and eddy current losses, helping electronics engineers to take decisions for optimizing the inductor component in the design phase according to the operational frequency. This method has been used for Toroidal Components giving a final equation for them.

Twelve publications summarize the work of this thesis, where chapter 6 shows the list of publications in detail.

2 Magnetic component modeling

This chapter is dedicated to the introduction of the magnetic modeling based on FEM, whereby the laws of Maxwell are presented as well as the frequency effects involved in the magnetic components for understanding the complexity to design power electronics. Details of the magnetic field distribution will be summarized to understand the allowed simplifications to solve the Maxwell´s equations and their advantages and disadvantages for specific magnetic components.

The FEM will be also described, introducing the FEA tool chosen for this thesis. This chapter will clarify the state of the art for electrical equivalent circuit and FEM based analyses. At the end of the chapter, the computer limitations for 3D models will be presented on the basis of a FEM study for asymmetrical components.

2.1 Basic electromagnetic theory for modeling

The laws of Maxwell are a set of coupled partial differential equations which form the basis of the electromagnetism and electric circuits because they are the mathematical models that determine the electric and magnetic fields that are created by currents, charges and fields variations. The system of equations is:

Faraday´s law
$$\oint_{\gamma} \vec{E} \cdot d\vec{l} = -\frac{d}{dt} \iint_{S} \vec{B} \cdot d\vec{S} \tag{1}$$

Gauss´s law
$$\oiint_{S} \vec{D} \cdot d\vec{S} = \oiint_{S} \varepsilon \vec{E} \cdot d\vec{S} = \iiint_{v} \rho \, dv \tag{2}$$

Gauss´s law for magnetism
$$\oiint_{S} \vec{B} \cdot d\vec{S} = 0 \tag{3}$$

Ampère´s circuital law
$$\oint_{\gamma} \vec{H} \cdot d\vec{l} = \oint_{\gamma} \frac{1}{\mu} \vec{B} \cdot d\vec{l} = \left(\iint_{S} \vec{J} \cdot d\vec{S} + \frac{d}{dt} \iint_{S} \varepsilon \vec{E} \cdot d\vec{S} \right) \tag{4}$$

where $\vec{E}$ is the electric field, $d\vec{l}$ is the differential vector element of the border of the S and γ is the curve that limits S, $\vec{B}$ is the magnetic field density, $d\vec{S}$ is the differential vector element of area S, $\vec{D}$ is the electric displacement field and is given by $\vec{D} = \varepsilon \vec{E}$ bring ε the permittivity, ρ is the electrical charge density, dv is the differential vector element of volume v, $\vec{H}$ is the magnetic field being $\vec{H} = \frac{1}{\mu} \vec{B}$ where μ is the magnetic permeability and $\vec{J}$ is the current density.

The resolution of the system of equations is tangled in 3D, thus, it needs some simplifications in the system of equations that depends on:

- The symmetry of the magnetic component to use 1D,2D or 3D magnetic field distribution in the problem where the laws of Maxwell are applied.
- The frequency of the problem, being in low frequency the displacement current density neglected and if not it is a magnetodynamics problem.

Whereby, in power electronics field, the only potential simplification depends on the symmetry of the magnetic component to solve the system of equations.

These equations are used to design and to optimize the magnetic component, being involved more variables such as material properties, switch technology, device dimensions, application specifications, production and process cost among others.

The component design needs to the mechanical, thermal and electromagnetic modeling with the additional performances constraints to achieve the final solution. Therefore, the

determination of electrical equivalent circuit can be performed analytically or by mathematical approximate resolution of the Maxwell´s equations. As it is known the analytical solutions are only available for 1D models, FEM is usually needed for 2D and 3D models.

2.2 Effects in the model

To model the magnetic component is complex due to the high-low frequency effects involved in the power converters operation. The understanding of these effects is important to select the magnetic field density distribution for the problem and also to obtain an appropriate model for the magnetic component. These effects owe to the component geometry and the frequency range where the magnetic component works [16,17].

The component geometry defines the symmetry selection which can be considered for the problem case and thus, the simplifications in the Maxwell´s equations that could be assumed to solve the particular problem.

2.2.1   *Skin effect*

This skin effect produces the tendency of the alternating electric current to flow mostly near the outer layer of the conductor [18,19]. The electric current flows mainly at the skin of the conductor, between the outer surface and a level called the skin depth (Figure 7). The influence of the skin effect over the electrical resistance in a conductor is determined by means of the skin depth which is defined as the equivalent thickness of a hollow conductor having the same resistance at the frequency of interest. Therefore, it causes the effective conduction resistance increase. The skin effect is due to opposing eddy currents induced by the changing magnetic field resulting from the AC current. This phenomenon is explained by Lenz law where the skin depth, δ, is determined by (5) [21].

$$\delta = \frac{1}{\sqrt{\pi \cdot f \cdot \mu \cdot \sigma}} \tag{5}$$

where f is the frequency, μ is the magnetic permeability and σ is the material electric conductivity.
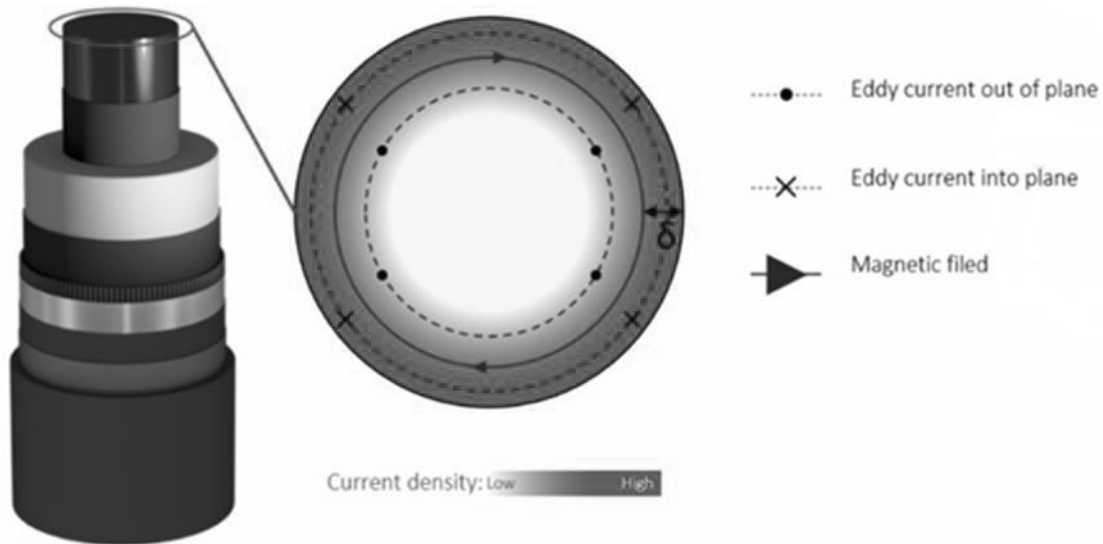
Figure 7. Skin effect [18].

2.2.2 Proximity effect

A variable magnetic field will influence the distribution of an electric current flowing within an electrical conductor by electromagnetic induction. When an alternating current flows through an isolated conductor, it creates an associated alternating magnetic field around it. This field will induce eddy currents in adjacent conductors, altering the overall distribution of current flowing through them.

So, in a conductor carrying alternating current, if one or more other conductors are close, such as a wound winding, the distribution of current within the first conductor will be constrained to smaller regions than if there is only one isolate conductor [19,20].The resulting current crowding is termed the proximity effect (Figure 8) and produces an increase in the effective resistance of the circuit, which is greater when the frequency is higher.
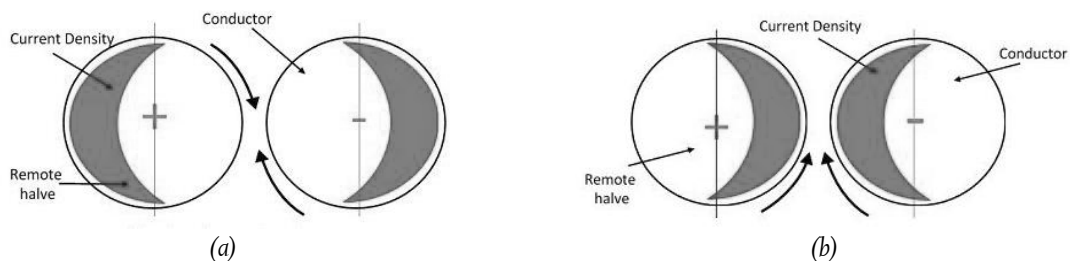

(a) *(b)*

Figure 8. Proximity effect [21] (a)Direction of current remains same (b) Current flow in opposite direction.

The proximity effect can significantly increase the resistance of adjacent conductors when compared to its resistance to a DC current. At higher frequencies, the AC resistance of a conductor can easily exceed ten times its DC resistance.

2.2.3 Air-gap effect

The magnetic flux lines can vary when going through different materials due to the value of the magnetic permeabilities, and this property is used in the design of the magnetic components. One of the most usual cases is an air-gap introduced in the magnetic core (Figure 9), introducing a discontinuity in the material. It produces a magnetic flux that disperses in the closed zone to the air-gap [22] which is a flexible tool for the power engineers to optimize the magnetic components reducing the core power losses.

The disperse flux affects the current distribution of the conductors near the air-gap, this phenomenon is very similar to the skin and proximity effect because the current of the conductors tries to minimize the energy with its own distribution.
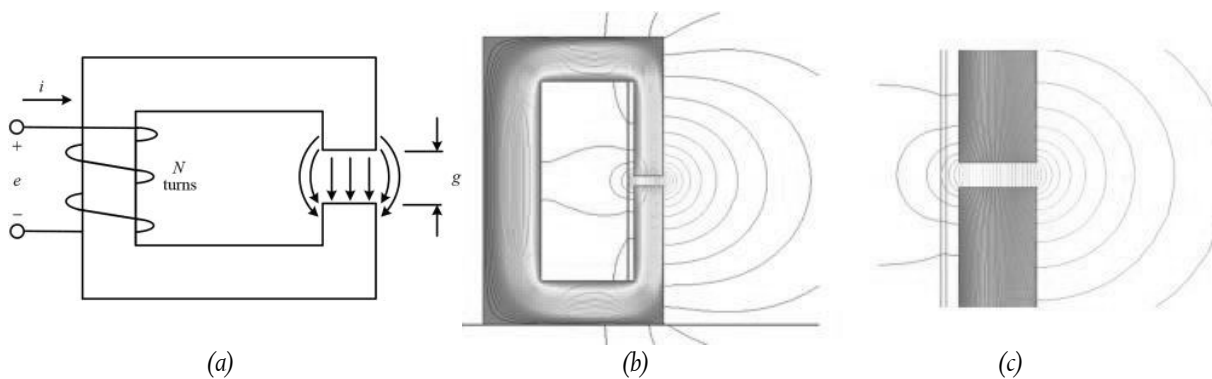

| (a) | (b) | (c) |

Figure 9. Air-gap effect [23] (a) Air-gap core (b) Magnetic field distribution in the magnetic component (c) Zoom in the core gap .

2.2.4 Edge effect

The edge effect consists in the modification of the flux direction when the core finishes, in each winding belonging to the magnetic component, the conductors fill the high of the window, and then, the distribution of the field is practically in the same direction, so, when the field flow at the up or down of the core window (Figure 10), the field has to change the direction and it appears to have a new distribution different the main one [25]. Also, when it is winded the primary and secondary in the same split of the component, this effect appears in the edge and in the space of the two closed turns of the winding.
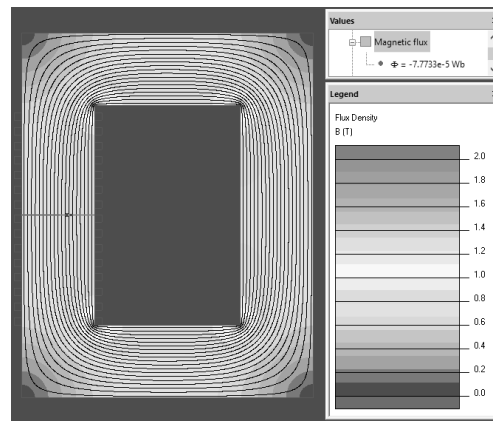
Figure 10. Edge gap effect [24].

2.3 Magnetic field distribution

In order to use an adequate model for any magnetic component it is necessary to recognize the symmetry of the magnetic field density to know if any of the magnetic field direction can be removed in the analysis of the inductive component (Figure 11). There are three different types of distributions.

2.3.1 1D Magnetic field distribution

This case is when the variation of the magnetic density field is only in one of the potential directions, and the field is constant or practically null in the other directions (Figure 11), thus, the Maxwell´s equations can be simplified considerably. Examples of these cases are when the windings take up all the space of the component window without any interleaving in the magnetic core, and when the cylindrical geometry is used in coils.

This case allows the simplification of the Maxwell's equations in only one dimension because all terms of these equations and their variations from the main direction can be eliminated [26,27] and it has the following advantages:

- Skin and proximity effects are considered.
- These models which are dependent of the frequency are valid for any waveform because of all harmonics are considered.
- There is no problem of convergence when running the simulations.
- The models are based directly on the Maxwell's equations in 1D distribution (only one axis) and they are only valid for this case.

Chapter 2. Magnetic component modeling

Faraday´s law
$$\oint_{\gamma} \vec{E}_x \cdot d\vec{x} = -\frac{d}{dt}\int_{\gamma} \vec{B}_x \cdot d\vec{x} \tag{5}$$

Gauss´s law
$$\oint_{\gamma} \varepsilon\vec{E}_x \cdot d\vec{x} = \int_{\gamma} \rho \, dx \tag{6}$$

Gauss´s law for magnetism
$$\oint_{\gamma} \vec{B}_x \cdot d\vec{x} = 0 \tag{7}$$

Ampère´s circuital law
$$\oint_{\gamma} {}^1\!/_{\mu}\vec{B}_x \cdot d\vec{x} = \left(\int_{\gamma} \vec{J}_x \cdot d\vec{x} + \frac{d}{dt}\int_{\gamma} \varepsilon\vec{E}_x \cdot d\vec{x}\right) \tag{9}$$

where x is the differential where there is variation of the magnetic field and γ is the curve or line.

The analyses in only one dimension have disadvantages such as:

- They are not applicable when there are conductors of different windings in the same split.
- Air-gap or edge effects are not taken into account.

The 1D model is based on the transformation of the circular conductors in layers of current, therefore, it is necessary that every layer has only one conductor with only one winding. This transformation helps also to examine the accuracy and the precision depends on the level of filling of the conductors in each layer. In other words, with the increase of separation in a layer, there is a decrease in the precision. Figure 11 (a) and Figure 11(d) show the approximations to layer the remaining the area to have the same resistance.

2.3.2   *2D Magnetic field distribution*

This case is when the variation of the field is in two different directions, and the field is constant or practically null in the third direction (Figure 11 (b) and 11 (e)), then, the magnetic component has to have an axial symmetry axis.

Examples of these cases are when the windings do not take up all the space in the window or there is some interleaving among turns. Dr. Roberto Prieto [15] introduced in his thesis a double 2D method that is applied in two different directions for these components.

These models consider all effects in 1D models and others [27-30]. To obtain these models is necessary to solve the Maxwell's equations in 2D and the main advantages of doing that are:

- The model is capable to reflect every phenomenon produced in the magnetic component if it has axial symmetry.
- Effects like air-gap and edge effects are considered only in 2D.

The main disadvantages are:

- 2D models are not accurate for non-axial symmetry components.
- The models are based directly on the Maxwell's equations in 2D distribution and they are only valid for this case. The next equations are the laws of Maxwell in Cartesian Coordinates to show the difficult to solve, even in 2D.

Faraday's law
$$\oint_{\gamma} \vec{E}_{xy} \cdot d\vec{x}d\vec{y} = -\frac{d}{dt}\iint_{\gamma} \vec{B}_{xy} \cdot d\vec{x}d\vec{y} \tag{10}$$

Gauss's law
$$\oint_{\gamma} \varepsilon\vec{E}_{xy} \cdot d\vec{x}d\vec{y} = \iint_{\gamma} dxdy \tag{11}$$

Gauss's law
for magnetism
$$\oint_{\gamma} \vec{B}_{xy} \cdot d\vec{x}\,d\vec{y} = 0 \tag{12}$$

Ampère's
circuital law
$$\oint_{\gamma} {}^{1}/_{\mu}\vec{B}_{xy} \cdot d\vec{x}d\vec{y} = \left(\iint_{\gamma} \vec{J}_{xy} \cdot d\vec{x}d\vec{y} + \frac{d}{dt}\iint_{\gamma} \varepsilon\vec{E}_{xy} \cdot d\vec{x}d\vec{y}\right) \tag{13}$$

2.3.3 *3D Magnetic field distribution*

In the case when there is not any symmetry it is not possible to eliminate any term in Maxwell's equations. The magnetic field distribution in 3D can be due to the geometry of the magnetic core or for the winding strategy (Figure 11 (c) and 11 (f)). To obtain these models it is necessary to solve the Maxwell's equations usually by FEA, but this is a problem because it needs computing power resources. The main advantages are:

- The model is capable to reflect every phenomenon produced in the magnetic component.
- The parameters of the model need to be obtained by the 3D analysis of the Maxwell's equations, through the solutions of the field and energies that consider the 3D effects.
- It is based on the solutions of the Maxwell's equations in 3D, so the constrains are not similar to those present in the 1D and 2D models.
- Effects like air-gap and edge effects are considered.
- They are applied for every magnetic component and winding strategy.

The main disadvantages are:

- FEA is needed to solve the model and the time for getting the solution is longer than 2D model, requiring significant CPU time for any magnetic component with 3D FEA.
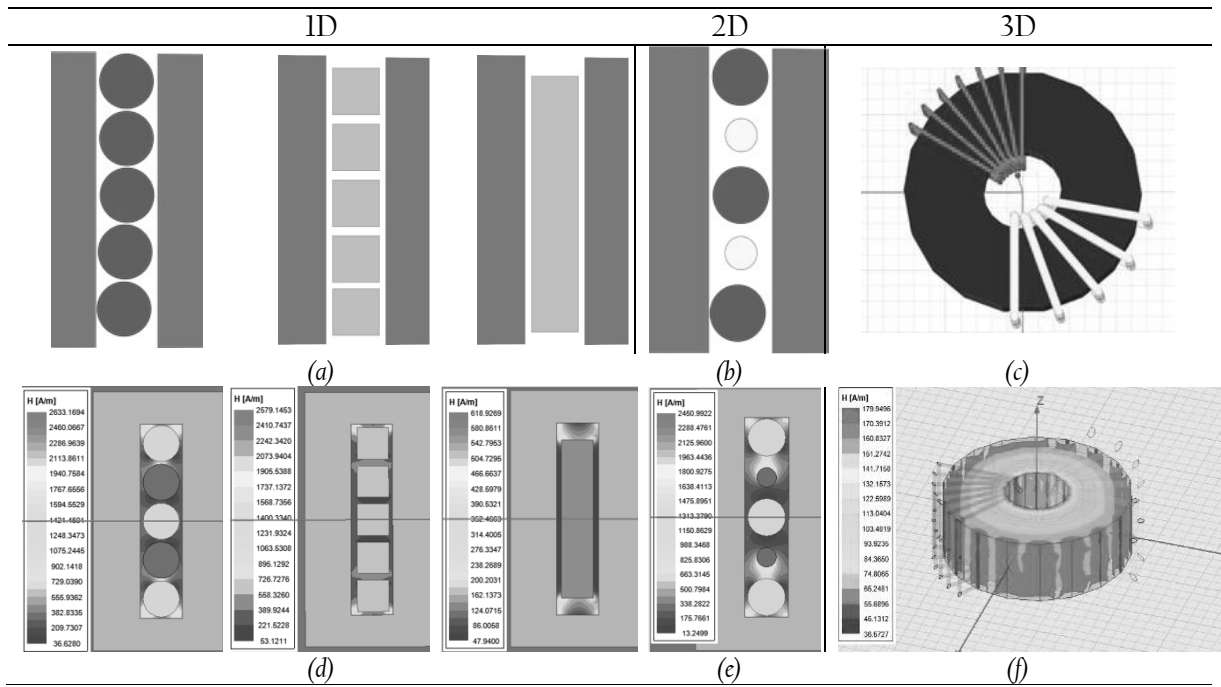- At higher frequencies (> 10MHz), the time consuming in FEA is especially long and the error increases substantially.

Chapter 2. Magnetic component modeling

Figure 11. Magnetic Field Distribution (a) 1D Model and approximations (b) 2D Model (c) 3D Model (d)Example of 1D model, concentration of the windings and approximations (e) Example of 2D model, interleaving (f) Example of 3D model, Toroidal Component with non-symmetry winding strategy.

Table 1. Comparison among models 1D/2D/3D

Model	Considerations	Frequency Effects					Simulation Complexity	Model Design Complexity
		Skin	Proximity	Air-gap	Edge	Others		
1D	All the window is full for windings	✓	✓	X	X	X	Low	Low
2D	Axial symmetry	✓	✓	†	†	*	Medium	Low
3D	Any case	✓	✓	✓	✓	✓	High	High for windings

Effects that are only considered in 3D models (i.e.: terminals of the windings)
†Considered only in 2D

- Although it is possible to use in components with distribution of far field in 2D, the precision is very low in the magnetic field distribution it the analysis is performed in 3D.

Table 1 shows a comparison among models in 1D, 2D and 3D. The usual symmetry for different magnetic core components used in the analyses is indicated in Table 2. In general, the cores with square windings need a 3D model to be studied.

Table 2. Symmetry for different magnetic core components

Denomination	Core	Winding Strategy	Dimensional Analysis Required
EFD		1	2D
		2	3D
EP		1	2D
		2	3D
ETD		1	2D
		2	3D
POT		1	2D
		2	3D
PQ		1	2D
		2	3D
RM		1	2D
		2	3D
EE		1	1D/2D
		2	3D
EI		1	1D/2D
		2	3D
Toroidal		1	3D
		2	3D

Winding Strategy:
1: The magnetic component window is fulfilled by turns and there is not interleaving
2 Any another different winding strategy 1

2.4 Model based on FEM

The thesis is based on the analyses obtained from FEM that it is a computer based power tool to solve electric, magnetic, dynamic and thermal problems, also contains experiments and other techniques to determine the electromagnetic parameters when modeling a magnetic component. Several softwares codes are available in the market for electromagnetic analyses being shown in Table 3 several ones from the comparisons in [31] and [32] .

It is necessary to remark that the work developed in this thesis could be performed in any 3D electromagnetic software to obtain the same results. The selected software has been Ansys Maxwell because it is the widely used in the interdisciplinary engineering companies.

Table 3. Electromagnetic FEA

Software / Features	Usage	Electric Module	Auto Cad File Integration	Graphic Performance	Memory Disk Performance	Overall Performance	Accuracy
Maxwell	Easy	Exist	Poor	Very Good	Good	Good	Average
Cedrat	Difficult	Exist	--	Good	Average	Good	Average
Ansys/Multiphysics	Hard	No	Excellent	Very Good	Good	Very Good	Very Good
Ansys/Workbench	Average	No	Good	Bad	Poor	Poor	--
Opera	Hard	No	Good	Excellent	Excellent	Very Good	Excellent

2.4.1 *Ansys Maxwell*

Maxwell can solve stationary and transient electromagnetic problems in 2D and 3D. In addition, it is possible to model materials with non-lineal properties and include hysteresis loop data. The process for a FEA is divided in three steps as they are:

1. <u>Modeling:</u> In this phase, the component geometry is configured (Figure 12) as well as the boundaries definition which means the establishment of the space limitations, because the software cannot simulate infinite regions, therefore, it needs to limit the analysed space and constrain the boundaries. For electromagnetic analyses, the boundary conditions are the fixations of the magnetic field directions in theses layers (normal, null or perpendicular). Also, the specification of the analysis is selected among harmonic, transitional or stationary conditions. The material properties for the different components used in the model are defined in this step, like conductivity or permeability for the electromagnetic analyses. The currents, voltages or a different input must be defined in this phase in the component geometry. The last step in this phase is the configuration of the mesh. FEA divide the geometry in small regions where the Maxwell´s equations are

2. applied which is why this division is named mesh. The greater number of elements the mesh has, the more precision the solution has, needing more CPU time.

3. <u>Simulation:</u> Maxwell solves the model defined in the previous phase according to the analysis settings to obtain the convergence which depends on the target error, energy error and delta energy defined by the user. According to the mesh and the analyses settings will be CPU time to solve the problem or obtain the convergence. More detail about the convergence process for Maxwell is located in Appendix II.

4. <u>Result Processing:</u> After the convergence is performed, the software allows obtaining values for some variables as energy, loss and other parameters depending on if the analysis has been developed in the frequency or time range. Also, it can use complex scripts to determinate specific parameters and produce graphics in 2D and 3D, color pictures of a single parameter is available as well. This option allows to obtain the parameters for the chosen equivalent circuit as well as any core situation introducing the material data.

2.4.1.1 Comparison between 2D and 3D in Ansys Maxwell

To show the different requirements for analysing in 2D and 3D in Ansys Maxwell with the same computer, a simple component that allows being analysing in 2D has been simulated in 3D as well. The component is the one of the simplest components to be simulated being a copper square rounded by a ferrite core. If the magnetic energy is calculated from the 2D and 3D models flowing 1 A through the copper is obtained the results shown in Table 4. It should be remarked that the 3D model needs more FE than is shown to achieve an asymptotic value of the inductance. This simulation shows the different Finite elements required between 2D and 3D models.
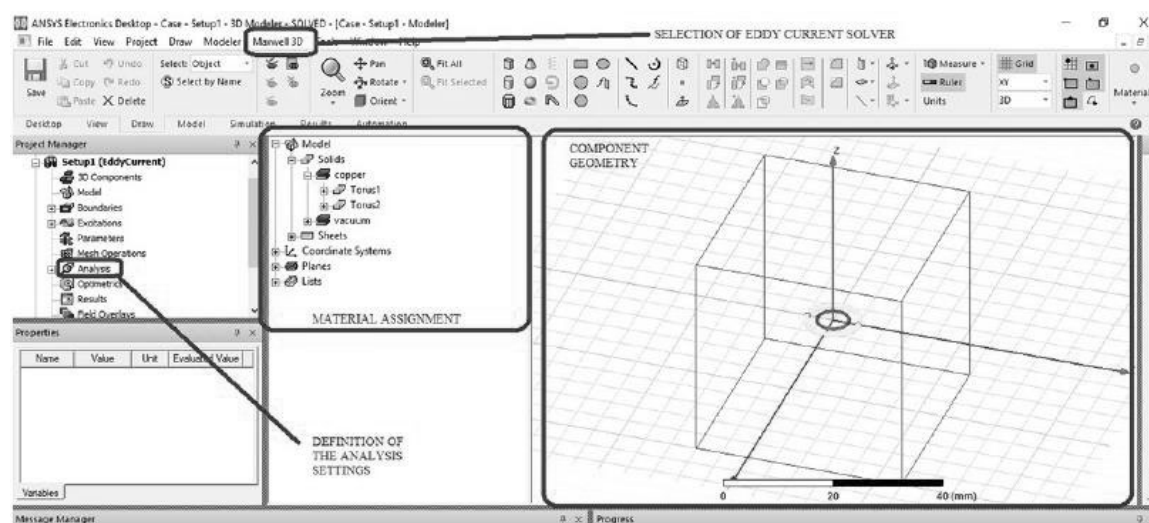

Figure 12. Ansys Maxwell environment.

Table 4. Comparison between 2D and 3D models

	Number of required FE	Air Inductance (nH/distance)	CPU Time* (s)
2D	382	120	3
3D	7907	117	68

*RAM: 4GB

2.4.2 Model structure

This section describes the electromagnetic model used in this thesis based on FEM. In order to propose a model which depends on the frequency, the impedance has to be determined using a frequency sweep, where the real and the imaginary parts are respectively the resistance and the inductance for the equivalent circuit.

The proposed model is formed by the components W (Figure 13) which represent the change between voltage and current to magnetic flux and magnetomotive force. Therefore, the core model is represented as a hysteresis cycle allocated to the magnetic model side [33-37].

The impedance Z_{11} represents the produced effects when the current only flows through the first winding, the impedance Z_{22} are the effects produced when the current only flows through the second winding, the impedance Z_{12} are when the current flow for both windings.

Figure 13 shows the position of the capacitors which represent the energy storage in the component according to the operation. The values are determined from two different analyses, the first one consists of the same voltage between both sides, the second analysis involves the voltage if one of the sides is null. For the capacitors, the index 1 means the values from the first analysis, the index 2 (offset) are obtained from the second analysis. This thesis is only focused in the winding loss and the core loss, so, more details about capacitor determination can be found in [13-14].

The model is useful for estimating the power losses for the winding components, and are as follows:

   a) copper losses which are related to the winding resistances,
   b) hysteresis losses due to the magnetic friction inside the core,
   c) eddy current losses due to the induced currents by magnetic fields.

The copper losses are the only one that are present even for DC current, the other losses are null. There are other minor losses such as physical vibration of the windings and the core, the electromagnetic radiation and dielectric losses in materials used for insulation.

One of the tasks of power engineers is the optimization of the design, which includes the minimization of the power losses, covering the selection of the winding strategy analysed in chapter 3 and the core design (chapter 4 is focused on this topic).

The winding strategy depends on the current density whereby a high value leads to compact, cheap and inefficient inductors and low values implies usually expensive, efficient and reliable designs. In addition, the skin and proximity effects are mainly involved in the current density in the windings in AC.

On the other hand, the core losses, mostly hysteresis and eddy current losses, could vary significantly if the core size and its material is not selected properly seeking for the minimal value of the magnetic field density into the core.

Therefore, a good balancing of copper and core losses is needed for the optimization of the magnetic component, to be efficient, cheap and successful in the market. However, this balancing is complex because they are inversely proportional according to the core size and same magnetic flux.
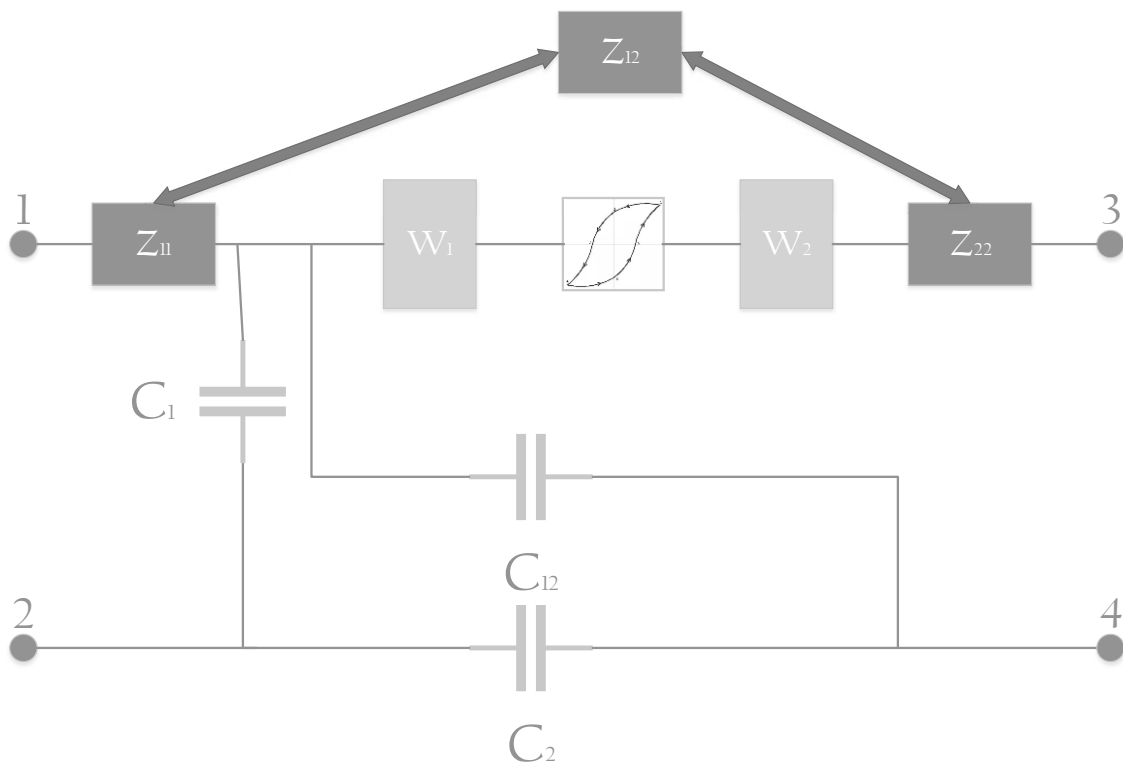

Figure 13. Component Model.

In addition, the balance between the copper loss and the core loss relies on the peak value of the AC component of $|\vec{B}|$, ΔB (*Figure 14*) as defined as from [38] for a simple transformer :

$$\Delta B = \frac{\gamma_1}{2 \cdot n_1 \cdot A_c} \tag{14}$$

$$\gamma_1 = \int_{t_1}^{t_2} V_1(t)dt \tag{15}$$

where n_1 is the number of turns of the primary side, A_c is the total surface of the core and V_1 is the voltage in the primary side, and γ_1 denotes the volts-seconds applied to the primary winding during the positive portion of the voltage between the time period from t_1 to t_2 in the waveform.

Figure 14 shows a particular example of an inductor to be used in avionic applications whose DC/DC converter will work at 10 kHz in V_{IN}/V_{OUT}=450 V/270 V. The light blue line represents another constrain to have in the inductor design, the maximum operation temperature, $P_{maxTemp}$, and the purple line means the minimum number of turns, N_{min}, which depends on the flux density and the effective area of the core that can be modified by increasing the stacking of the core. In addition, there is a quadratic relationship between the winding resistance and the number of the turns according to [38].

There are a number of variables involved in the power losses and many factors to consider the relationship among them to estimate the core losses and the copper losses. Also, additional requirements such as size, weight, thermal limitation and project budget may have to be considered in the design.
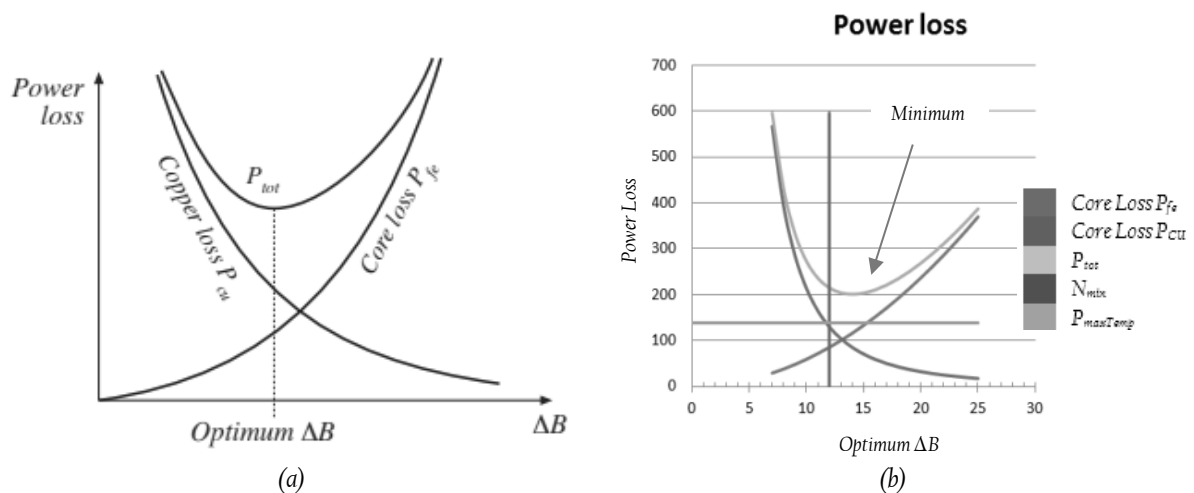

Figure 14. (a) Power Loss Optimization [38] (b) Example of Power Loss Optimization for 10 kHz in V_{IN}/V_{OUT}=450 V/270 V [32].

In conclusion, the calculation of both losses, copper and core, are very important to design and optimize the inductor component to be successful in the competitive market and useful for the application that it has been designed for.

2.4.3 *Parameter extraction procedure*

The parameter extraction procedure is based on the values of energy and losses obtained from FEM in every element using the electrical equivalent circuit from [9]. The Finite Element Analysis determines the electromagnetic field in each model region and therefore, any electromagnetic variable can be calculated by FEM because the Maxwell´s equations are applied in every point of the component.

A distribution of the energy in the model is needed to use this method because some parameters like dispersion and magnetizing inductances are not linked to any part of the model (i.e.: all stored energy in the component window is magnetizing energy).

To explain the procedure for the parameter extraction, it should be highlighted the proposed method is based on the superposition theorem which is applied to magnetic fields and current densities and not to energies and losses. This theorem requires a linear system; thus, the inductor will be considered a linear behaviour component, the only nonlinear part of the inductor as far as current is concerned is the core, therefore, a permeability constant value will be used for modeling the core in the FE tool.

The FEA achieves the energy and losses in the magnetic component for different work conditions (open circuit and short circuit):

- Open circuit condition

  In this condition, the current flows only by one winding producing copper losses in this winding and some losses in the other ones will be produced by the induced currents. In this situation, all magnetic energy can be considered magnetizing energy, with the dispersion energy neglected.

- Short circuit condition

  In this condition, the currents flow in each different winding at the same time. The current value in any position depends on the many parameters being very complex to determine the cause. Therefore, the procedure is only based on open circuit analysis.

2.5 State of art

Electric and electronics engineers are used to work with an electrical equivalent model for analysing and optimizing a magnetic component [28,39]. This model can help understand the phenomena in high-low frequencies. The review of the existing models will allow identifying the advantages and disadvantages from the frequency effects explained previously.

The model proposed in [40] establishes an analogy between electrical circuits and magnetic ones. In an electrical circuit, when a voltage is applied, it produces a current in the circuit. The relationship between both parameters is the resistance. In a magnetic circuit, the magnetomotive force is applied producing a magnetic flux, being the relationship between these magnitudes, the reluctance. Then, it can be found an electrical equivalent circuit that represents the behaviour of the magnetic component and it allows the calculation of the magnetic flux or magnetomotive forces according to the theory of circuits (Figure 15).

An improved model is used in [41] where the currents are not concentrated in a given point in the windings as the previous model, but they spread over the length of the windings [42]. This approach is used only for the current models in the low frequency range.

A different solution is included in [43] based on [44], for multiwinding transformers at industrial frequency (50 Hz) where the magnetizing inductance is neglected and it is not valid for air-gap components, but useful for harmonics analysis.

The described models do not take into account the variation on the effects in the operational frequency range of the power converters. The inclusion of the frequency influence needs the Maxwell´s equations resolution, and to do so, some simplifications are required to solve them One of these simplifications is currently used in practical designs [45] assuming that the windings of the magnetic component is a boundless solenoid, which is useful for symmetric magnetic component modeling and appropriate for high and low frequencies.
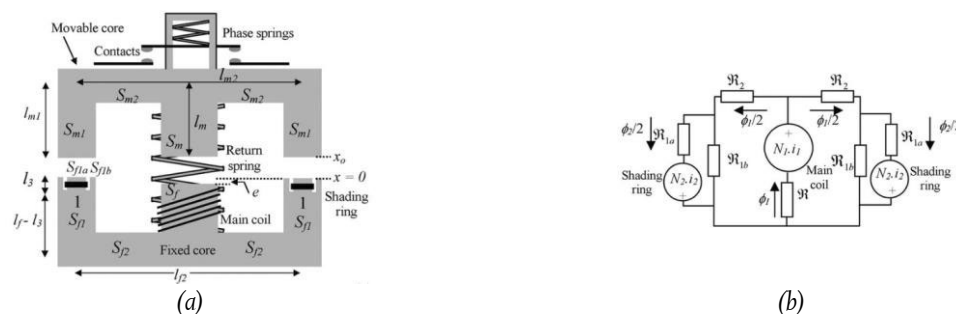

Figure 15. Magnetic Equivalent Circuit [46](a) the electromagnetic contactor(b) the magnetic circuit.

To model components with more than two windings is also of interest. Modifications in the electrical equivalent circuit from [44] were published in [47,48] with a model that reflect the

mutual coupling. Different analytical expressions for planar configuration [49] and for spiral coils [50] were determined in other works.

Previously, there were experimental methods based on a solenoid working in resonance with an auxiliary capacitor [51,52], and also, theoretical methods that obtained different formulas which allow calculating the solenoid capacitance depending on its dimensions [53,54]. Presently, the modeling of the parasitic capacitances has been analysed in the field of the electrical machines in order to understand the transitory stages for a shut-down or electrical disconnection [55,56].

In the last decades, with the progress of the computational resources, the modeling and component simulation has been linked to help in the optimization design. The FEA is an adequate tool to calculate the winding parameters [57], but the current hardware computational limitations being the Random Access Memory the main constraint to manage the Finite Number in a simulation) do not usually allow a 3D simulation for non-symmetric inductors. The winding parameters extraction based on 1D or 2D FEM are not adequate to achieve the required accuracy due to the complexity of these components. In addition, a 3D model is necessary for different reasons such as to analyse of a specific magnetic effect, thermal analysis and the determination of the magnetic field distribution into the conductor.

Different approaches to obtain the electrical parameters have been developed based on FEM optimization process [58,59], original methodologies [60] or for particular components [61-63].

Different FEMs were benchmarked in [64]. Firstly, a full 3D nonlinear method in the time domain was used, then, the small signal strategy was applied to the 3D model achieving a considerable reduction of computational time. In the 3D model, the eddy currents in the laminations are fully modeled, in order to avoid 3D model, a 2D model has been also considered where the eddy currents have been included adopting a homogenization technique. In this 2D case, both nonlinear time domain simulations and small signal strategies have been implemented. The results for the described four FEM methods are in a very good agreement, proving that the small-signal strategy can be profitably used in order to reduce significantly the computational cost. The homogenization technique is based on the technique described in [65] that it is based on the lamination 1D model coupled with the FE equations to approximate the field distribution. This model is very useful for electrical machines under saturation, evaluation of the average torque considering the flux linkage contributions and identification of the torque components. This modeling method [65] was published for hybrid excitation synchronous machines that is another electrical field where FEM is extensively

used due to the complexity of the magnetic field distribution with radial/axial flux paths using magnetic equivalent circuits (MEC). A 3D FE analysis is essential in analyzing a machine with radial/axial flux paths due to the asymmetry in the axial direction. However, a 3D FEM is computationally expensive and time consuming, especially during the preliminary design stage. For 3D models, a MEC considering saturation and leakage flux distribution was designed, and the field analysis was performed. A 2D equivalent FE model via MEC was modeled and experimental results have validated this proposal.

An improved MEC considering the leakage, cross coupling and saturation effects through the performance of an integrated 3 degrees of freedom magnetic bearing analysis (3-DOF MB) is developed in [66], and if compared with the conventional magnetic component model, this proposal analyses the radial and axial control current fields together. By using this improved MEC model, it demonstrates the cross coupling effect between radial and axial directions in such integrated 3-DOF MB. The stiffnesses of the radial force is significantly influenced by the axial control current, while the stiffnesses of the axial force is independent of the radial control current.

A Quasi 3D FEM was developed in [67] by exploiting the symmetry and thus reducing the original 3D geometry to a 2D cross section. However, it is no longer possible when boundary conditions or excitations are not appropriate for the geometrical symmetry applied. To avoid a computationally expensive 3D simulation, a quasi 3D FEM has been developed which uses tensor-product shape functions combining standard finite elements in the cross-sectional plane with harmonic functions to take into account the azimuthal variation of the field. The proposed method and its convergence are validated against an analytical model. All calculations are carried out on an underlying 2D mesh which allows considerable reduction in computational effort compared to a standard 3D simulation. The spectral discretization converges exponentially, whereas the FE discretization converges to a polynomial (Figure 16).
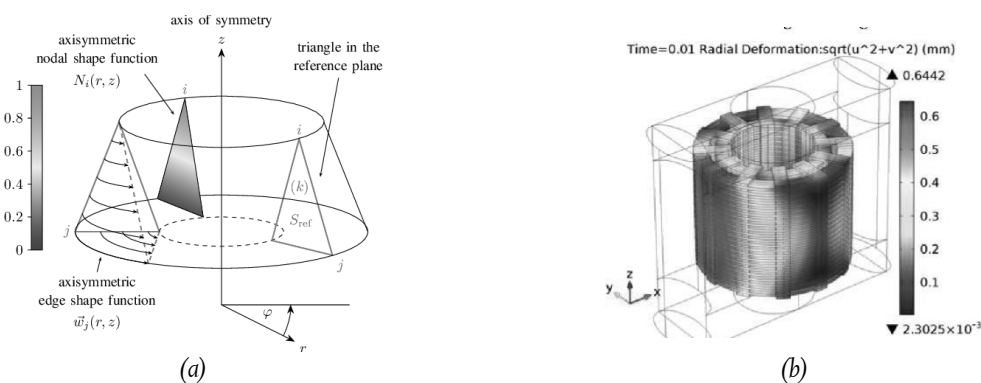

Figure 16. Different steps in the research for the winding loss (a) Quasi-3-D Finite-Element Method for Simulating Cylindrical Induction-Heating Devices [71] (b) Deformation process for the windings [69].

A new model for magnetic flux of multi-winding Toroidal core high frequency Transformers using 3D reluctance network model was shown in [68]. This work shows a 3D reluctance network that is introduced to model the magnetic flux distribution and estimates the self and leakage inductances of multiwinding toroidal core high frequency transformer. The model is compared with experimental results to verify the accuracy of the proposal.

A new step forward was done in [70], where a novel 3-D hybrid analytical modeling (HAM) method proposes integrating a mesh-based 3D MEC model into a 3D Fourier modeling. This HAM is capable of predicting the electromagnetic field distributions for Cartesian 3D structures. A generalized approach technique is applicable to a wide range of electromagnetic devices, such as linear and planar actuators where the 3-D HAM calculates the magnetic field distributions and forces with approximately 90% accuracy.

One of the last important improvements in the field of the FEMs has been the inclusion of the deformation transient process during short-circuit faults shown in Figure 16 [64]. A 3D geometric simulation is developed based on the actual size parameters of a 500 kV single-phase two windings transformer. The multi-physic-field coupling technique based on the FEM has been employed to calculate the dynamic deformation characteristics of transformer winding structures during the transient process. The simulation results indicate that the windings can withstand the most severe impacts caused by external shorts-circuits without any plastic deformation. Consequently, the winding structure in the middle-height position near the ferromagnetic circuit should be checked and strengthened to prevent windings from plastic deformation and radial instability.

Currently, FEM are focused in the thermal analyses of the magnetic components [71] and electric equivalent parameters extraction methods by using FEMs [72].

2.5.1 *Summary of the models*

The state of the art concerning the computational limitations to analyze the magnetic components using 3D models, pseudo 3D models, hybrid models and analytical solutions is described in this section.

At this point, there is no equivalent circuit (electrical and magnetic) consider all the effects in 3D without paying a high computational time cost.

The models presented in section 1.4 are usually applied for determined geometries and they are not useful for generic non-symmetric components with the various of topologies and working conditions used for inductive components in power converters.

Chapter 2. Magnetic component modeling

In addition, it assumes that the core is not in saturation and it has a linear behaviour, but there is no issue because this state for the core is normal for switcher sources and a linear permeability can be used in the analysis.

In consequence, there is not currently a 3D model taking into account all frequency effect based on FEA to obtain an electrical equivalent circuit using an operative CPU time for the power engineers in the optimization process of the magnetic components.

Table 5. Selected research papers dealing with equivalent electrical circuits

Contribution	Year							
	1989	1990	1991	2011	2016	2017	2019	2020
Proposition of an Equivalent Circuit	[28]	[39]						
Analogy between Magnetic and Electric circuit			[40]					
Equivalent circuit valid for harmonics				[38]				
Introduction of parasites capacitances for transient analyses					[55]	[56]		
Addition of the frequency and Mutual Coupling						[42] [43]		
Different Approach for Planar Coils							[44]	
Different Approach for Spiral Coils							[45]	
Currents not concentrated in a given point								[41]

Table 6. Selected research papers dealing with FEM analysis of magnetic components from 2015

Contribution	Year				
	2015	2016	2017	2018	2019
2D-3D hybrid modeling	[70]				
FEM original approaches		[58]			
3D methods for particular magnetic components		[61]		[58]	
Homogenization technique for FEM			[65]		
Quasi 3D Model				[62]	
Thermal analyses					[71]
Practical parameter extraction					[68]

2.6 Computer limitations in 3D modeling

Not every magnetic component can be solved by 3D FEA because there are some hardware computer limitations that cannot allow performing the simulation in 3D or finishing the simulation in operative CPU time. One of the solutions for this issue is the use of 2D model for simulating the magnetic components, however, non-symmetric components are not valid the simulations in 2D [73].

A 3D model is necessary for different reasons: analysis of an asymmetric component, study of specific magnetic effects, thermal and electromagnetic analyses and determination of the magnetic field distribution inside of the winding conductors. The analysis to determine the hardware computer limitation can be divided in two branches:

- Determination of the maximum number of FE managed by the computer resource [74]. This number will mainly depend on the computer memory. The core processor is a not the real limiter, however it has influence in the execution time for running the simulation of the magnetic component.

- Identification of the potential model simplifications to obtain the simulation convergence and reducing the computation stress [75].

Any simulation process in a FE tool is determined by the convergence criteria (Appendix III) that defines the maximum FE number used for the electromagnetic analysis. The convergence, in a FEM tool, is usually calculated from the difference of energy between two iterations: after one iteration is completed in the simulation, the energy error values are used for determining if additional iterations are needed to increase the solution accuracy.

Thus, the FE number used in the last iteration is available to be known, even the convergence has not been achieved. Thus, according to the energy error, it could predict the FE number that leads to any magnetic component to achieve the convergence of any magnetic component simulation [73,74].

In the next sections, two magnetic components are studied in detail by analysing different sequences when only one parameter is modified to know the influence of this parameter in the values obtained for the different electrical parameters of the magnetic component equivalent circuit (MCEC).

2.6.1 *Simulation Analysis*

This work is focused in the non-symmetric magnetic components that need 3D models to be analysed. The selected models for this work are inductors with EE and Toroidal cores because they are commonly used for inductive components in power converters and they have no 3D symmetry depending in the winding strategy. Thus, the two inductive components used in these studies to analyse the computer limitations are shown in detail in the Table 7 and Table 8.

Three different simulation sequences were launched to define the computer limitation and model parameters involved in the problem and to predict the FE number needed for a complete 3D simulation of the magnetic component.

Table 7. Summary of EE core data
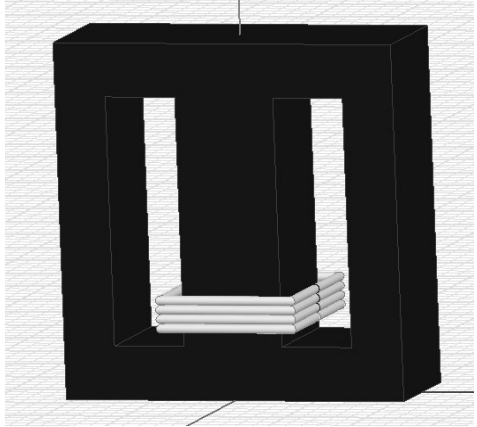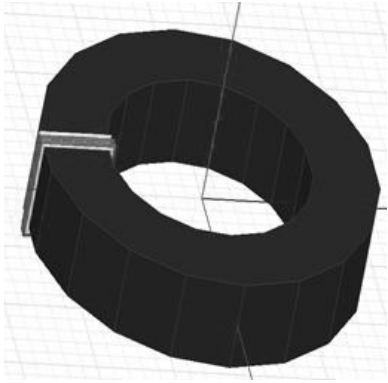
Core	Manufacturer: FerroxCube [76] Geometry: EE Core with rectangular section Geometry specification: EE/42/21/15 Material: 3C90 Relativity Permeability:40	
First winding	Diameter of the conductor: AWG 24 Conductor material: Copper Number of turns: 4	
Second winding	Diameter of the conductor: AWG 18 Conductor material: Copper Number of turns: 4	

Table 8. Summary of Toroidal core data

Core	Manufacturer: FerroxCube [76] Geometry: Toroidal Core with rectangular section Geometry specification: C107/65/25 Material: 3C90 Relativity Permeability:40	
First winding	Diameter of the conductor: AWG 24 Conductor material: Copper Number of turns: 4	
Second winding	Diameter of the conductor: AWG 18 Conductor material: Copper Number of turns: 4	

2.6.2   *Impact of the geometrical parameters for the FE number*

The study in this section determine which geometrical and material features could impact in the FE number required for obtaining a result with the desired accuracy using a given computer resource. The analysis consists on the permutation of these parameters (number of winding turns, winding current, core size and air-gap dimension) from the original models presented in the previous section to determine the number of FE increase from each parameter separately [73,74].

The FEM simulation was set up with an estimated error of 1% and 5% with a maximum of 40 iterations in the simulation. At this stage of the study, any simplification is applied to the component.

It can be concluded from [74] that the main parameter that determines the increase of the FE number is the winding turns in the coil.

Table 9 shows the increase of the number of FE depending on the windings turns (EE core) being the limit for the component model 15 windings because the convergence is not available with this number of the windings. Figure 17 shows the evolution of the number of FE vs. CPU time.

Table 10 and Figure 18 show a similar analysis for the Toroidal core inductive components using the same computer resource.

Table 9. Summary of FE number required EE Core Component Simulation

Turns	Total Tetra (FE)	Air Tetra (FE)	Core Tetra (FE)	Winding Average (FE)	Energy Error (%)	Delta Error (%)	CPU Time (s)
4	402,806	213,520	15,662	21,703	0.6	0.8	3,742
5	501,75	260,959	17,120	22,350	0.8	0.2	3,877
6	607,086	311,380	20,191	22,960	0.5	0.1	5,745
7	707,113	362,333	21,379	23,100	0.6	0.6	8,285
8	811,411	406,290	23,193	23,871	0.5	1.0	9,660
9	912,224	456,616	27,216	23,800	0.5	0.7	11,030
10	1,021,211	507,418	28,678	24,256	0.4	0.2	12,066
11	1,119,785	558,969	28,859	24,180	0.5	0.3	13,784
12	1,227,119	602,976	30,179	24,749	0.38	0.13	16,854
13	1,329,032	653,364	32,253	24,747	0.4	0.2	19,924
14	1,436,020	700,197	36,691	24,969	0.4	0.8	26,676
15	1,531,421	756,312	34,562	24,685	0.3	1.1>1	NOT
16	1,256,051	652,715	19,135		1	3.8>1	NOT
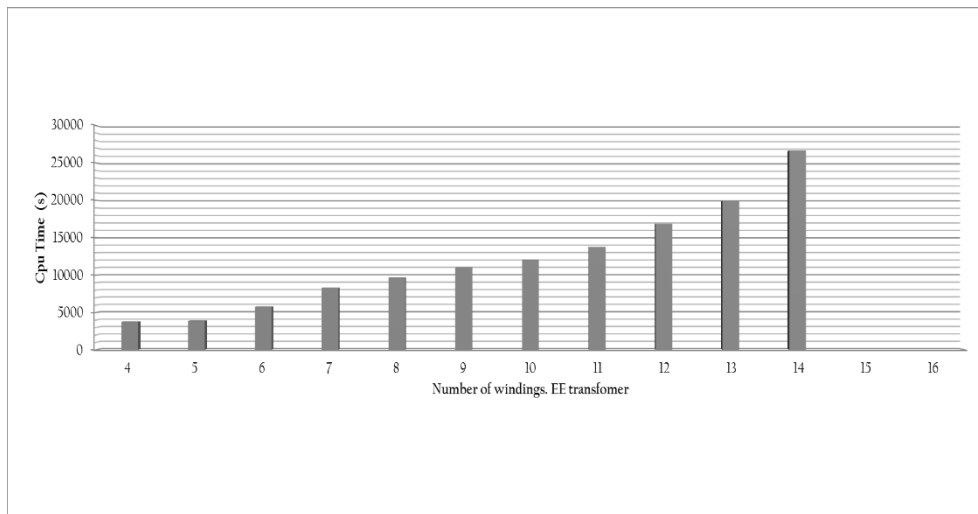
Figure 17. CPU time versus number of turns in EE core.

Table 10. Summary of data corresponding to Toroidal core FEA analysis using Hexagonal Section.

Features	Values				
Turns (FE)	4	8	12	16	56
Total Tetra (FE)	18,248	58,793	52,506	201,498	249,457
Air Tetra(FE)	13,148	44,742	37,687	151,655	170,582
Core Tetra (FE)	720	4,720	2,008	24,493	15,232
Winding Average (FE)	5,475	583,188	533,792	792,188	198,884
Energy Error(%)	0.36714	1.612	0.61018	0.55139	0.02937
Delta Error(%)	0.43953	1.325	1.411	1.4845	0.18275
CPU Time (s)	15	71	62	338	618

(a)

(b)
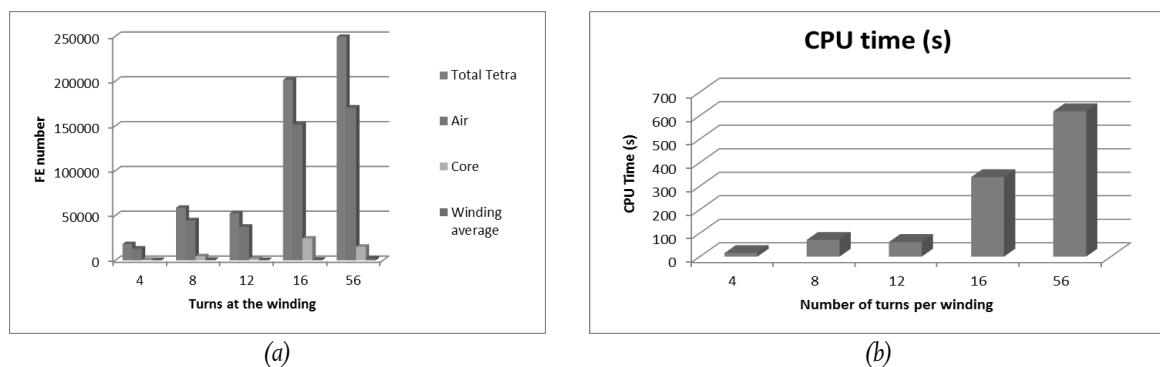
Figure 18. (a)CPU time for Toroidal core (turns per winding) FE number evaluation (b) CPU time evaluation.

2.6.3 *Impact of the conductor cross-section in simulations*

This dedicated analysis was developed following the same procedure as in the previous section, but the original model contains the simplification assumed in [73], where the

conductor cross-section of the windings does not have a circular shape but a polygonal shape has been used for the reduction of the number of FE in the component simulation and CPU Time saving.

Table 10 shows the distribution of the FE in the component model depending of the polygonal conductor cross-section used in the windings. The number of the FE increases in the air zone around of the windings because of the surface approximation technique in Maxwell Ansys [77]. The mesh methodology depends on the surface approximation technique for the object surfaces.

To create a finite element mesh, Maxwell tool first divides all true surfaces (the original ones) into triangles, these triangulated surfaces are called faceted surfaces because a series of straight line segments represents each curved or planar surface (Figure 19).

For planar surfaces, the triangles lie exactly on the model faces, there is no difference in the location or the normal of the true surface and the meshed surface. When an object´s surface is non-planar, the faceted triangle faces lie a small distance from the object´s true surface. This distance is called the surface division, and it is measured in the model´s units. The surface deviation is greater near the triangle centres and less near the triangle vertices.

The normal direction of a curved surface is different depending on its location, but it is constant for each triangle. The angular difference between the normal of the curved surface and the corresponding mesh surface is called the normal deviation. The aspect ratio of triangles used in planar surfaces is based on the ratio of circumscribed radius to the in-radius of the triangle. It is unity for an equilateral triangle and approaches infinity as the triangle becomes thinner. This is the reason that polygonal cross-section with more than 24 edges have more FE number than circular sections (Figure 20).
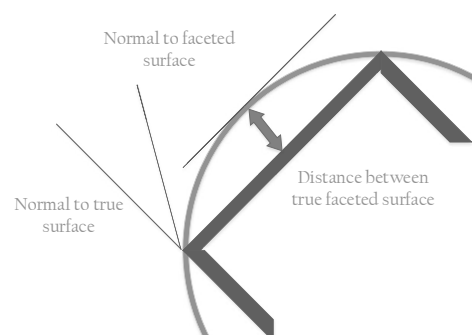
Figure 19. Approximation Surface in the Meshing [78].

Chapter 2. Magnetic component modeling

Table 11.Summary of EE core FEA analysis

	Hexagon	Dodecagon	Octadecagon	Circle	Polygon 24 edges	Polygon 36 edges	Polygon 48 edges
Total Tetra (FE)	34,300	160,837	331,428	402,806	504,030	659,629	1,176,051
Air Tetra (FE)	24,295	100,227	187,004	213,520	257,656	339,744	570,251
Core Tetra (FE)	5,577	19,857	34,422	15,662	45,563	18,183	26,417
Winding Average (FE)	5,535	5,094,125	1,375,025	21,703	251,01,375	3,771,275	72,422,875
Energy Error (%)	0.39065	0.25575	0.22826	0.5937	0.16952	0.67739	0.54051
Delta Error (%)	0.14453	0.069121	1.4228	0.75958	0.26949	0.94505	1.9237
CPU Time (s)	43	710	1,695	3,742	3,467	5,781	12,401
Time Portion	1	16,5	39,4	87	80	134	288
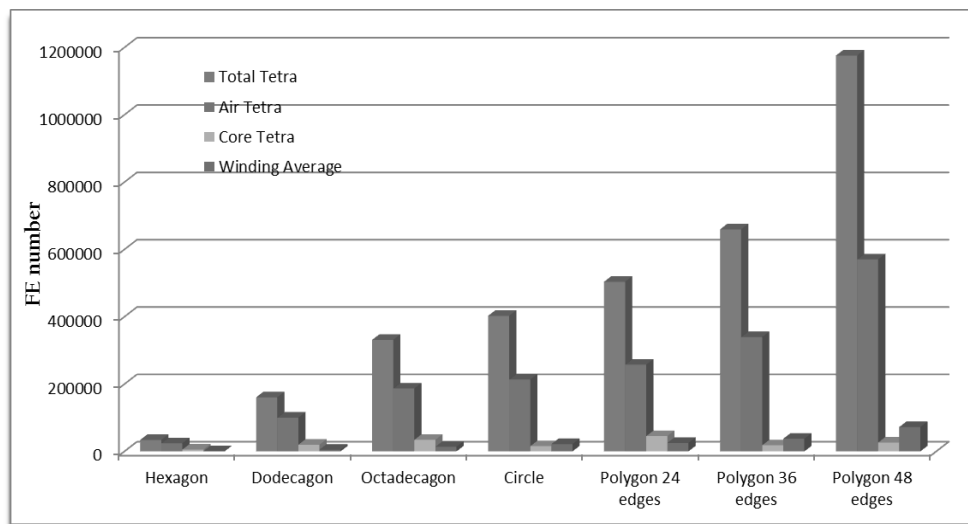
Figure 20. Comparison of FE number for different coil cross-section in the case of a EE core .

Figure 20 shows the graph corresponding to the Table 11, showing that the total FE is increasing depending on the number of the edges in the conductor cross-section due to the major impact in the air zone. This increase is the main reason for the evolution of the total number of the FE varying the edges of the polygon. Figure 21 is a similar graph for the CPU time required for running each simulation.

A similar analysis for the Toroidal core component (Table 8) has been done and the results are summarised in Table 12, Figure 22 and Figure 23. As the procedure is similar for the EE core component, only the circle and hexagon for the cross-section has been analysed.
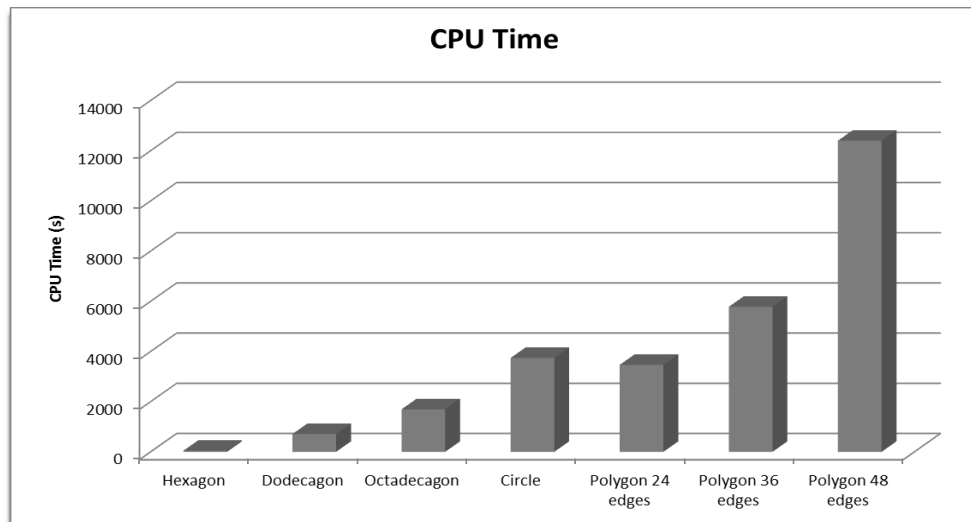
Figure 21. Comparison of CPU time among different coil cross-section for EE core .

Table 12. Summary of Toroidal core FEA analysis

	Hexagon	Circle
Total Tetra (FE)	18,248	435,685
Air Tetra (FE)	13,148	249,649
Core Tetra (FE)	720	13,091
Winding Average (FE)	5,475	21,618,125
Energy Error (%)	0.3671	0.13631
Delta Error (%)	0.4395	0.39149
CPU Time (s)	15	1.030
Total Time (s)	18	1.062
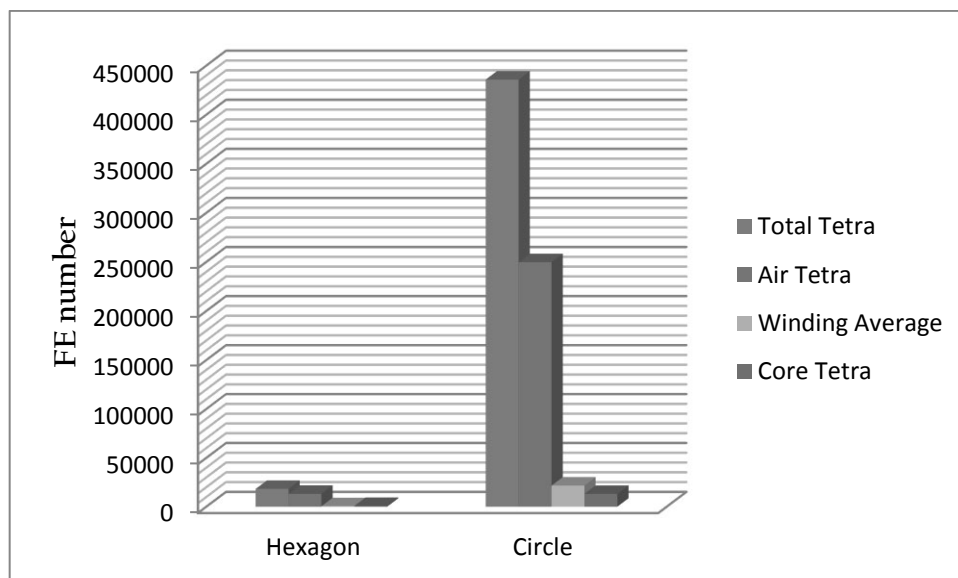
Figure 22. Comparison of FE number for different coil cross-section (Toroidal core case).
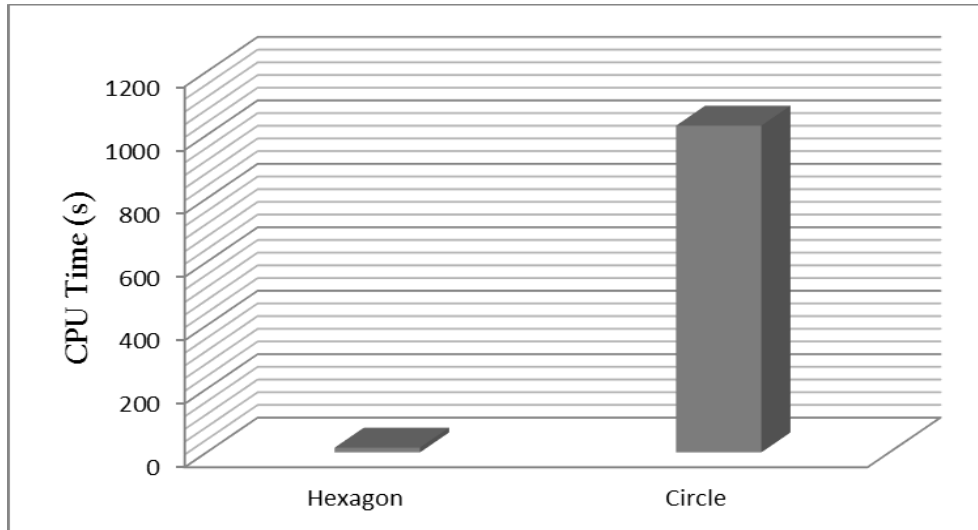
Figure 23. Comparison of CPU time for different coil cross-section (Toroidal core case).

As Figure 22 and Figure 23 show, the conductor cross-section changes can increase the FE numbers in the simulation up to the impossibility of the simulation completion. In addition, it can be concluded that the results indicate that the hexagonal section is the best choice as a simplification according to the FE number and the CPU time saving. Another result obtained from this study is that there is not any simulation than can manage more than 1,600,000 FE for 4 Gb RAM computer (Appendix IV).

2.6.4 *Impact on the winding electrical parameters*

This section is devoted to analyse the evolution of the resistance and inductance values for different models varying the conductor cross-section used for simulation of the two considered inductive components (EE and Toroidal cores) when the winding turns are varied shown from Figure 24 to -Figure 31.

The analyses are focused in the main parameters for the electrical equivalent circuit [9] for an inductive component. These parameters are the resistance (R) and the inductance (L) of the windings. The values of the parameters when the conductor cross-sections are different in low frequency due to the conductor areas are different as well. In high frequency, these differences are bigger because of the different influence of the skin and proximity effects in circular and polygonal sections. Thus, the geometrical simplifications applied to the component are not adequate for the electrical parameter extraction. The figures demonstrate that there is an additional step to calculate the AC resistance from a model that uses a polygonal cross-section for the windings. This logic from this sequence analysis is due to the difficulty to achieve the complete simulation of complex geometries. For this reason, it is necessary to know which

component simplifications are more useful to achieve the convergence or which elements of the component produces bigger increments in the FE in the model. This analysis starts with one winding till it reaches the number of the windings where the computational limitation is achieved for the analysed components (EE and Toroidal core) to determine the difference of results for the different electrical parameters in DC and in AC and to investigate its influence on the error obtained with the simplified model.

2.6.5 *Conclusions*

According to the analyses developed in this chapter, some simplifications are needed in the magnetic component model to be able to run the simulation in a 3D FE tool.

As it has been demonstrated (Table 9-Table 12), the FE of the magnetic component depends on the air zone finite element that are created around the windings. Therefore, the most critical design aspect for the CPU Time is the conductor cross sections for the windings. Also, the analyses sequence has confirmed a linear relationship between the required CPU time and the FE number [74], being the most effective cross section the hexagonal one.

The hexagonal section for the conductors has different value for the electrical parameters (resistance and inductance) in low frequency because the conductor area and the distance between conductors are different (this variable is very sensible for the inductance calculation). At high frequency, the skin and proximity effects have different impacts in circular and polygonal sections and the difference between these values are bigger.

In conclusion, the hexagonal section for windings is the most operative choice for design engineers, however, a correction factor is needed to achieve the same results using circular cross-sections. This correction factor will be determined in the following chapter as an original contribution from this work.

Chapter 2. Magnetic component modeling

EE core. First winding (1 turn) and Second Winding (1 turn)
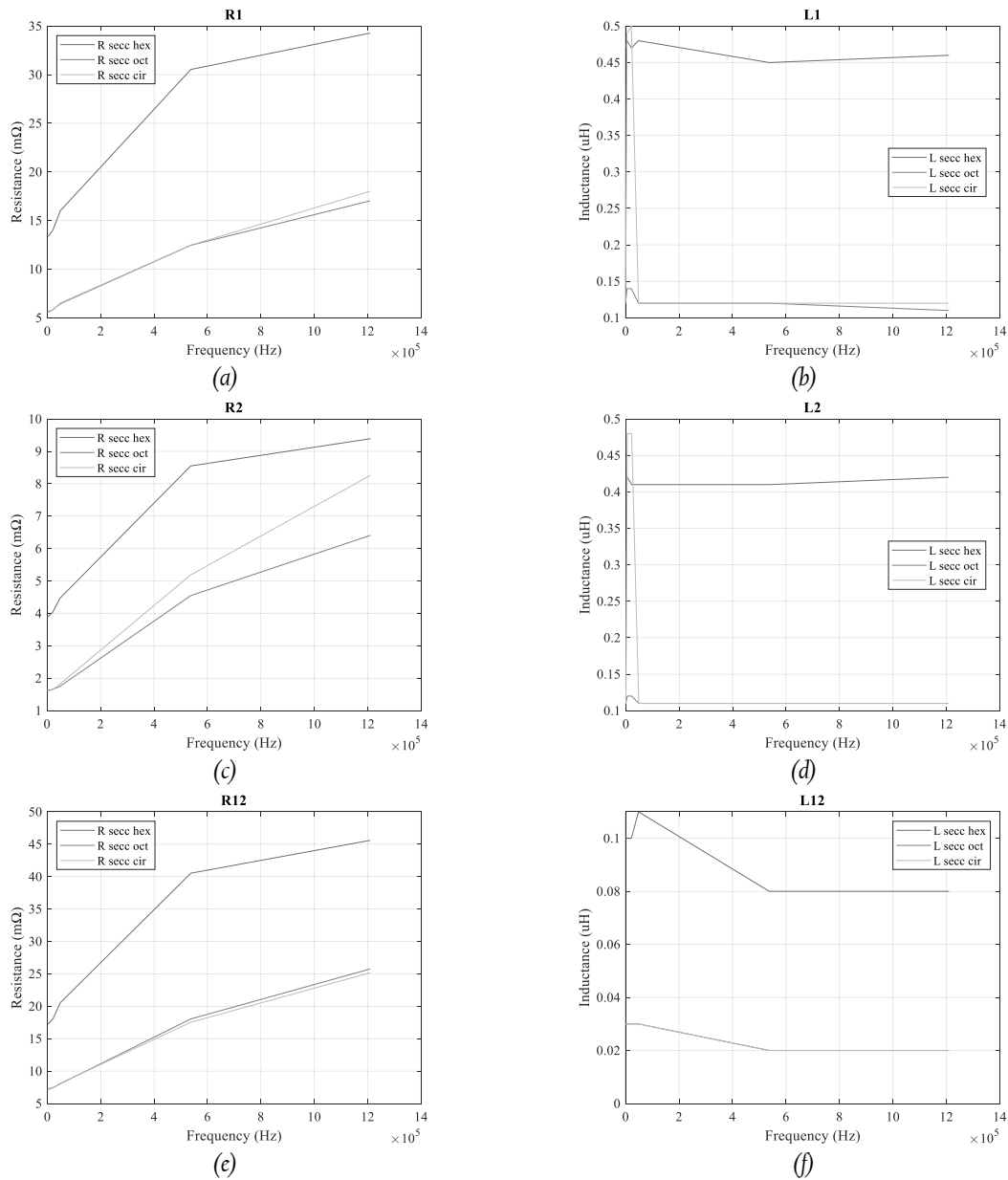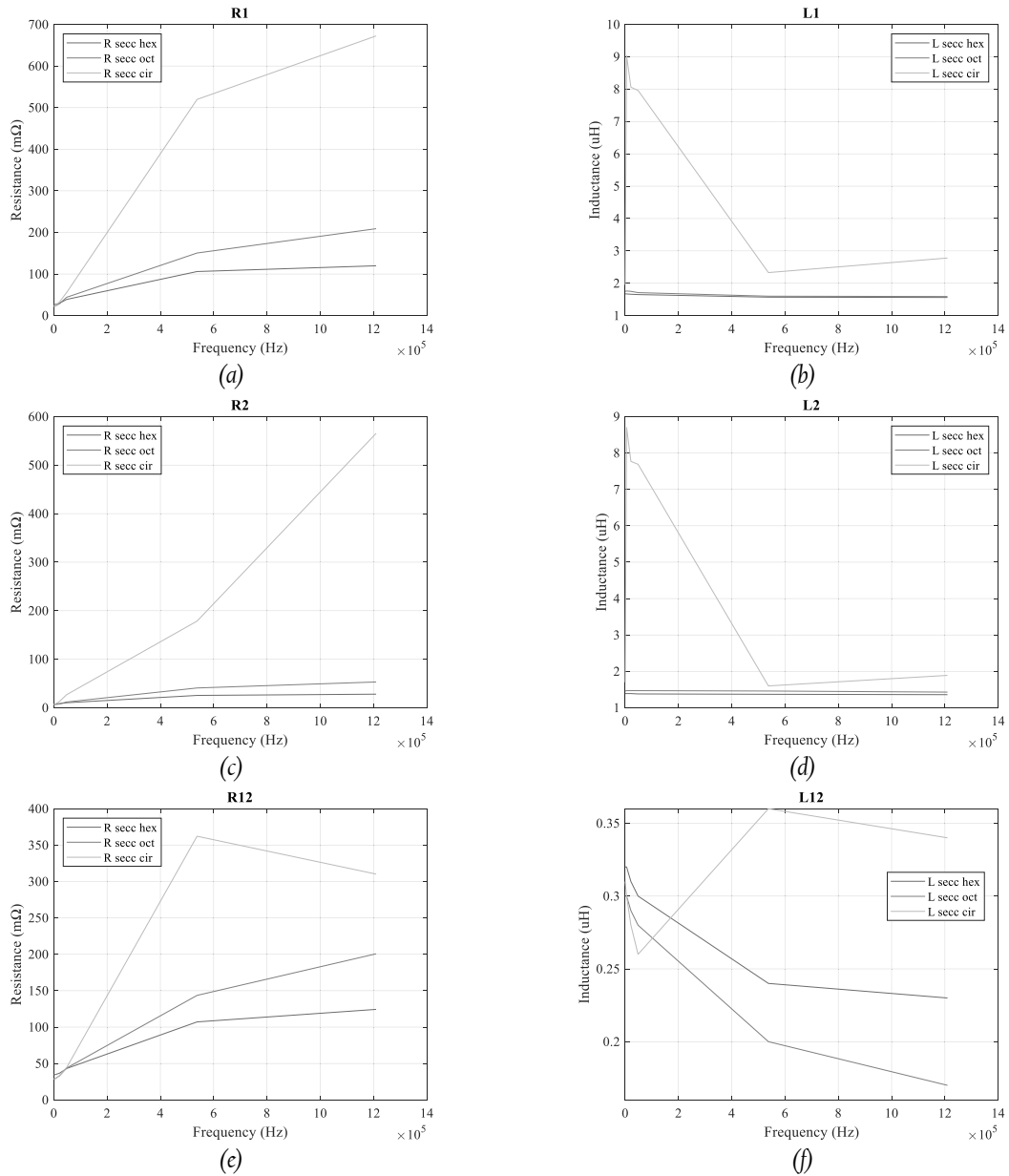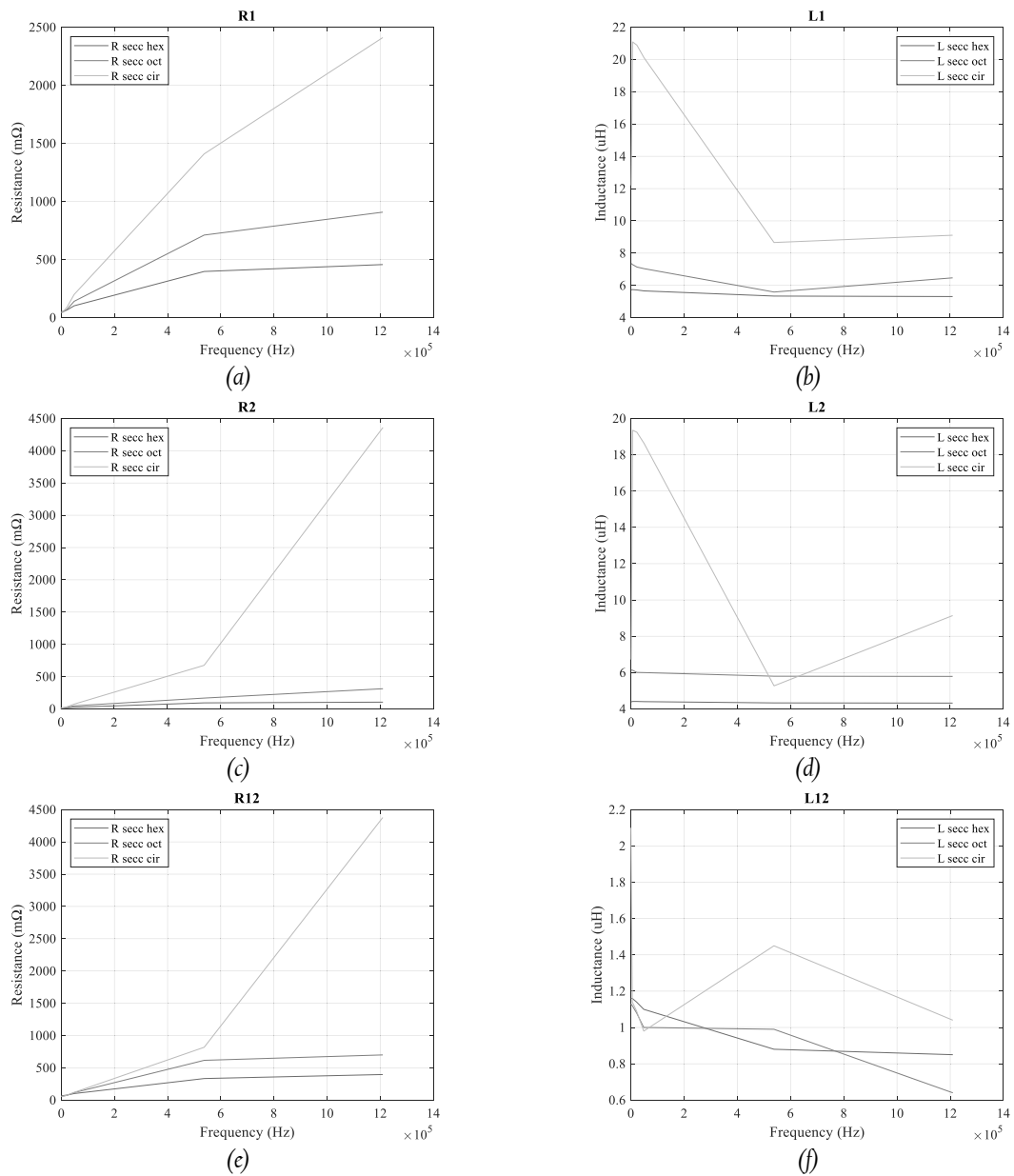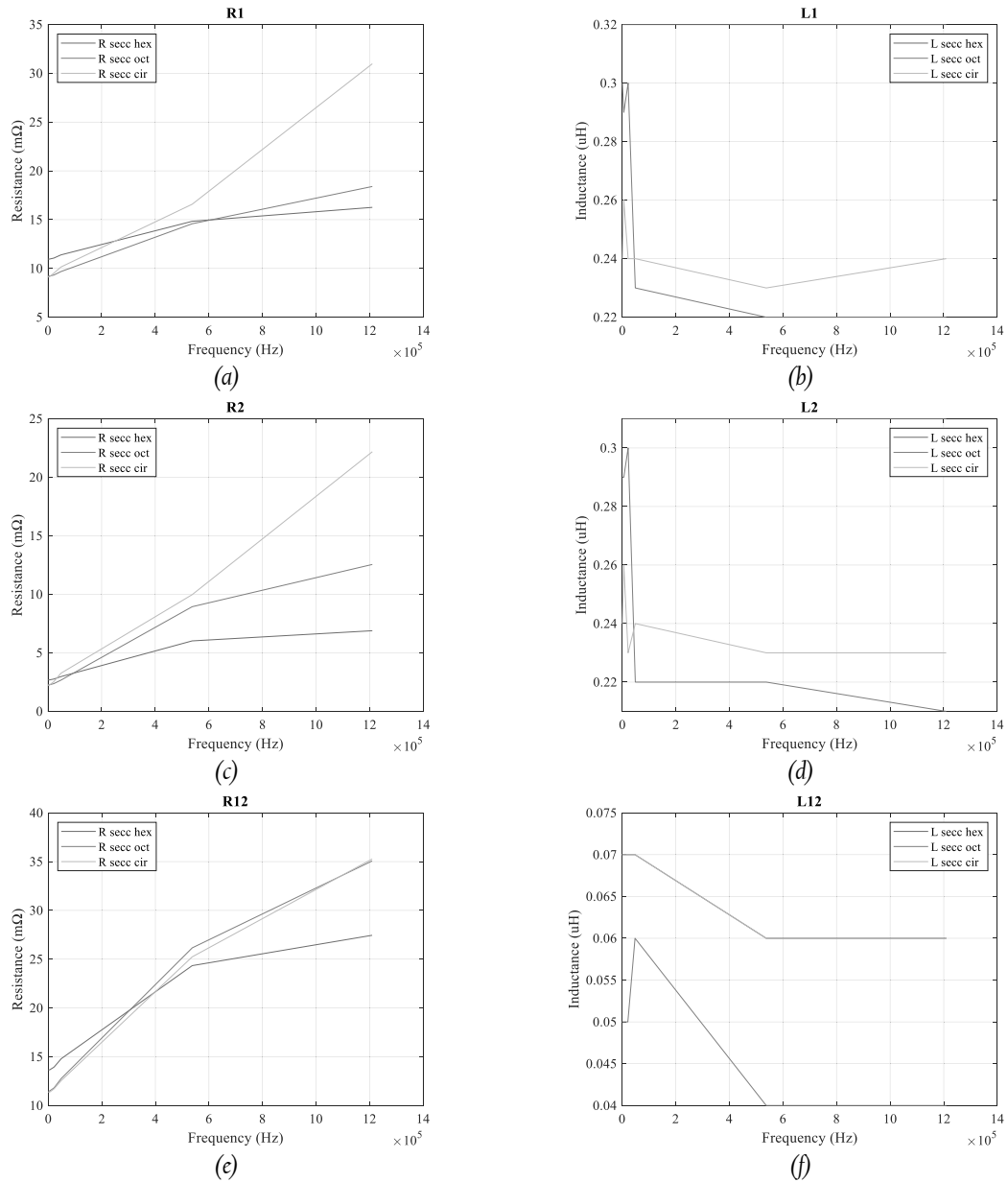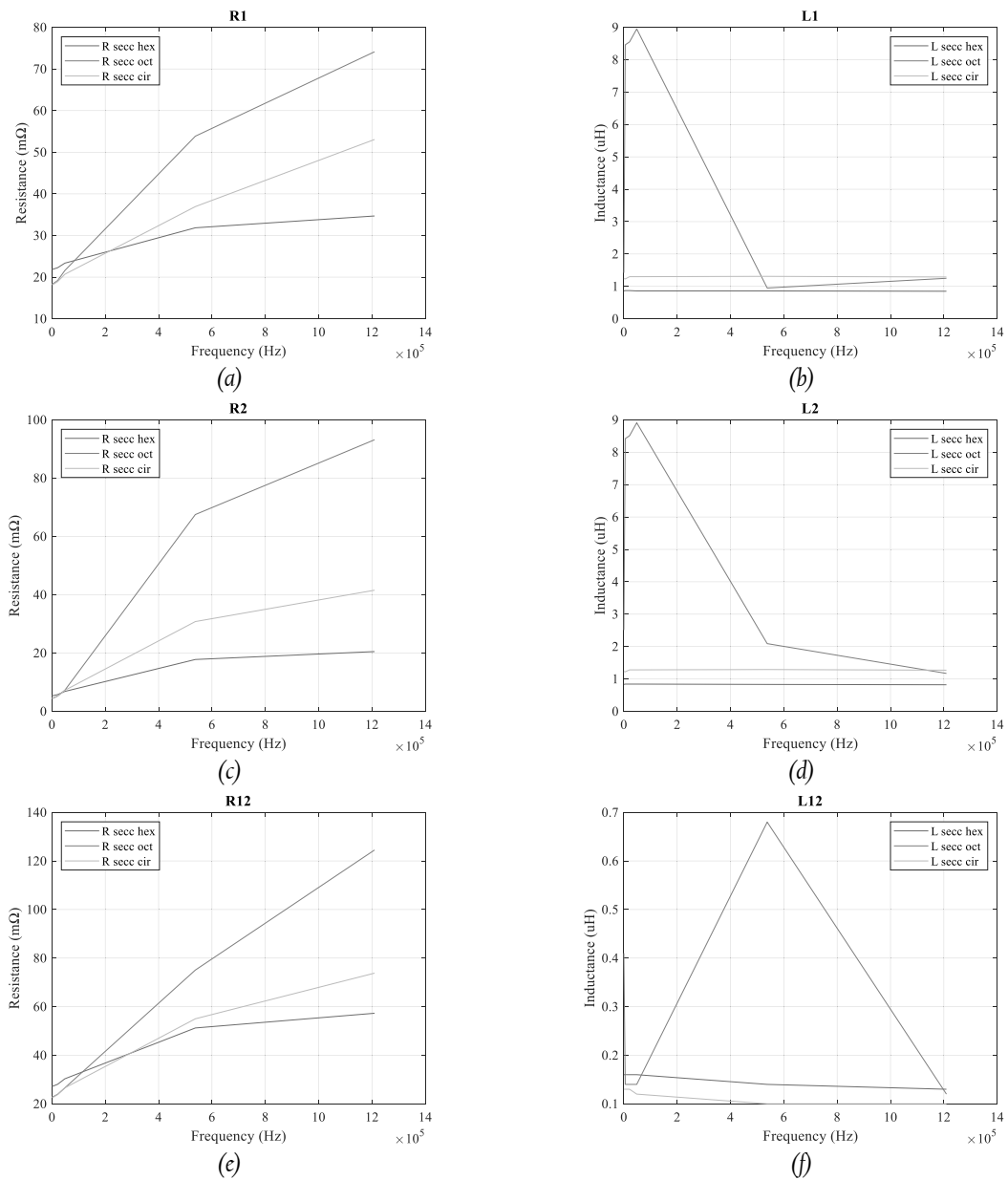

Figure 24. EE transformer. 1 winding (a) Resistance of first winding (R_1, AWG 24) (b) Inductance of first winding (R_1, AWG 24) (c) Resistance of second winding (R_1, AWG 18) (d) (b) Inductance of second winding (R_1, AWG 18) (e) Resistance R_{12}, working as transformer equivalent circuit [9] (f) Inductance L_{12}, working as transformer equivalent circuit [9].

EE core. First winding (2 turn) and Second Winding (2 turn)
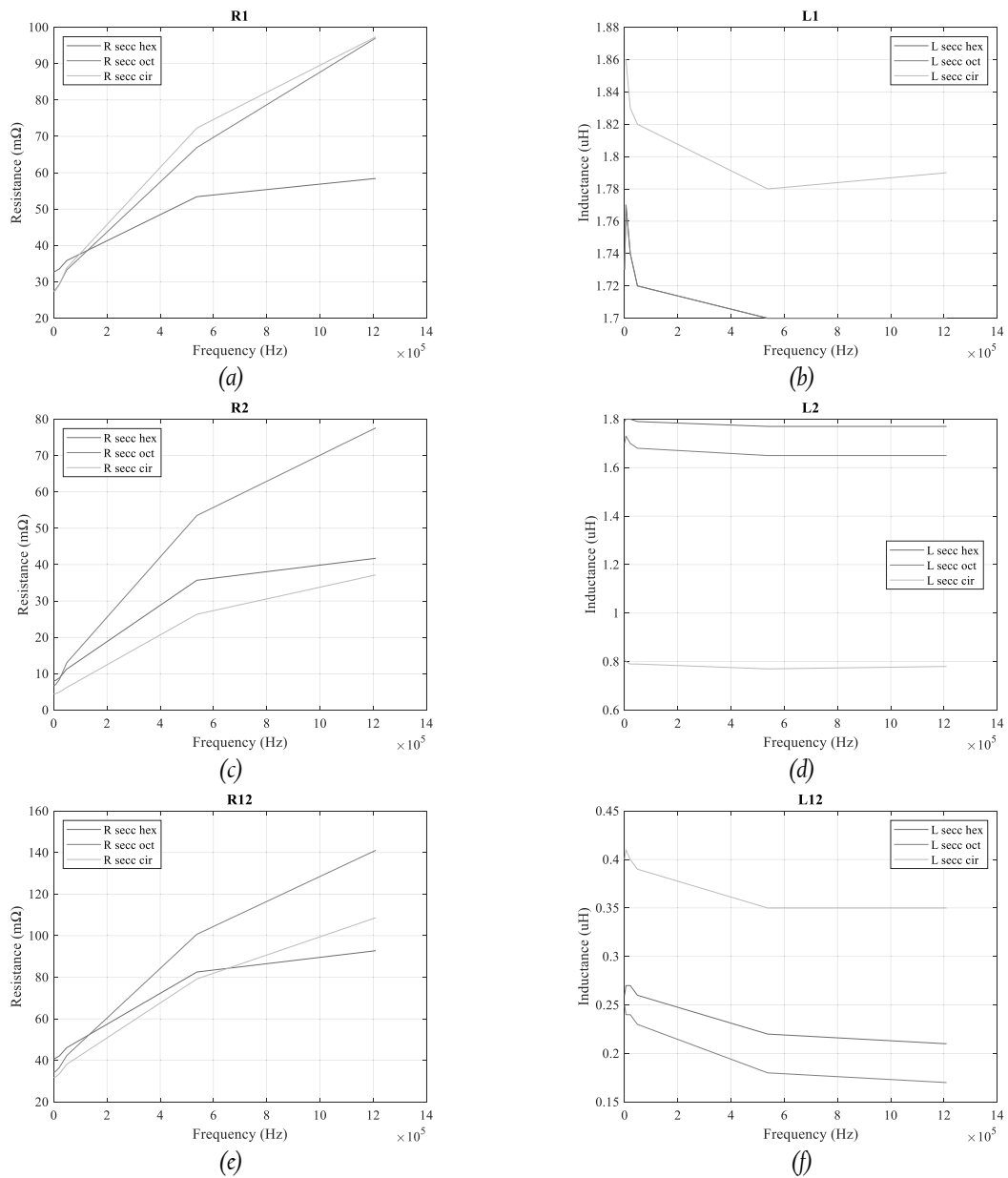

(a)

(b)

(c)

(d)

(e)

(f)
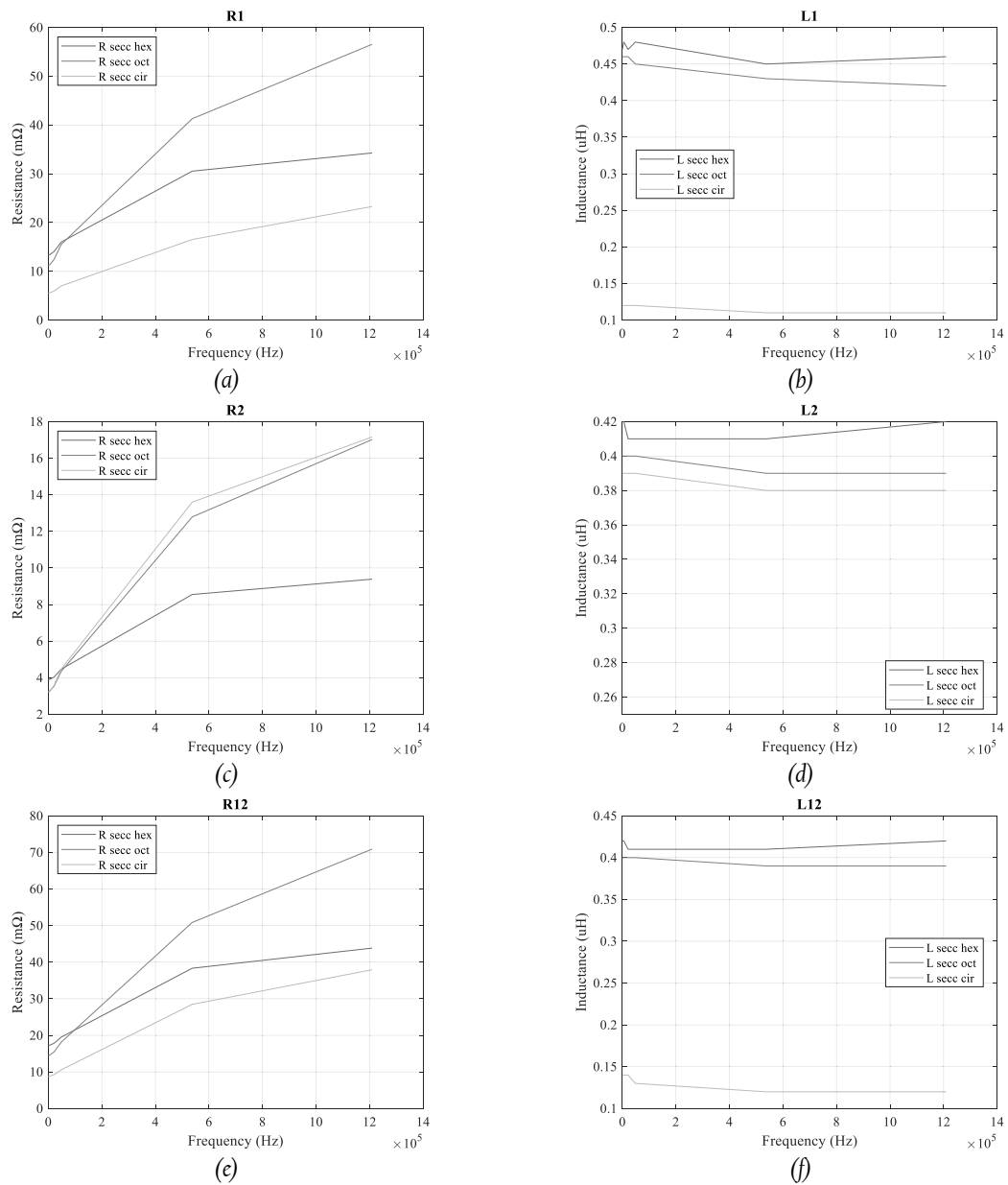
Figure 25. EE transformer. 2 windings (a) Resistance of first winding (R₁, AWG 24) (b) Inductance of first winding (R₁, AWG 24) (c) Resistance of second winding (R₁, AWG 18) (d) (b) Inductance of second winding (R₁, AWG 18) (e) Resistance R₁₂, working as transformer equivalent circuit [9] (f) Inductance L₁₂, working as transformer equivalent circuit [9].

Chapter 2. Magnetic component modeling

EE core. First winding (4 turns) and Second Winding (4 turns)

(a)

(b)

(c)

(d)

(e)

(f)

Figure 26. EE transformer 4 windings (a) Resistance of first winding (R₁, AWG 24) (b) Inductance of first winding (R₁, AWG 24) (c) Resistance of second winding (R₁, AWG 18) (d) (b) Inductance of second winding (R₁, AWG 18) (e) Resistance R₁₂, working as transformer equivalent circuit [9] (f) Inductance L₁₂, working as transformer equivalent circuit [9].

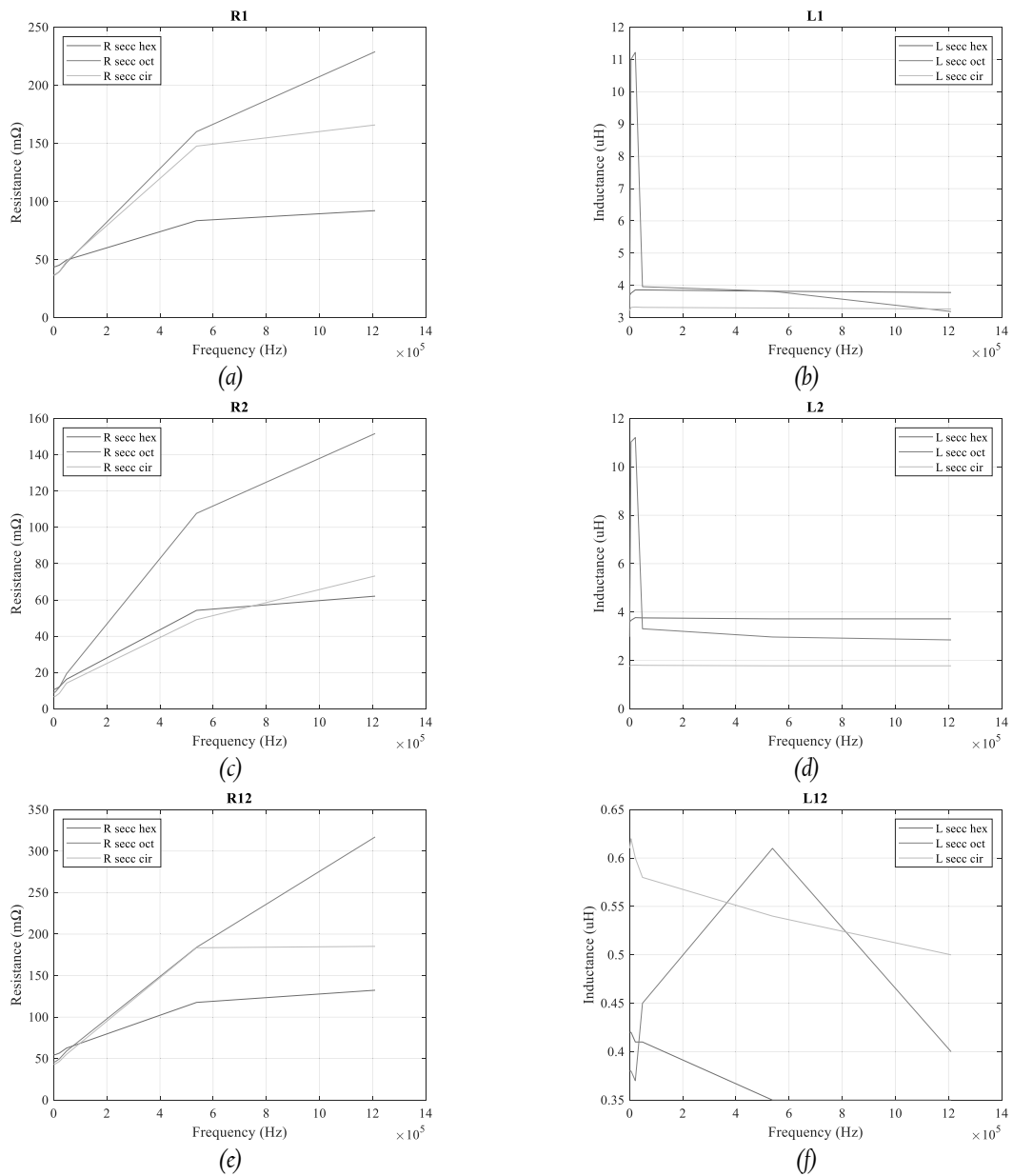EE core. First winding (8 turns) and Second Winding (8 turns)

(a)

(b)

(c)

(d)

(e)

(f)

Figure 27. EE transformer 8 windings (a) Resistance of first winding (R_1, AWG 24) (b) Inductance of first winding (R_1, AWG 24) (c) Resistance of second winding (R_1, AWG 18) (d) (b) Inductance of second winding (R_1, AWG 18) (e) Resistance R_{12}, working as transformer equivalent circuit [9] (f) Inductance L_{12}, working as transformer equivalent circuit [9].

Chapter 2. Magnetic component modeling

Toroidal core. First winding (1 turn) and Second Winding (1 turn)

Figure 28. Toroidal core. 1 winding (a) Resistance of first winding (R_1, AWG 24) (b) Inductance of first winding (R_1, AWG 24) (c) Resistance of second winding (R_1, AWG 18) (d) (b) Inductance of second winding (R_1, AWG 18) (e) Resistance R_{12}, working as transformer equivalent circuit [9] (f) Inductance L_{12}, working as transformer equivalent circuit [9].

Toroidal core. First winding (2 turns) and Second Winding (2 turns)

(a)

(b)

(c)

(d)

(e)

(f)

Figure 29. Toroidal core. 2 windings (a) Resistance of first winding (R₁, AWG 24) (b) Inductance of first winding (R₁, AWG 24) (c) Resistance of second winding   (R₁, AWG 18) (d) (b) Inductance of second winding (R₁, AWG 18) (e) Resistance R₁₂, working as transformer equivalent circuit [9] (f) Inductance L₁₂, working as transformer equivalent circuit [9].

Chapter 2. Magnetic component modeling

Toroidal core. First winding (3 turns) and Second Winding (3 turns)

Figure 30. Toroidal core. 3 windings (a) Resistance of first winding (R_1, AWG 24) (b) Inductance of first winding (R_1, AWG 24) (c) Resistance of second winding (R_1, AWG 18) (d) (b) Inductance of second winding (R_1, AWG 18) (e) Resistance R_{12}, working as transformer equivalent circuit [9] (f) Inductance L_{12}, working as transformer equivalent circuit [9].

Toroidal core. First winding (4 turns) and Second Winding (4 turns)

(a)

(b)

(c)

(d)

(e)

(f)

Figure 31. Toroidal core. 4 windings (a) Resistance of first winding (R_1, AWG 24) (b) Inductance of first winding (R_1, AWG 24) (c) Resistance of second winding (R_1, AWG 18) (d) (b) Inductance of second winding (R_1, AWG 18) (e) Resistance R_{12}, working as transformer equivalent circuit [9] (f) Inductance L_{12}, working as transformer equivalent circuit [9].

3 Proposed electrical equivalent circuit based on 3D FEM

This chapter presents the new electrical parameters extraction procedure based on the 3D FEM. The principles and limitations of the model are described as well as the methodology to obtain the procedure and the original correction factor used in the result-processing. At the end of the chapter, the experimental validation is shown for several magnetic components as well as a guide to use this proposed procedure for power engineers.

3.1 Electrical equivalent circuit

The proposed MCEC is adequate for any of magnetic component (transformers, inductors, non-gapped and gapped ceres) and takes into account frequency and geometry effects such as skin, proximity, interleaving and edge effects. The impedances in this model represent not only the self-terms, but also all mutual terms shared between the windings. The parameters of these self and mutual impedances are frequency dependent, and thus the model represents the frequency behaviour of windings in detail. Also these parameters determine the efficiency of the inductive component and operation capabilities of the power converters (as in the voltage boost factor) which define their performance. In addition, the procedure based on 3D FEM needs a very low computer resources compared with the current mainframes.

3.1.1 *Frequency effect*

The fact that frequency affects the behaviour of magnetic components is widely known. The analysis of magnetic components may become quite difficult since the component depends on the operation frequency and the geometrical model parameters.

For some components, it is possible to use 1D and 2D models due to the magnetic field density symmetry and the equations can be derived for parasitic components, losses, and energies [9,12].

However, as explained in Chapter 2, complicated geometries imply that it becomes almost impossible to derive analytical equations that describe the behaviour of the components. Also, due to the computer limitations a 3D FEA is not available without simplifications in the original model. Despite this issue, a systematic methodology for generating a 3D model for a magnetic component by means of a FEA tool is needed. The original proposed methodology takes into account the frequency dependency of the electrical parameters as well as the frequency effects only studied in a 3D model. As the parameters of the model are frequency dependent, the model is valid to work with non-sinusoidal currents, applying superposition to the Fourier's terms of the current, and then the behaviour of the components working with these currents can be represented if no core saturation is presented and the superposition theorem can be applied as it is explained in the following section.

3.1.2 *General modeling principles*

The main principle, which the equivalent circuit is based on, is the linear behaviour of the system. This assumption is very important to determine the limitations and the advantages of the proposed model.

One of the most important advantages is the use of the superposition theorem for deriving the values of the electrical parameters extracted from FEA. This theorem is applied to magnetic fields and current densities and it is not possible to apply it to energies and losses. The only nonlinear piece of a magnetic component as far as current is concerned is the core of the magnetic component because of the saturation status of the material.

A constant value of permeability has been used in the FEA simulations in order to apply this theorem. This model is accurate in the linear core behaviour zone, if nonlinear core behaviour appears, the model for windings is not correct because the field distribution changes [9]. This is not an important issue because the power converters usually work in the linear zone and additionally, the following chapter is dedicated to the core losses analysis in non-saturation and saturation cases.

3.2 Modeling the effects

Let us consider an N winding magnetic component where all the windings are wound around a common core in the axial section of this component. Figure 32 shows an example with three windings to be easier to explain the model. The classical coupled inductor theory says that the average flux per turn of winding, $\emptyset_k(t)$, is given by:

$$\emptyset_k(t) = \emptyset_c(t) + \sum_{i=1}^{N} \emptyset_{ki}(t) \tag{16}$$

where $\emptyset_c(t)$ is the core flux (it is shared by all the windings) and $\emptyset_{km}(t)$ is the flux induced in winding k by winding m circulating across the air, not through the core, the possibility being that k equals m (self-induced flux). The voltage of winding k may be determined using (17) as shown is Figure 32. If equation (16) is used in (17) and the relationship (18) is considered, the voltage of winding k is given by (19), and there are k equations like this, one per winding in the magnetic component [9].

$$u_k(t) = N_k \cdot \frac{d\emptyset_k(t)}{dt} \tag{17}$$

$$N_k \emptyset_{ki}(t) = L_{ki} \cdot i_i(t), \qquad k, i = 1, 2, \ldots, N, \qquad k \neq i \tag{18}$$

$$u_k(t) = N_k \cdot \frac{d\emptyset_c(t)}{dt} + \sum_{i=1}^{N} L_{ki} \frac{di_i(t)}{dt} \tag{19}$$
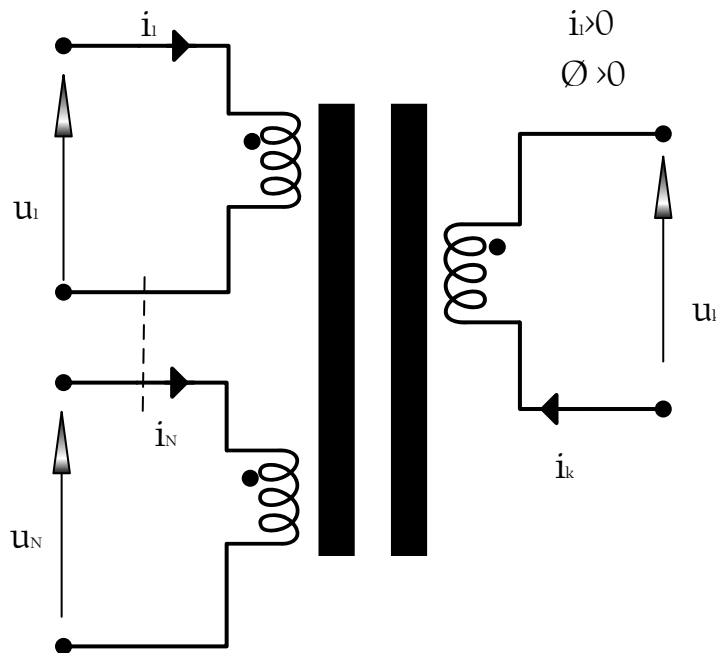
Figure 32. Magnetic Component and references.
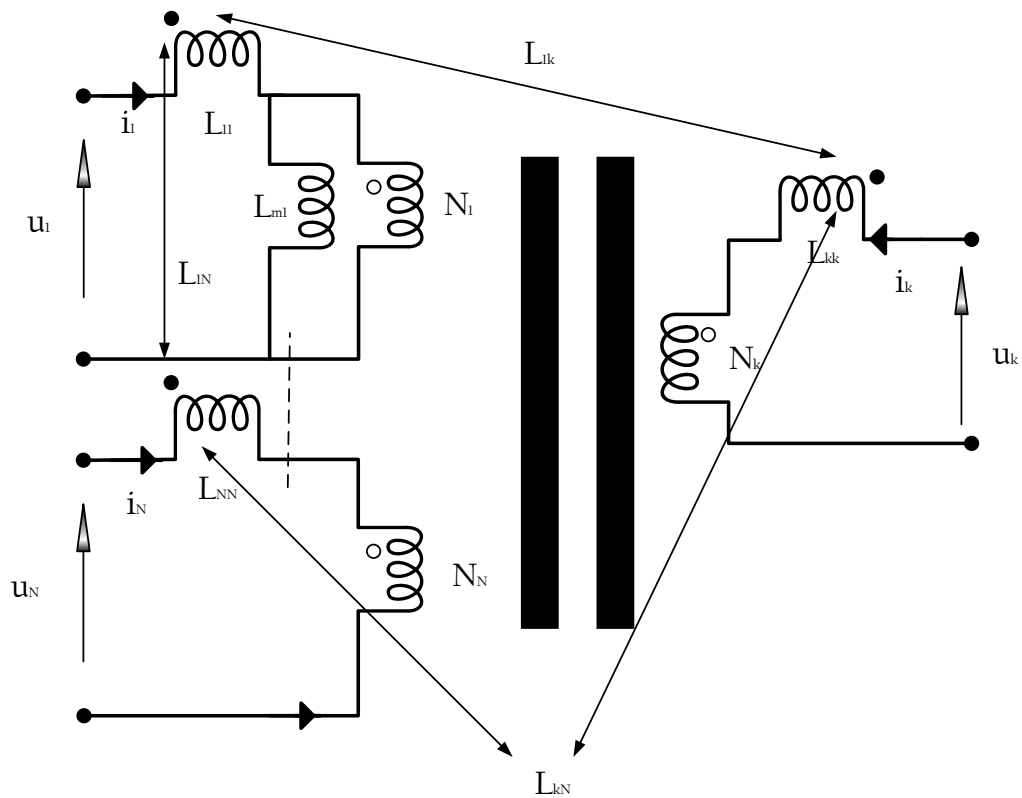
Figure 33. Magnetic Effects Model.

In this situation, the voltage is created by the mutual flux circulating by the core and *N* voltages created by the currents of the *N* windings that can be represented by means of a set of coupled inductors, one per winding of the magnetic component. The circuit in Figure 33 represents these equations.

The model which is presented in this chapter is a modification from the classical one where the inductance L_{ml} accounts for the mutual flux across the gap and the core, but not the mutual flux circulating through the air. It is very important to mention that self-inductances L_{kk} and mutual inductances L_{km} account for the effects of the leakage flux as well as the mutual flux circulating through the air [9].

An atypical assumption that simplifies the implantation of the magnetic component model in electrical simulators is to use only a kind of dotted terminal:

- Black dots represent the terminals of the windings.
- White dots represent the terminals for the ideal transformer.

3.2.1 *Inductance parameter extraction*

This model is based in the fundamental concept that a classical flux-based analysis is not adequate to determine the electrical parameters. Firstly, it is not clear what is the method to calculate the self and mutual fluxes in a turn built with a conductor in which the diameter is not null like any real situation. Secondly, as windings may have a very complex geometry, the calculations of fluxes are not an easy task. The procedure for model parameters is derived from handling energies because it is easier than handling fluxes. However, commercial FEMs are used to calculated fields. The parameter extraction method proposed in this section is based on energies calculated from the fields resulting by FEA.

As fields weaken outside the magnetic component, the zero vector potential boundary condition is imposed in a prism that encloses the component and a region of space surrounding the magnetic component, whose size depends on the component size (between 5 and 10 times the component length).

If current $i_k(t) = I_o sin(\omega t)$ is flowing in winding k, and the rest of the windings have no net current, a magnetic field $\overrightarrow{\boldsymbol{H}}_k(x,y,z,t) = H_x(x,y,z) \cdot sin(\omega t + \emptyset_x(x,y,z)) \cdot \vec{\imath} + H_y(x,y,z) \cdot sin(\omega t + \emptyset_y(x,y,z)) \cdot \vec{\jmath} + H_z(x,y,z) \cdot sin(\omega t + \emptyset_z(x,y,z)) \cdot \vec{k}$ appears in every point of the magnetic component. It is a vector whose components in X, Y, Z axes are sinusoids of pulsating angular frequency ω. In other words, it is a vector depending on the time and the coordinates, x, y, z

The magnetic component is working in the sinusoidal regime, and then phasors can be defined for the electromagnetic magnitudes: $\vec{\boldsymbol{I}}_{ko}, \vec{\boldsymbol{B}}_{ko}$ and $\vec{\boldsymbol{H}}_{ko}$. The total magnetic induction (20) and magnetic field (21) in any point of the component applying superposition are determined by:

$$\vec{\boldsymbol{B}}_o = \sum_{k=1}^{N} \vec{\boldsymbol{B}}_{k0} \tag{20}$$

$$\vec{\boldsymbol{H}}_o = \sum_{k=1}^{N} \vec{\boldsymbol{H}}_{k0} \tag{21}$$

$\vec{\boldsymbol{B}}_{ko}$ and $\vec{\boldsymbol{H}}_{ko}$ are the contributors of the winding k, $\vec{\boldsymbol{B}}_o$ and $\vec{\boldsymbol{H}}_o$ are the resulting vectors. Peak values have been used to define the phasors. Thus, the average energy stored in the component (except the core and the core gap) and all space around it may be determined by [9]:

$$W = \frac{1}{4} \oiiint_{v_t} Re(\vec{\boldsymbol{B}}_0 \cdot \vec{\boldsymbol{H}}_0^*) dv \; (J) \tag{22}$$

where "*" the conjugate vector and v_t the volume of the magnetic component without the core. If equations (20) and (21) are introduced in (22), the average energy stored in the entire component (except the core and the core gap) and all space around it is obtained in (23).

$$W = \frac{1}{4}\sum_{i=1}^{N} \oiint_{v_t} Re(\vec{B}_{i0} \cdot \vec{H}_{i0}^*)dv + \frac{1}{2}\sum_{i=1}^{N-1}\sum_{j=i+1}^{N} \oiint_{v_t} Re(\vec{B}_{i0} \cdot \vec{H}_{j0}^*)dv \ (J) \tag{23}$$

where "Re" means the real part of the vector.

This formula is composed of two kinds of terms. One term depends only on the fields created by the current of one winding i. The second one depends on the fields produced by two different windings $(i$ and $j)$.

The next equation represents the average energy that is stored in the equivalent circuit represented in $Figure\ 36$ (core energy is not included).

$$W = \frac{1}{4}\sum_{i=1}^{N} L_{ii}I_0^2 + \frac{1}{2}\sum_{i=1}^{N-1}\sum_{j=i+1}^{N} L_{ij}I_0^2 \ (J) \tag{24}$$

This equation has two different terms. One depends on the presence of a single current in the magnetic component (winding i) and the other one depends on the simultaneous presence of two currents (windings $i\ and\ j$). In order to obtain an equivalent circuit of the magnetic component, the equivalent terms of both expressions of the average energy must be equal according to [9]. Thus, L_{ii} and L_{ij} should be defined as:

$$L_{ij} = \frac{1}{I_0^2} \oiint_{v} Re(\vec{B}_{i0} \cdot \vec{H}_{j0}^*)dv \tag{25}$$

If a current $i_k(t)$ is injected in winding k, the core inductance referring to winding k, named L_{mk}, can be defined:

$$L_{mk} = \frac{1}{I_0^2} \oiint_{v_c+v_g} Re(\vec{B}_{k0} \cdot \vec{H}_{k0}^*)dv \tag{26}$$

The integration volume (v_c+v_g) is the volume occupied by the magnetic core (v_c) and the core gap (v_g). In the case of gap into the model, it can be necessary to divide the inductance L_{mk} into two inductances, one for the core and another for the gap. In order to split the inductance, the energies stored in the core and the gaps are used.

(a)   *(b)*
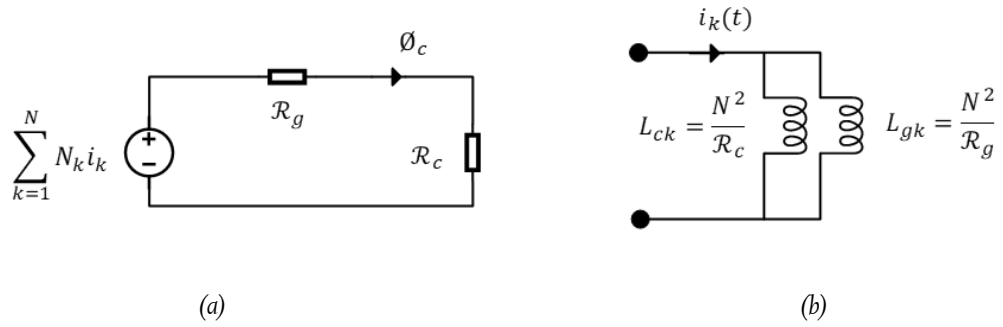
Figure 34. Analogy between the flux path by the core and gap and electrical circuit (a) Magnetic circuit (b) Electrical circuit.

(a)   *(b)*

Figure 35.Air gap (a) EE core (b) Toroidal core.

If the duality theorem between electricity and magnetism is applied, the circuit of Figure 34 represents the core and gap effects in the circuit referring to winding k. Inductance L_{mk} is replaced with L_{ck} and L_{gk}.

If a current $i_k(t) = I_o sin(\omega t)$ is injected in winding k, it results in the core and gap stored energies (W_c and W_g). Then, the core energy, W_c, is calculated as indicated in (27), the integral being calculated in the core (volume v_c). The gap energy, W_g, is calculated in the gap volume v_g using (28).

$$W_c = \frac{1}{4} \oiiint_{v_c} Re(\vec{B}_{k0} \cdot \vec{H}_{k0}^*)dv \tag{27}$$

$$W_g = \frac{1}{4} \oiiint_{v_g} Re(\vec{B}_{k0} \cdot \vec{H}_{k0}^*)dv \tag{28}$$

The gap in the last equation is a prism which represents the perfect gap which is the portion of air between both core halves (Figure 35). The fringing field of the gap (spread field outside of the gap) has an important impact in long gaps. Thus, it is included in this assessment in (27) -(28). W_T is the total energy stored in the core and the gap and it is calculated as:

$$W_T = W_c + W_g \tag{29}$$

Based on [9], the expressions of the core and gap inductances can be obtained as:

$$L_{ck} = \frac{4}{I_0^2} \frac{W_T^2}{W_c} \qquad (30)$$

$$L_{gk} = \frac{4}{I_0^2} \frac{W_T^2}{W_g} \qquad (31)$$

The previous calculations allow deriving a traditional gapped component model. One inductance representing the core effect and another representing the gap effect appear in the equivalent circuit, and their values can be calculated by equation (30) and (31). If the gap is not presented, then equation (29) can be used to calculate L_{mk}, W_T being equal to W_c. W_g is zero and the result (32) gives the confirmation that this procedure is valid for transformers as well following [19].

$$L_{gk} = \frac{4}{I_0^2} \cdot W_c \qquad (32)$$

3.2.2 *Resistance parameter extraction*

The procedure used to obtain the model structure for resistances (Figure 36) is similar to the previous one used for inductances. The expression of the losses as a function of the current density in the windings is derived, and, in addition, a circuit is synthesised from them.

If a current i_k is injected in winding k, and the other windings have zero net current, a current density distribution i_j appears in every point of the component. Windings k has current density affected by skin effect and winding $j{\neq}k$ has current density caused by proximity effect. When all windings have net current, the current density in a point, can be determined by:

$$\vec{J}_o = \sum_{k=1}^{N} \vec{J}_{k0} \qquad (33)$$

 It is the sum of the current density induced by each of the N windings of the magnetic component. Equation (34) represents the average power losses in the windings. The integral is calculated in the volume of the conductors. Using equations (33) and (34), produces (35).

$$P = \frac{1}{2} \oiiint_{v_w} Re(\vec{J}_0 \cdot \vec{E}_0^*)dv = \frac{1}{2} \oiiint_{v_w} Re\left(\frac{(\vec{J}_0 \cdot \vec{J}_0^*)}{\sigma}\right) dv \text{ (W)} \qquad (34)$$

$$P = \frac{1}{2}\sum_{i=1}^{N} \oiiint_{v_w} Re\left(\frac{\vec{J}_{i0} \cdot \vec{J}_{i0}^*}{\sigma}\right) dv + \sum_{i=1}^{N-1}\sum_{j=i+1}^{N} \oiiint_{v_w} Re\left(\frac{\vec{J}_{i0} \cdot \vec{J}_{j0}^*}{\sigma}\right) dv \text{ (W)} \qquad (35)$$

where v_w the volume of the windings. There are two terms in the expression. The first term depends on the existence of current in a unique winding i. The second one depends on the
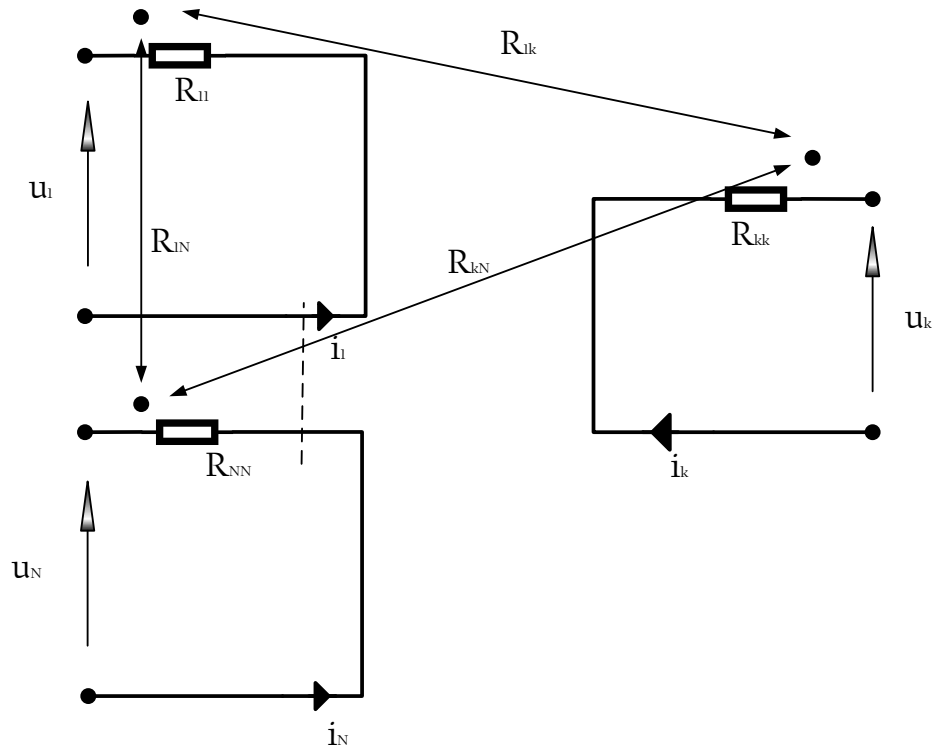
Figure 36. Resistive effects model in windings.

existence of current different windings (i and j). The equivalent circuit represents this assumption. The power losses of this set of coupled resistances depend on individual currents acting independently and simultaneously.

The average losses are calculated by means of:

$$P = \frac{1}{2}\sum_{i=1}^{N} R_{ii}I_0^2 + \sum_{i=1}^{N-1}\sum_{j=i+1}^{N} R_{ij}I_0^2 \ (W)$$

(36)

From (34), (35) and (36) it can be obtained that:

$$R_{ij} = \frac{1}{I_0^2}\oiiint_{v_w} Re\left(\frac{\vec{J}_{i0}\cdot\vec{J}_{j0}^*}{\sigma}\right)dv$$

(37)

3.2.3 Complete model structure

Once the equivalent circuits for energy storage and power losses have been obtained from [9], they are merged into a single equivalent circuit that represents both effects (Figure 37) The expressions of the operational impedances $\mathcal{Z}ii(s)$ and $\mathcal{Z}ij(s)$ are:

$$\mathcal{Z}ii\,(s){=}Rii\,(s){+}Lii\,(s)$$

(38)

$$\mathcal{Z}ij\,(s){=}Rij\,(s){+}Lij\,(s)$$

(39)
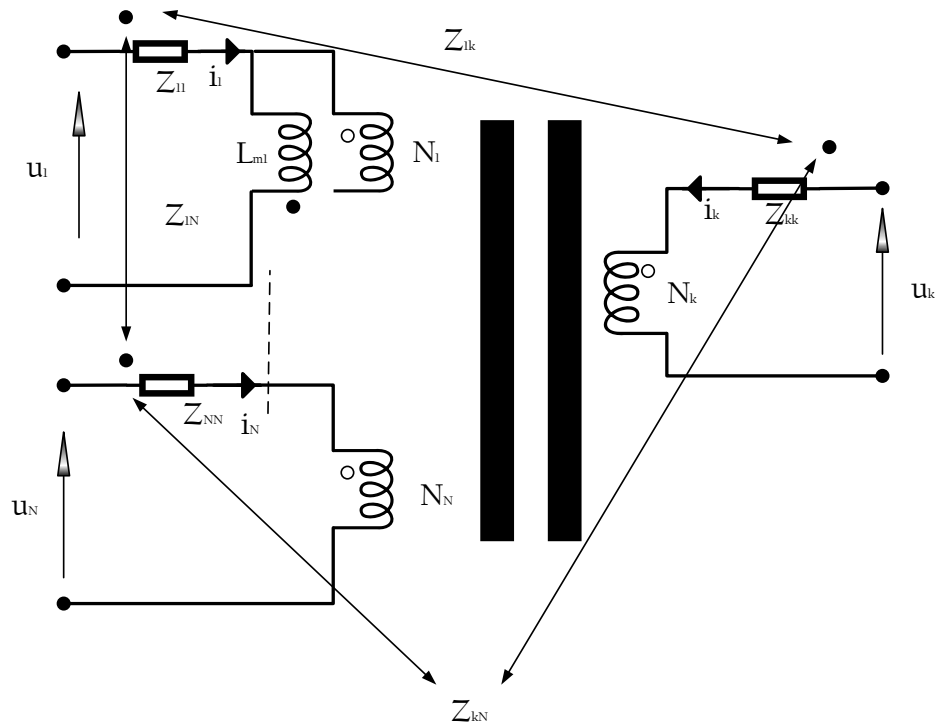
Figure 37. Multiwinding magnetic component model.

According to [9]:

- $Z_{ii}(s)$ represents the magnetic energy and power losses when the net current is only flowing though winding. Therefore, this impedance takes into consideration: the energy (except the core and gap) when current is flowing through winding, the losses in winding (skin effect), and the power losses induced in windings (proximity effect).

- $Z_{ij}(s)$ represents the contribution to the magnetic energy and the power losses caused by the simultaneous conduction of net current through windings.

The energy and the losses in the windings when the current is flowing simultaneously through two windings are not the addition of those calculated when current is flowing though each winding independently. These losses could be higher due to the addition of ampere turns in a particular winding zone or lower because of the compensation of ampere turns (i.e.: interleaving).

This model is a very important contribution of this work. Because the impedances are shared by all the windings, this idea was used in the past by [44], but not for any magnetic component topology and operation frequency, for which it is adequate because the contribution from every winding on power losses depends on each current.

3.3 Proposed parameter extraction procedure

As it was explained previously, not every component can be modelled in the 3D FE tool. In [73] and [74] , the relationship between the computer features and number of elements used in a FEA was obtained. According to [74,75], the main factor to determine this value in a 3D simulation is the conductor cross-section for the windings.

This parameter extraction procedure is based on 3D FEA divided in three steps:

1. Modeling.

2. Component simulation.

3. Result-processing.

At the modeling phase, the component is designed in three dimensions and the conductor cross-sections are modified from circular to polygonal to reduce the FE number to achieve the convergence in the FE tool as well as reducing the CPU time. This modification involves that the conductor surface and the distance between conductors are not exactly the same in that the real component producing different values in the winding resistance and inductance.

One contribution of this thesis is the adjustment of the material properties for the conductors, following (40 and 41) to have the same resistance and inductance values in DC.

$$\sigma_{Pol} = \frac{S_{Circular}}{S_{Polygon}} \cdot \sigma_{Circular} \tag{40}$$

$$\mu_{Pol} = \frac{S_{Circular}}{S_{Polygon}} \cdot \mu_{Circular} \tag{41}$$

where $S_{circular}$ is the circular cross-section and the $S_{polygon}$ is the area of the polygonal cross section. The component using the polygonal model applying the material properties from (40) and (41) in the modeling phase will be name the polygonal model. As this model has much smaller FE number than the original one, the simulation can be completed and the CPU time reduces drastically.

After the simulation, in the result-processing stage, the parameter extraction is according to the magnetic-electrical equivalent circuit shown in Figure 33 and Figure36 [9]. The resistance and inductance for the windings are calculated by script using:

$$L_{ij} = \frac{1}{I_o^2} \oiiint_{v_w} \frac{1}{\mu} \cdot Re(\vec{B}_{io} \cdot \vec{B}_{jo}^*) \, dv \tag{42}$$

$$R_{ij} = \frac{1}{I_o^2} \oiiint_{v_w} \frac{1}{\sigma} \cdot Re(\vec{J}_{io} \cdot \vec{J}_{jo}^*) \, dv \tag{43}$$

This methodology is focused on inductive components used in power electronics converters where some frequency effects are very relevant for the winding modeling like skin and proximity effect.

These frequency effects have different behaviour for circular and polygonal cross-section. Therefore, a correction factor is needed to obtain the same value for the winding resistance using both cross-sections and its corresponding material properties.

The impact of the frequency in inductances in this procedure using polygonal instead of circular sections for this methodology is negligible as demonstrated in [79-82].

3.3.1 *Correction factor for resistance depending on the frequency*

As demonstrated in the Chapter 2, the polygonal model is not enough to determine the electrical parameters in AC, and it is only valid for DC, it is necessary to calculate a correction factor depending on the frequency which is applied on the extracted resistance from the polygonal model to achieve accurate results for the resistance.

$$R_{ij}^{real} = k \cdot R_{ij}^{FEM} \tag{44}$$

The correction factor is divided in two coefficients corresponding to the skin and proximity effects that depend on the frequency.

$$k = k_{skin} + k_{proximity} \tag{45}$$

A dedicated analysis sequence has been performed to calculate this correction factor. This study consists of the comparison between the resistance from the real component and the resistance from the polygonal model. The comparison between both resistances is named EQ_R and defined in (46).

$$EQ_R = \frac{R_{cirle}}{R_{polygon}} \tag{46}$$

The correction factor also depends on the polygonal cross-section used in the simulation. A new term is introduced in the study to involve the polygonal section dependency named A_{pol}, described in (47) and presented in Table 13 and

Table 14 for the polygonal sections used and the corresponding conductivity.

$$A_{pol} = \frac{S_{circle}}{S_{polygon}} \tag{47}$$

As the conductivity has been modified using (40), the skin depth is also modified according to the used cross section (Table 15).

Table 13. Conductor cross-sections
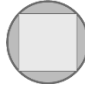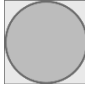
	Circular	Diamond	Square into Circle	Square outside Circle	Hexagon
A_{pol}	1	1.5708	1.5708	0.7854	1.2092
Conductivity (σ_{pol}) (S/m) from (26)	58000000	91106186	91106186	45553093	70133575

Table 14. Data for the starting point

	(R$_1$)	(R$_2$)
Material	Copper	Copper
American Wire Gauge	AWG18	AWG24
Conductor radius (mm)	1.02	0.510
Turns	1	1

Table 15. Skin depths (m) for different conductor cross-sections

Cross-section shape equivalent conductance	variable)	frequency f (KHz)			
		0.001	48.39	537.67	1,209
Circular $\sigma(Cu)= 58000000\ S{\cdot}m$	δ	6.64E-02	3.02E-04	9.06E-05	6.04E-05
Hexagonal $\sigma_1(Cu)= 70133575\ S{\cdot}m$	δ_1	6.04E-02	2.75E-04	8.24E-05	5.49E-05
Octagonal $\sigma_2(Cu)= 64421802\ S{\cdot}m$	δ_2	6.30E-02	2.86E-04	8.59E-05	5.73E-05
Dodecagonal $\sigma_3(Cu)= 60737457\ S{\cdot}m$	δ_3	6.49E-02	2.95E-04	8.85E-05	5.90E-05
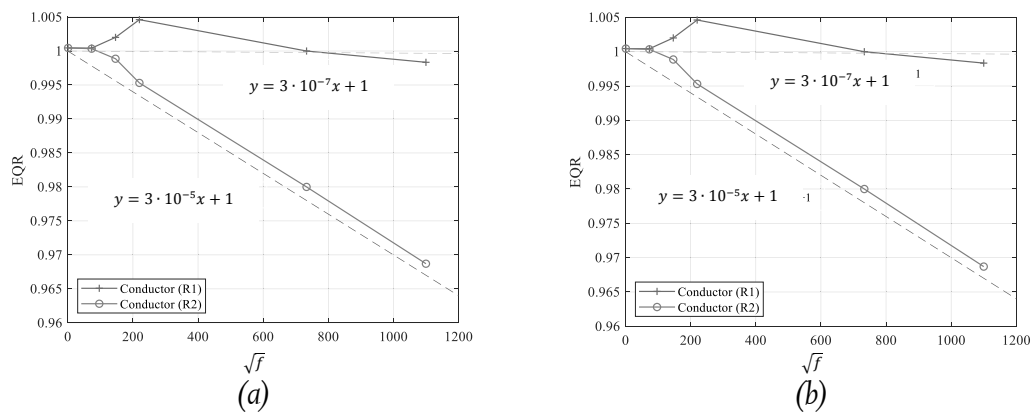
Figure 38. EQ$_R$ for a single wire alone and single circular coil with hexagonal cross-section (a) R$_1$(AWG18) and R$_2$ (AWG24). Single wire alone; (b) R$_1$(AWG18) and R$_2$ (AWG24). Single circular coil.
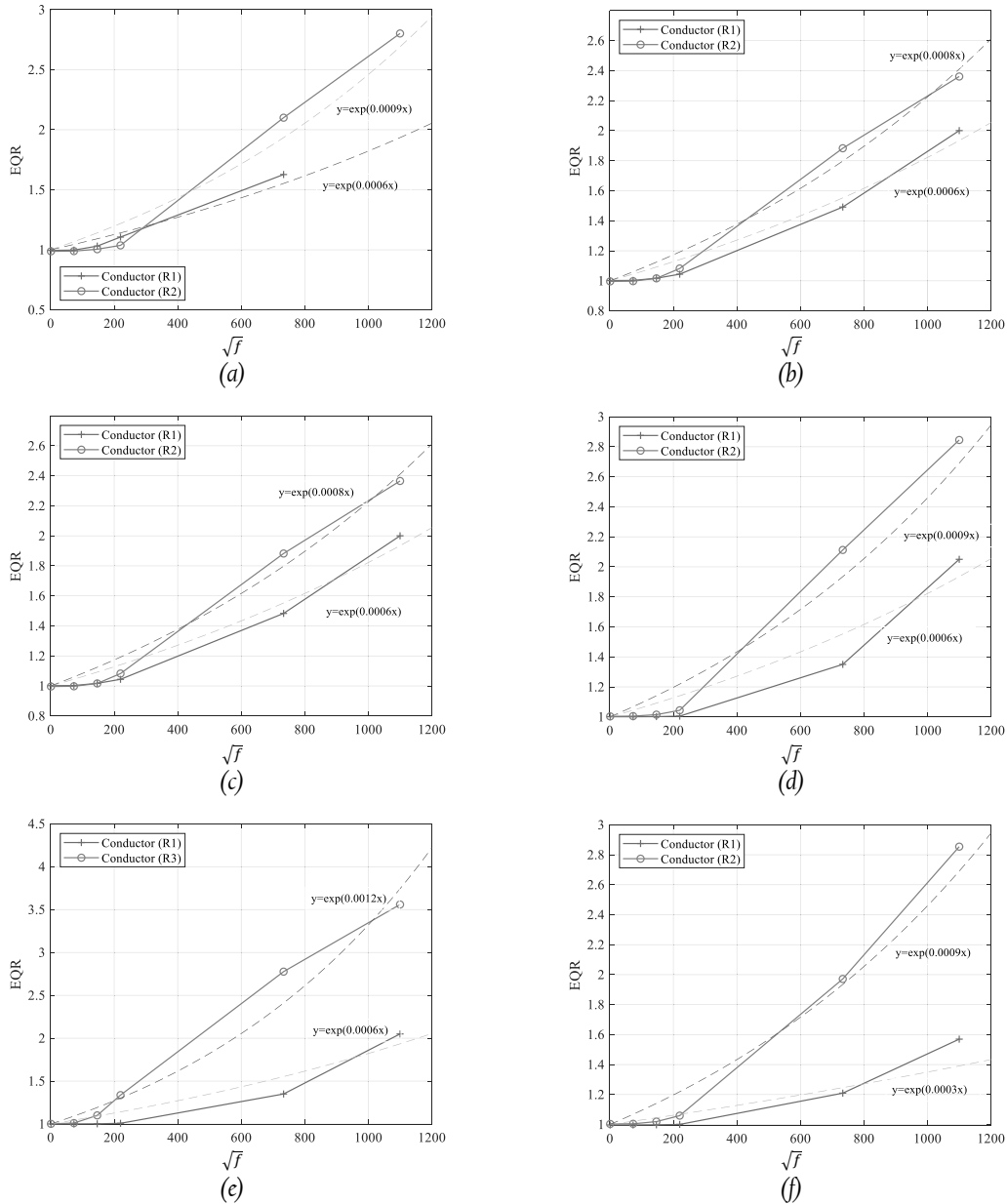
Figure 39. EQ_R for different cases of single square coil with hexagonal cross-section (a) Ferrite core (3C90); (b) Air core; (c) 4A driven in both conductors; (d) Square edge 20 mm; (e) R_1=AWG18 and R_3=AWG12 (f) Square edge 5 mm.

Firstly, three simple cases have been evaluated to understand the skin effect for different polygonal cross-sections. These cases are a single wire alone, a single circular coil and a single square coil for different cross-sections. Also, the cases have been developed for two different conductors ($R_1 \rightarrow$ AWG18 and $R_2 \rightarrow$ AWG24).

Figure 38 and Figure 39 show the evolution of EQ_R versus frequency for different cases as examples. The single wire alone is only impacted for the skin effect. The proximity effect is only defined strictly for more than one conductor; so, there is loop current effect in circular and square coils.

Figure 38 (a) shows the EQ_R for a single wire alone, which depends on the current and conductor diameter. The EQ_R for a circular coil is plotted in Figure 38 (b), where there is an additional parameter to be included, the coil diameter. The case for square coils has more impact from the current loop effect. Some examples are shown in Figure 39 where the EQ_R tendency is in agreement with the theoretical assessment from [83].

3.3.1.1 Skin effect study

In this section, a theoretical assessment will be developed, supported by FEA results for three different cases: a single wire alone, a circular coil and a square coil to determine the skin effect by itself in the effective resistance.

1)   <u>Single wire alone</u>

The effective resistance for a wire (circular cross section) in DC is given by

$$R = \rho \frac{l}{S} \tag{48}$$

However, in AC the resistance increases because the current density becomes distributed within a conductor, being largest near the surface of the conductor, and decreasing with greater depths in the conductor.

The skin depth, δ, determines the net surface used by the current depending on the frequency

$$\delta = \sqrt{\frac{2}{\omega\mu\sigma}} \tag{49}$$

and the real surface used by the current in this situation defined in (50) being the surface of the circular crown with thickness δ. Therefore, the effective resistance in AC for a single wire alone, using the last equations, is given by (51).

$$S_{effective} = \pi \cdot r_1^2 - \pi \cdot (r_1 - \delta)^2 = 2\pi r_1^2 \delta - \pi \delta^2 \tag{50}$$

$$R_{effective} = \rho \frac{l}{S} = \rho \frac{l}{2\pi r_1 \delta - \pi \delta^2} \tag{51}$$

where ω is the angular frequency of the sinusoidal current of the conductor, μ is the conductor material permeability, σ is the wiring material conductivity, and r_1 is the radius of the surface used by the current according to the frequency f.

As the material properties are modified when polygonal sections are used in the FE tool, the skin depth, δ_i, has different values per each polygonal section due to the conductivity used having been adjusted according to Table 15. It approaches as a mathematical estimation that the real surface is decreasing in a circular shape whatever cross-section is used in the
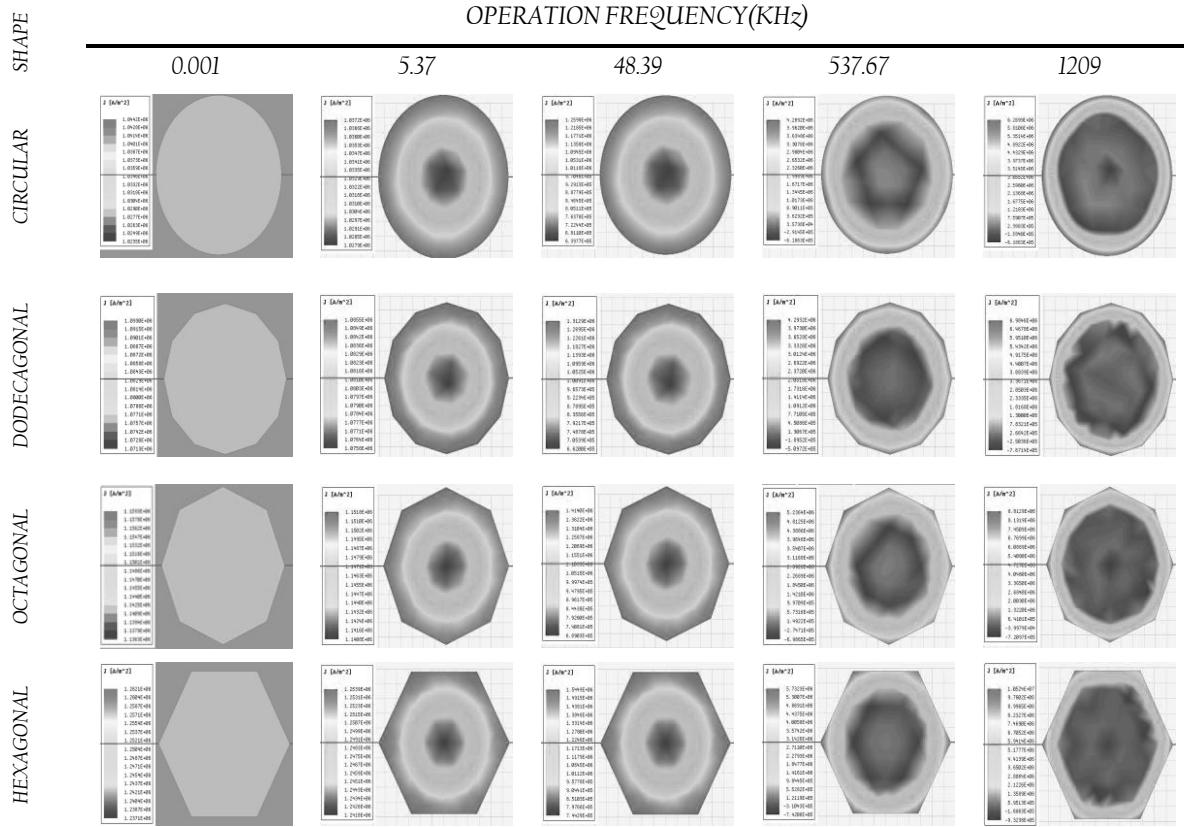
Figure 40. Current density obtained from FEA for a single wire alone for different cross-section shapes.

simulation removing the computational effect for the meshing, mainly in high frequencies according to the analysis sequences developed (Figure 40).

Table 15 also shows the frequencies used in the analysis sequence, where these operation frequencies are in the range corresponding to the switching frequencies normally used for operating power converters based on Si, SiC or GaN semiconductors. The conductors have been selected so that skin depth ranges from one conductor to another are multiples. The net surfaces used by the current in the polygonal models depend on the cross-section and they are:

- Hexagonal section:

$$S = \frac{3}{2}\sqrt{3}r_1^2 - \pi r_2^2 = \frac{3}{2}\sqrt{3}r_1^2 - \pi(r_1 - \delta_1)^2 = 2\pi r_1\delta_1 - \pi\delta_1^2 - 0.54r_1^2 \qquad (52)$$

- Octagonal section:

$$S = 2\sqrt{2}r_1^2 - \pi r_2^2 = 2\sqrt{2}r_1^2 - \pi(r_1 - \delta_2)^2 = 2\pi r_1\delta_2 - \pi\delta_2^2 - 0.31r_1^2 \qquad (53)$$

- Dodecagonal section:

$$S = 3r_1^2 - \pi r_2^2 = 3r_1^2 - \pi(r_1 - \delta_3)^2 = 2\pi r_1\delta_3 - \pi\delta_3^2 - 0.14r_1^2 \qquad (54)$$

Table 16. Effective Conduction Area for polygonal cross-sections related to the circular ones

Polygon	A_{pol}	Simplified A_{pol}
Hexagon	$\dfrac{2\pi r_1 \delta - \pi \delta^2}{2\pi r_1 \delta_1 - \pi \delta_1^2 - 0.54 r_1^2}$	$\sim \dfrac{2\pi r_1 \delta}{2\pi r_1 \delta_1 - 0.54 r_1^2}$
Octagon	$\dfrac{2\pi r_1 \delta - \pi \delta^2}{2\pi r_1 \delta_2 - \pi \delta_2^2 - 0.31 r_1^2}$	$\sim \dfrac{2\pi r_1 \delta}{2\pi r_1 \delta_2 - 0.31 r_1^2}$
Dodecagon	$\dfrac{2\pi r_1 \delta - \pi \delta^2}{2\pi r_1 \delta_3 - \pi \delta_3^2 - 0.14 r_1^2}$	$\sim \dfrac{2\pi r_1 \delta}{2\pi r_1 \delta_3 - 0.14 r_1^2}$

(a)   *(b)*
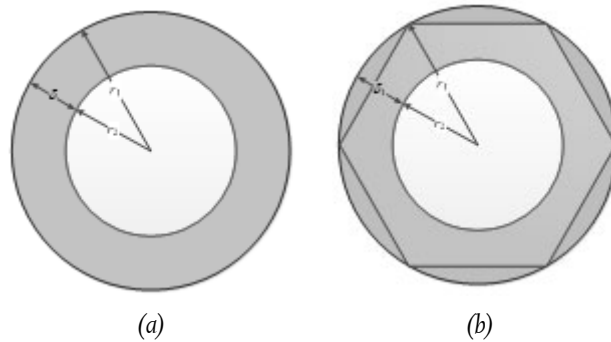
Figure 41 (a)Circular cross -sections (b)Polygonal cross-section (hexagon example) and the effective conduction area (filled in orange).

Table 16 summarises the A_{pol} (47) in AC for the different polygonal sections used in the study and the potential simplification for the mathematical expressions due to the terms of the second order.

Using the values of Table 16 to calculate EQ_R and introducing δ_i (skin factor for polygonal sections), the equation (55) is obtained.

$$EQ_R = \frac{R_{Circular}}{R_{polygon}} = \frac{\dfrac{\sigma l}{S_{Circular}}}{\dfrac{\sigma l}{S_{polygonal}}} = \frac{S_{polygonal}}{S_{Circular}} = \frac{2\pi r \delta_i - \pi \delta_i^2}{2\pi r \delta - \pi \delta^2} \qquad (55)$$

In addition, Figure 40 show the FEM results of the current density for different cross-sections at the selected frequencies demonstrating the decrease of the net surface in circular shape used by the current. Figure 41 represents the skin depth for the polygonal sections (a hexagonal section as an example) according to the FEM results.

Analysing this effect in detail, Figure 42 shows the mathematical approach for an hexagonal section where r_A is the circular border for the net surface used if a circular cross-section is considered and r_B corresponds to the polygonal cross-section.

Figure 43 and Figure 44 show the FEM results for high and low frequencies and the different cross-sections, showing the impact on the skin depth $\delta_{i,}$. Even the material properties have been modified according to the cross–section to have the same DC resistance (Table 16).
If Ampère's law is applied in the circular and the polygonal cross sections, equations (56) and (57) are obtained B_A and B_B being the peak values of the magnetic field density.

$$B_A = \frac{\mu I}{2\pi r_1^2} \cdot r_A \tag{56}$$

$$B_B = \frac{\mu I}{2\pi r_1^2} \cdot r_B \tag{57}$$

These values of the magnetic field density can be normalised as $B_{polygonal}/B_{circular}$ and these are compared with the obtained values for A_{pol}, (Table 17), confirming that equation (57) is valid. In other words, the ration between B_B and B_A gives exactly the value of $A_{pol.}$

$$B_B = \frac{\mu I}{2\pi r_1^2} \cdot r_B = \frac{\mu I}{2\pi r_1^2} \cdot A_{pol} \cdot r_A = A_{pol} \cdot B_A \tag{58}$$

Hence, the skin factor of the polygonal model can be assumed as:

$$\delta > \delta_i \sim \frac{\delta}{A_{pol\,(DC)}} \tag{59}$$
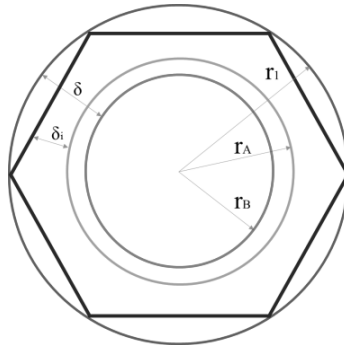
Figure 42. Skin depth in polygonal section.
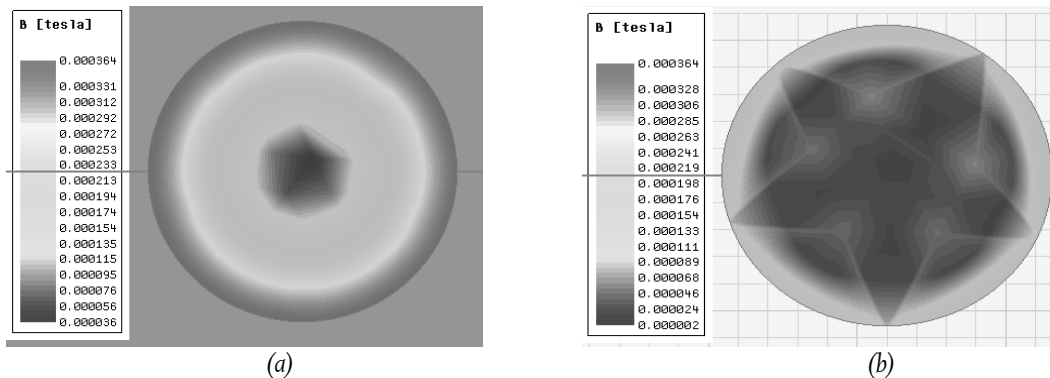
Figure 43. Magnetic Field Density AWG18 in circular section (a)0.001kHz (b) 1209 kHz.
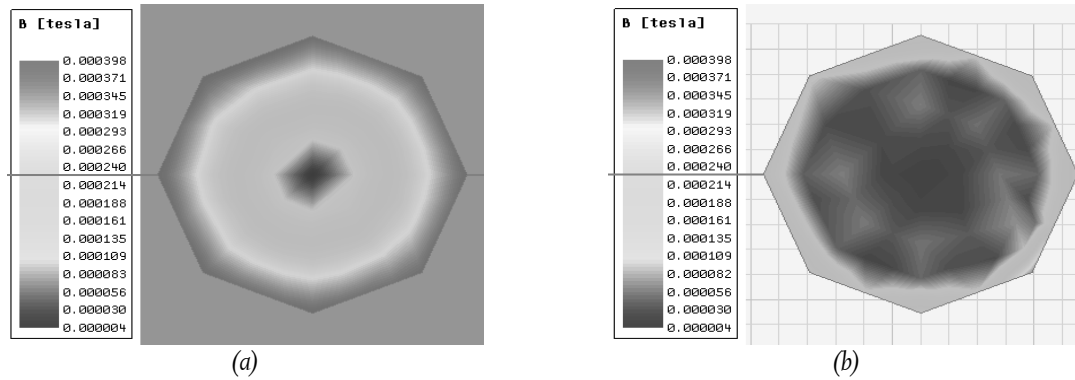
Figure 44. Magnetic Field Density AWG18 in hexagonal section (a)0.001kHz (b) 1209 kHz.

Table 17. Normalisation of the magnetic field density (B)

	Cross-Section	R_3=0.185 (AWG14)	$R1$=0.285 (AWG18)	R_2=0.55 (AWG24)	R_4=0.725 (AWG29)	Avg**	A_{pol} (0 Hz)
B_A	Circular	2.8 mT	3.6 mT	7.1 mT	1.4 mT		
B_B	Hexagonal	3.4 mT	4.3 mT	8.3 mT	1.7 mT		
B_B/B_A	*Normalisation**	1.2143	1.1944	1.1690	1.1972	**1.19**	**1.20**
B_B	Octagonal	3.1 mT	4.0 mT	7.8 mT	1.5 mT		
B_B/B_A	*Normalisation**	1.1071	1.1111	1.0986	1.0563	**1.09**	**1.11**
B_B	Dodecagonal	2.9 mT	3.8 mT	7.4 mT	1.49 mT		
B_B/B_A	*Normalisation**	1.0357	1.0556	1.0423	1.0423	**1.04**	**1.04**

*Normalisation= division between the B value in the polygonal section and the circular one (B_B/B_A).
**Avg=Normalisation average

2) <u>Single circular coil</u>

The resistance from one single wire alone (only skin effect) has been determined and normalised to one metre, named R_{wire} in this work. The difference between R_{coil} (resistances obtained for the singular circular coils normalised to one metre as well) and R_{wire} is the resistance due to the impact of the current loop effect exclusively named $R_{cl.}$ One example is shown in Figure 44.

$$R_{lc} = R_{coil} - R_{wire} \tag{60}$$

	OPERATION FREQUENCY (KHz)					
	0.001	5.37	21.5	48.39	537.67	1,209
B (T)						
J (A/m²)						
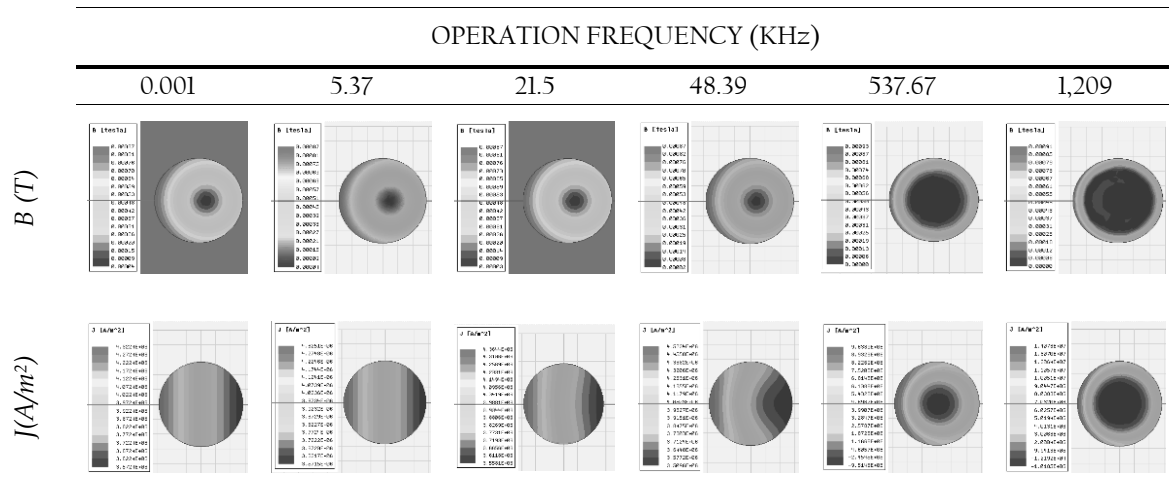
Figure 45. Magnetic field and current density in a single coil (AWG24) with r_m=3mm.

(a)   *(b)*
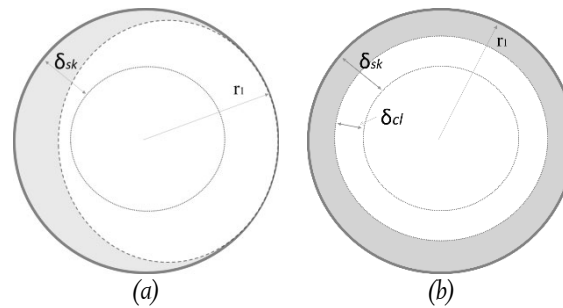
Figure 46. Net surfaces for skin and proximity effect (a)Real situation (b) Mathematical approach.

But the nature of this effect is different from the skin effect and there is not any circular effective area flowing by the current, in spite of the behaviour of this effect producing a not circular surface used by the current. As a mathematical approach, it could define the proximity depth, δ_{lc}, in order to calculate the equivalent surface of the conductor to obtain an equivalent R_l. (Figure 46).

Applying a similar strategy as in the previous section for the skin effect, the effective area in a single circular coil can be calculated by:

$$A = \pi \cdot r_1^2 - \pi(r_1 - \delta_{sk} + \delta_{cl})^2 \tag{61}$$

where A is the net surface used by the winding current and δ_{sk} is the skin depth for a single wire alone. Developing the mathematical expression, A can be obtained as:

$$A = 2\pi r_1(\delta_{sk} - \delta_{cl}) + 2\pi\delta_{sk}\delta_{lc} - \pi(\delta_{sk}^2 + \delta_{cl}^2) \tag{62}$$

Applying the general law of Ampère, that was used for a single wire alone in the previous section.

$$\oint B \, dl = \mu \iint J \, ds \tag{63}$$

and using the net surface produced by these effects in this mathematical approach, (64) is obtained where the second order terms can be removed to simplify the expression as in (65).

$$B = \frac{\mu I}{(2\pi r_1)^2(\delta_{sk} - \delta_{cl}) + (2\pi)^2 r_1 \delta_{sk}\delta_{cl} - 2\pi^2 r_1(\delta_{sk}^2 + \delta_{cl}^2)} \tag{64}$$

$$B \sim \frac{\mu I}{(2\pi r_1)^2(\delta_{sk} - \delta_{cl})} \tag{65}$$

For a particular operational frequency, the total depth produced by the skin effect and the current loop effect can be determined by (66). In addition, the FEM results confirm that the resistance from the current loop effect $R_{cl} = (R_{coil} - R_{wire})$ is very similar to the resistance calculated using the depth from the current loop effect (67).

$$\delta_{lc} = \delta_{sk} - \frac{B(2\pi r_1)^2}{\mu \cdot I} \tag{66}$$

$$R_{cl,circular} = F_{pol} \cdot R_{lc,poligonal} \tag{67}$$

The objective of this mathematical approach is to provide a quick method to calculate the corresponding skin and the current loop effects separately.

The comparison between the R_{cl} for circular and different polygonal sections has been performed and corresponding analyses for R_{cl} between the circular cross section and whatever polygonal sections have been developed as well.

The comparison analysis of the R_{cl} between the circular and polygonal sections has been performed, resulting a new coefficient, F_{pol}, that could be defined to obtain the resistance due to the current loop effect if the FEM uses a polygonal cross section.

The coefficient F_{pol} depends on the conductor diameter and it is close to one for most of the cases. Thus, the influence of the current loop effect using any polygonal section is similar using FEM analyses. Therefore, the current loop depth for a polygonal section can be calculated:

$$\delta_{cl_p} = \delta_{sk_p} - \frac{B(2\pi r_1)^2}{\mu \cdot I} \tag{68}$$

where r_1 is the radius of the original circular cross section that contains the polygonal cross section used in the problem, δ_{cpl} is the depth corresponding to the current loop effect using the polygonal cross section and δ_{skp} is the skin depth for the polygonal section.

3) <u>Single square coil</u>

This case has been analysed by permuting different parameters indicated in Table 18, determining the isolated influence of the skin and the current loop effects, obtaining a difference for the current loop effect producing a greater repercussion for the edge effect of the

square. The EQ_R obtained from a mathematical regression from the developed permutations (Table 18) is:

$$EQ_R = A_{pol} \cdot r_1^{1/2} \cdot f \qquad (69)$$

giving the next equation for the skin depth for a single square alone:

$$k_{skin} = e^{\left(\frac{EQ_R}{1000}\right)} \qquad (70)$$

where r_1 is the radius of the circular section that contains the polygon and f is the frequency.

Table 18 Parameters used in permutations for case III (*See. Figure 47*)

Nro	Parameter	Values
1	Conductor cross-section	Circular, Diamond, Square into Circle, Square outside Circle, Hexagon
2	Conductor dimension	AWG29, AWG24, AWG18, AWG14
3a	Edge length ED_1*	Standard, +5mm, +10mm, +15mm, +20mm,
3b	Edge length ED_2*	Standard, +5mm, +10mm, +15mm, +20mm,
4	Core Material	Vacuum, 3C90, 3C98,3F4,4F11

(a)   (b)   (c)
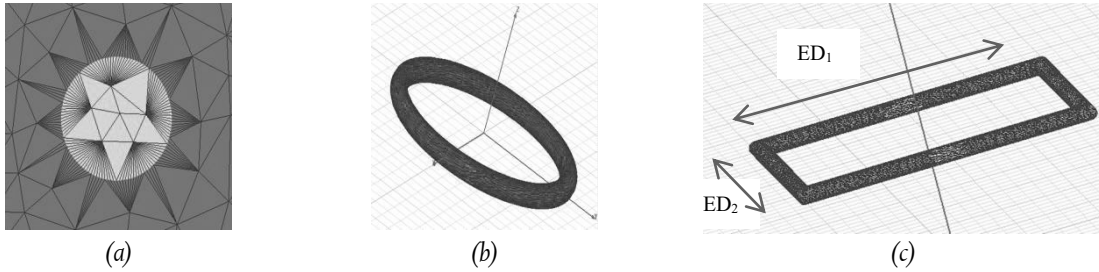
Figure 47. Description of the three analysed cases Notes: (a) A single wire alone (case I); (b) A single circular coil (case II); (c) A single square coil (case III)

3.3.1.2 Proximity effect study

There are two well-known methods for calculating high-frequency winding losses in round-wire windings. The methods from Ferreira [84] and Dowell [85] give significantly different results at high frequency and they have substantial errors, exceeding 60%. The Ferreira method, which is based on the exact Bessel-function solution for the eddy current in an isolated conducting cylinder subjected to a time varying magnetic field, is found to be most accurate for loosely packed-windings, whereas the Dowell method, which approximates winding layers comprising multiple turns of round wire with a rectangular conducting sheet, is most accurate for closely packed-windings.

The proximity effect will be analysed in detail for the square coils, the ones used in the EE and Toroidal cores which are the magnetic components for this research using polygonal cross-sections. Based on [84] the skin effect and proximity effect can be calculated separately due to the orthogonality existing between them.

A square shaped winding having different number of coil turns (1 turn to 14 turns), has been studied (Figure 47) permuting all the geometrical parameters used in the last case (Table 18).

Chapter 3. Proposed electrical equivalent circuit based on 3D FEM

By excluding the influence of the skin effect, calculated in the previous section, one may obtain for the proximity effect:

$$k_{prox} = e^{\left(\frac{A_{pol}}{1000}\cdot\frac{n}{k_C}\cdot r^{1/2}\right)\cdot f} \tag{71}$$

where k_C is a number of combinations without repetition $\binom{l}{2}$, where l represents the number of edges of the polygonal cross-section and n is the number of the turns in the winding. The factor k_C takes into account various cross-section area chosen for studied conductors in FEA using the real model or the polygonal model.

Table 19 shows the value of k_C depending on the polygonal shape used for the winding cross-sections in the polygonal model. The results for different calculated cases are graphically presented in Figure 48. The solid lines show calculated values using FEA and the dashed lines represent their regression. The regression has allowed determining kc which is the value that defines the area used for the conductors, A_t, if the windings are modelled with circular or polygonal cross-sections in the FEM (Figure 49).

Table 19. Definition of k_C depending on the edges in the polygon

l	4	6	8	10	12	18
k_C	6	15	28	45	66	153

(a)

(b)

(c)

(d)
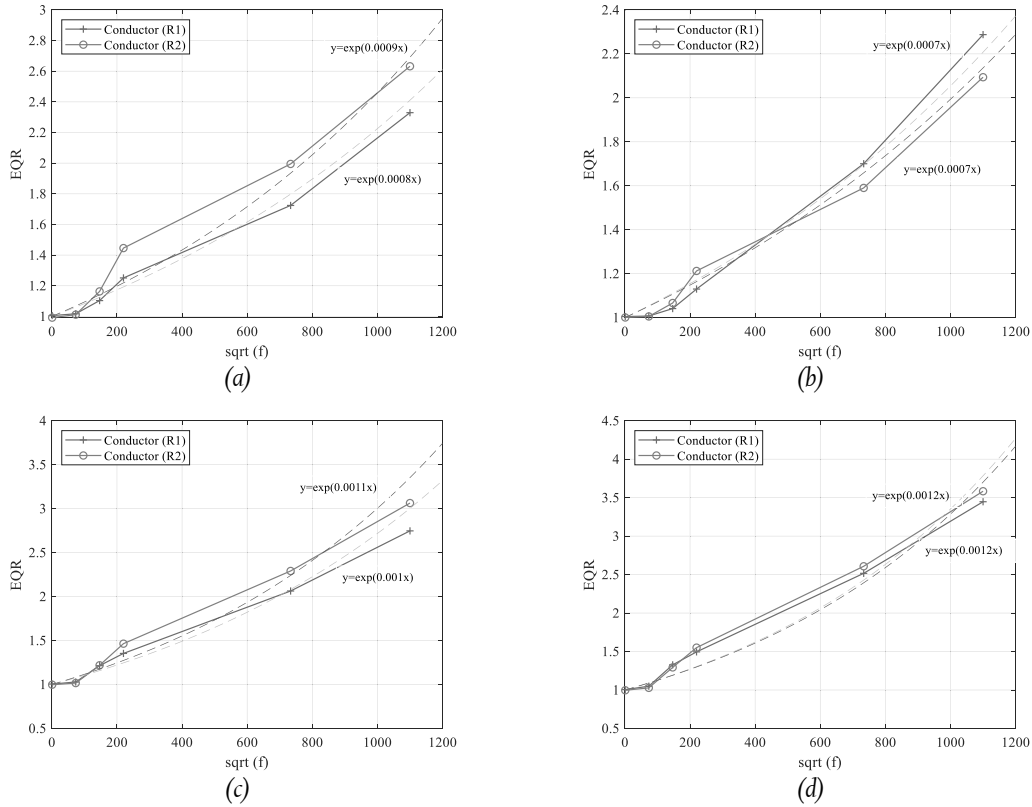
Figure 48. EQ$_R$ for different cases of single square coil with hexagonal cross-section (a) 2 conductors in primary (R1) and 2 conductors in secondary (R2); (b) 4 conductors in primary (R1) and 4 conductors in secondary (R2); (c) 8 conductors in primary (R1) and 8 conductors in secondary (R2); (d) 14 conductors in primary (R1) and 14 conductors in secondary (R2.)
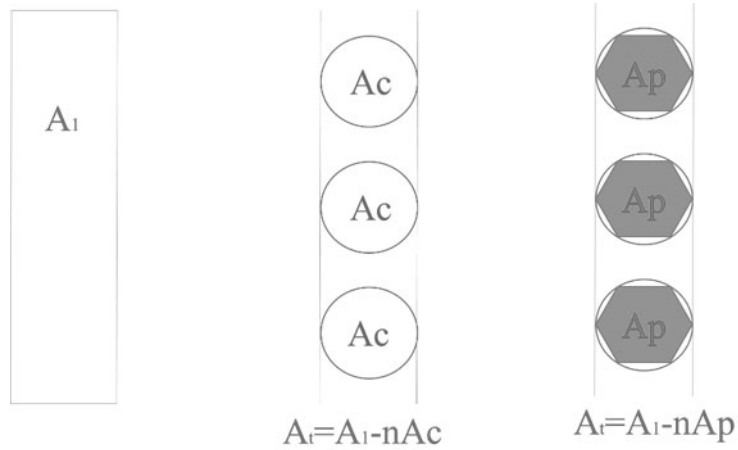
Figure 49. Different Areas. Proximity Effect.

3.4 Experimental validation of the parameter extraction from the 3D modeling procedure

The validation of the new methodology has been performed with experimental measurements for 4 different non-symmetric inductive components that will be described in this section. The impedance analyser (Keysight Technologies 4294A), showed in Figure 50, is the electronic device, and it has a four terminal-pair configuration for the measurements of impedance parameters over the temperature range of 0 to 40ºC with a basic impedance accuracy of +/-0.08% from 40Hz to 110 MHz.

This analyser used for the tests has an equivalent circuit whose corresponding equations are indicated in (72-75). Figure 51 shows the typical equivalent circuit from the analyser with the resistances of the short-circuits and non-load current.

$$Z_{cc1} = R_{cc1} + jX_{cc1} \tag{72}$$

$$Z_{01} = R_{01} + jX_{m1} \tag{73}$$

The equivalent circuit for the analyser is different from the equivalent circuit used in the parameter extraction procedure using FEA based on energies. Therefore, the simplest way to validate the results is to use (22) and (23) to transform the experimental measurements in comparable parameters with the parameters extracted from the FEM based method:

- Open Circuit Test:

$$Z_{o1} + Z_{cc1} \approx Z_{11} \tag{74}$$

- Short Circuit Test (example of 2 windings);

$$Z_{cc1} \approx Z_{11} + a^2 \cdot Z_{22} - 2a \cdot Z_{12} \tag{75}$$

Here Z_{01} and Z_{ccl} are the parameters from the traditional equivalent circuit and a is the turn ratio. Thus, values from (74) and (75) are comparable to the values obtained from the proposed method ($k \cdot R_{ij}^{FEM}$).
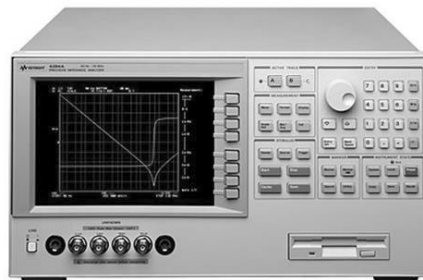
Figure 50. Analyser 4294A (Keysight Technologies)
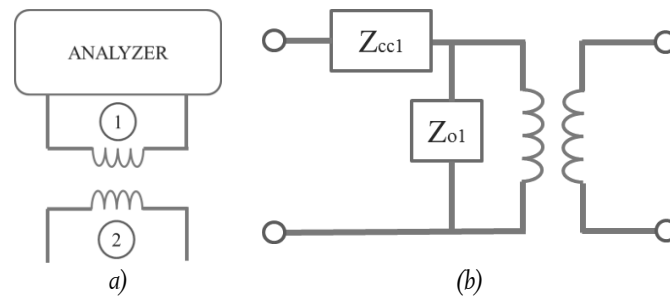
Figure 51. (a) Electrical Scheme (b)Equivalent circuit

3.4.1 *Components*

This section describes the components that have been used in the experimental validation, two are EE cores and two others are Toroidal cores.

3.4.1.1 **Component I**

Component I is an EE core transformer that is made with 3C90 material with the characteristics shown in Table 20 and Figure 52 for simulated and tested model. This component cannot be simulated with Ansys Maxwell in a common PC with 4 Gb of RAM due to its complex geometry, comprising a high number of circular conductors. The geometric model was simplified using a hexagonal conductor shape as explained previously in this chapter and the polygonal model needed a bit more than 3.12 min to converge. The methodology proposed in this thesis was used to calculate the winding resistances. Figure 53 shows the comparison between the measurement resistance and the estimated resistance for the primary and secondary windings.

Table 20. Summary of Component I data

	Reference	EE.42.21.15
	Material	3C90
Core	μ_r	500
	B_{max} (mT)	435
	H_{max} (A/m)	250
	Material	Copper
Windings: Primary	Turns	25
	Conductor	AWG18
	Material	Copper
Windows: Secondary	Turns	15
	Conductor	AWG24

Table 21. FEA data for Component I

	FE Number	CPU Time (m)
Original model	Unable	Unable
Polygonal model	23572	3,12
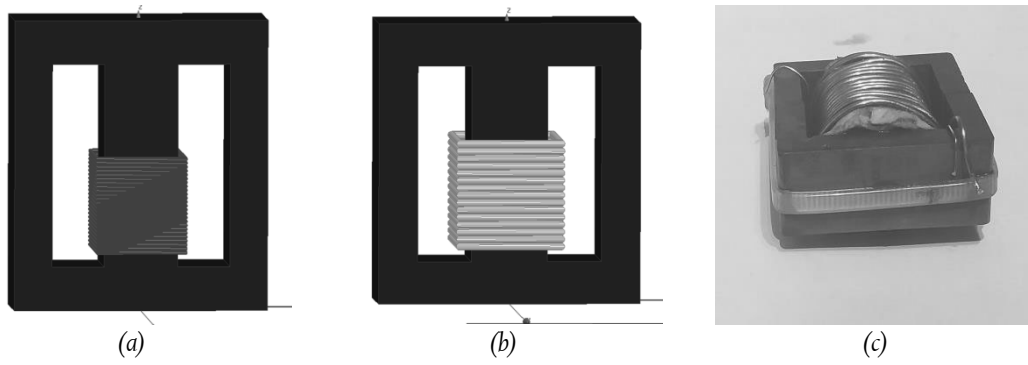
Figure 52. FEM and tested Model. Component I (a) Primary; (b) Secondary; (c) Tested Model.
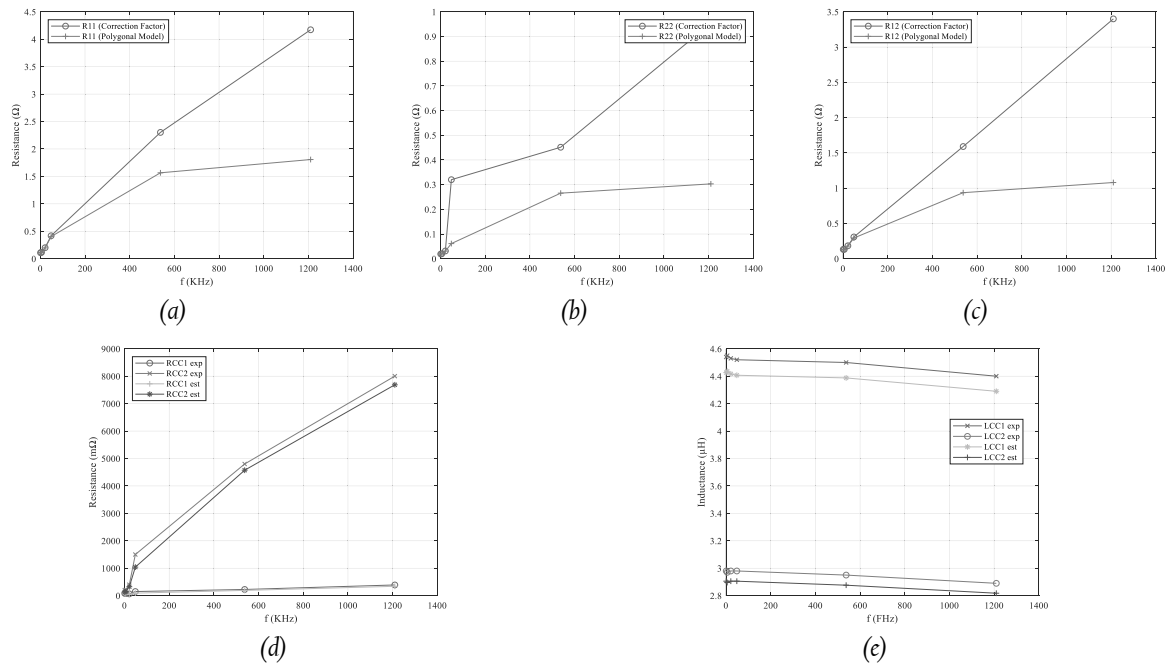
Figure 53. FEM and tested Model. Component II (a)FEA calculations (R_{11}) of Component I, (b) FEA calculations (R_{22}) of Component I, (c) FEA calculations (R_{12}) of Component I, (d) Estimated and Measured R_{cc} of Component I, (e) Estimated and Measured L_{cc} of Component I.

3.4.1.2   Component II

Component II is a Toroidal one (3F4 material) two-winding transformer as shown in Figure 54. The windings are indicated in Table 22. Once again, the high number of turns did not allow the simulation in an Ansys Maxwell with 4 Gb RAM either.

The geometry was simplified using the polygonal model (hexagonal conductors), and only 21,046 elements were needed by FEA, which allowed us to obtain the coefficients needed to estimate the power losses of the detailed component with the circular conductors (Table 23). The experimental results and the estimated calculations of the winding resistances are shown in Figure 55.

Table 22. Summary of Component II data

	Reference	C107.65.25
	Material	3F4
Core	μ_r	1700
	B_{max} (mT)	407
	H_{max} (A/m)	1000
	Material	Copper
Windings: Primary	Turns	20
	Conductor	AWG18
	Material	Copper
Windows: Secondary	Turns	20
	Conductor	AWG24

Table 23. FEA data for Component II

	FE Number	CPU Time (m)
Original model	Unable	Unable
Polygonal model	21046	9.58

(a)   *(b)*

Figure 54.FEM and tested Model. Component II (a)FEM model; (b) Tested Model.
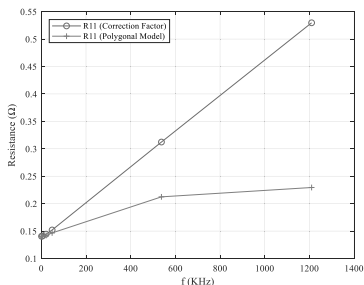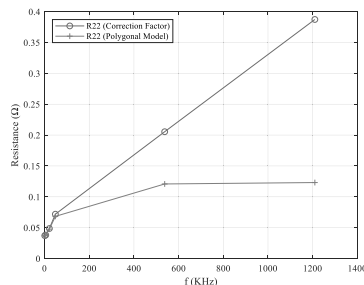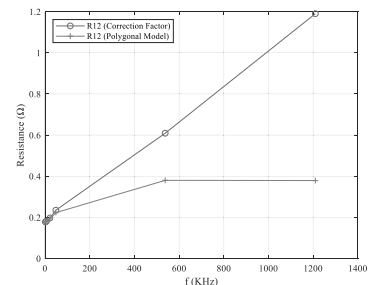
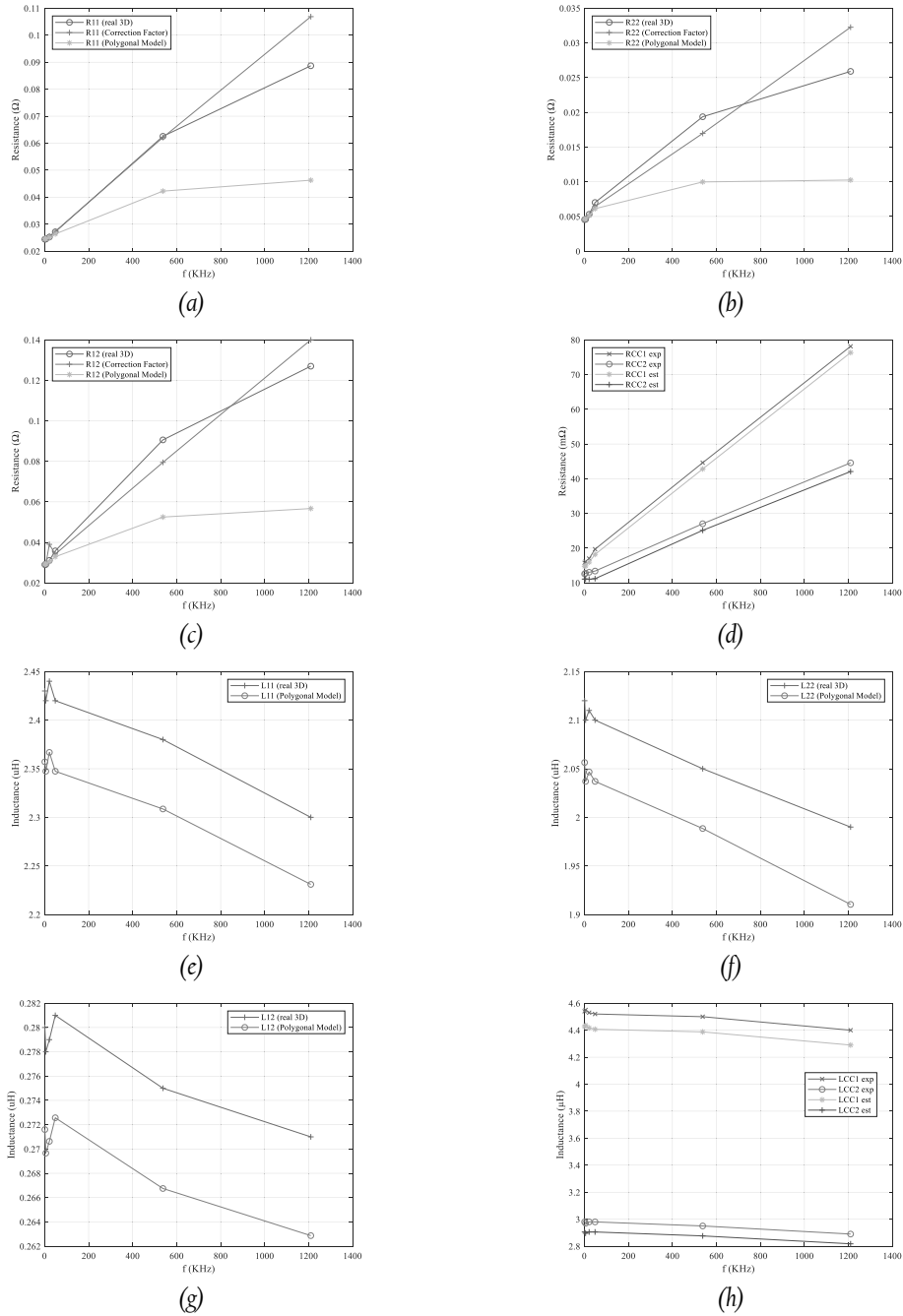*(a)*   *(b)*   *(c)*
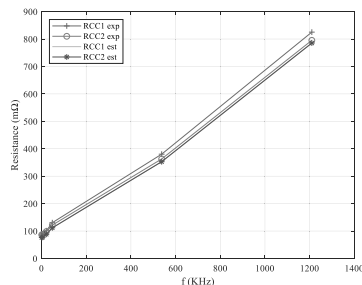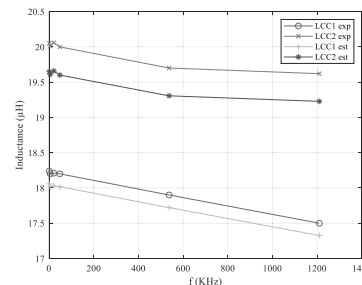
(d)   *(e)*

Figure 55. Comparison between experimental values and polygonal model (a) FEA calculations (R_{11}) of Component II, (b) FEA calculations (R_{22}) of Component II, (c) FEA calculations (R_{12}) of Component II, (d) Estimated and Measured R_{cc} of Component II, (e) Estimated and Measured L_{cc} of Component II.

Chapter 3. Proposed electrical equivalent circuit based on 3D FEM

3.4.1.3 **Component III**

Component III is a three-winding transformer with an EE.18.4.10.R core (3F4 material) shown in Figure 56 as the simulated and tested model/ The details of the windings are indicated in Table 24. This component has been chosen for two reasons:

- Three windings occupy all the core columns

- It can be simulated with Ansys Maxwell with all its geometric complexity (no polygonal simplifications) which allows us to check the advantages of using this proposed methodology.

The simulation of the detailed model needed 662635 elements and converged in 59.89 minutes and the polygonal model (hexagonal conductors) needed just 34672 elements (5% of the detailed simulation) and converged in 3.3 minutes of CPU time (6% of the detailed simulation). Figure 57 shows the calculated results and, detailed simulation, only the polygonal model simulation and resistance calculated with the polygonal model and the correction factor. The experimental validation is indicated in Figure 57(e), where the sort circuit resistances are represented. Figure 58 shows the same study for the inductance with the experimental validation.

| (a) | (b) |

Figure 56. FEM and tested Model. Component III (a) FEM model; (b) Tested Model.

Table 24. Summary of Component III data

	Reference	C107.65.25
Core	Material	3F4
	μ_r	1700
	B_{max} (mT)	407
	H_{max} (A/m)	1000
Windings: Primary	Material	Copper
	Turns	4
	Conductor	AWG18
Windows: Secondary	Material	Copper
	Turns	3
	Conductor	AWG24
Windows: Terciary	Material	Copper
	Turns	4
	Conductor	AWG24

Table 25. FEA data for Component III

	FE Number	CPU Time (m)
Original model	662635	59.89
Polygonal model	34672 (5%)	3.3 (›6%)
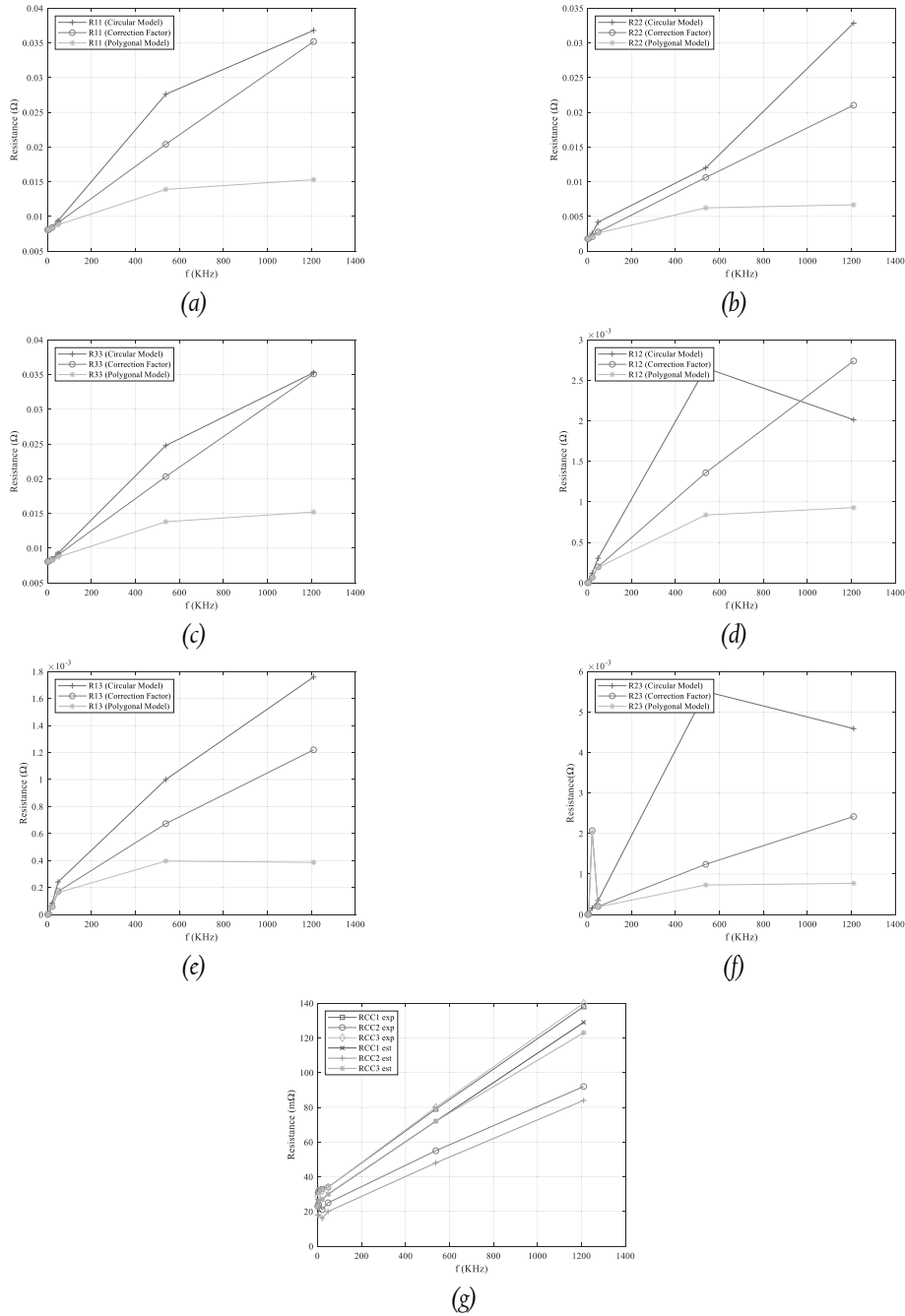
Figure 57. Comparison between experimental values and polygonal model (a) FEA calculations (R_{11}) of Component III, (b) FEA calculations (R_{22}) of Component III, (c) FEA calculations (R_{12}) of Component III. (d) FEA calculations (R_{12}) of Component III (e) FEA calculations (R_{13}) of Component III (f) FEA calculations (R_{23}) of Component III (g) Estimated and Measured R_{cc} of Component III.
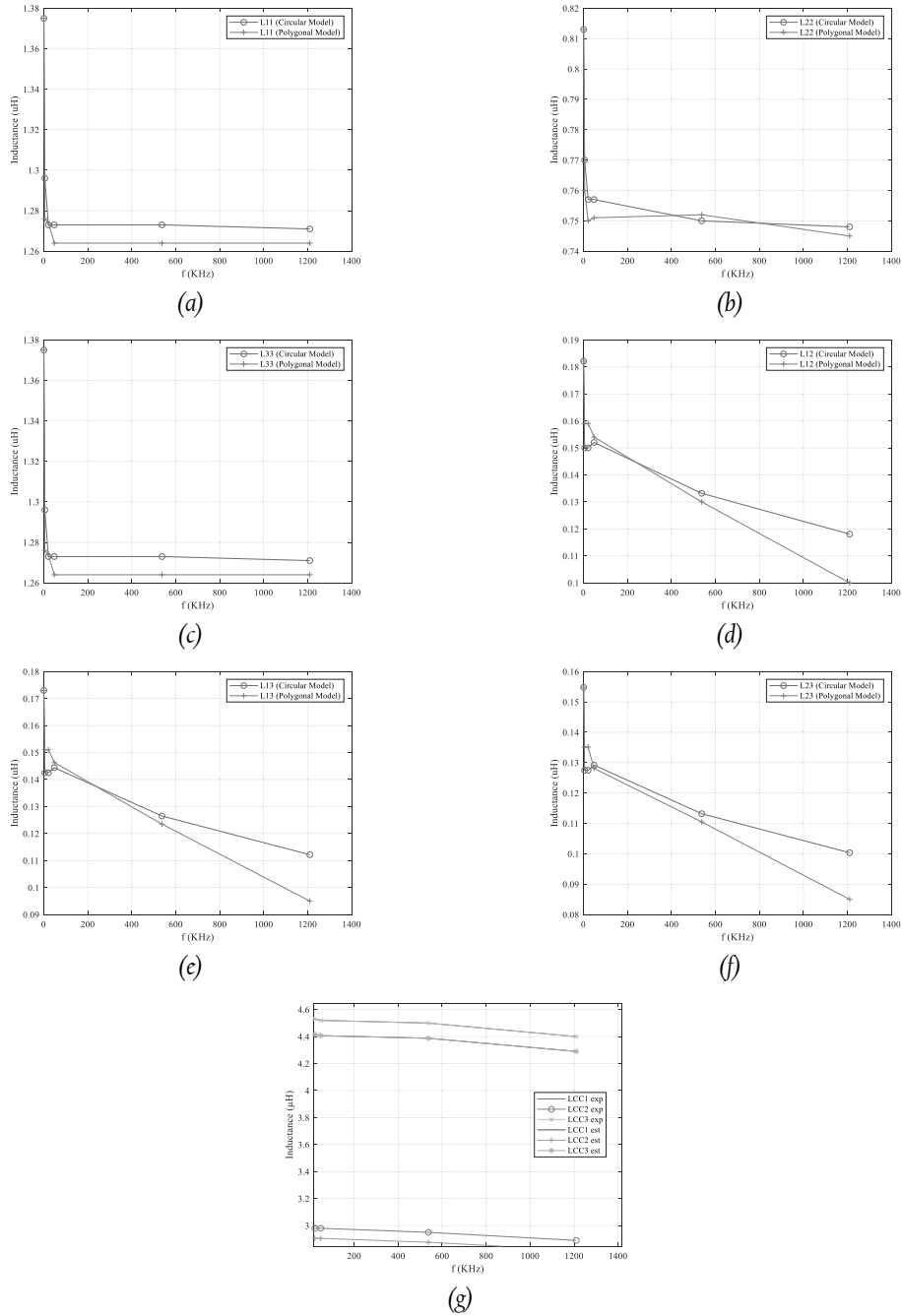
Figure 58. Comparison between experimental values and polygonal model (a) FEA calculations (L_{11}) of Component III, (b) FEA calculations (L_{22}) of Component III, (c) FEA calculations (L_{12}) of Component III, (d) FEA calculations (L_{12}) of Component III, (e) FEA calculations (L_{13}) of Component III, (f) FEA calculations (L_{23}) of Component III, (g) Estimated and Measured L_{cc} of Component III.

3.4.1.4 Component IV

Component IV is a TX25.15.10 (3C90 material) and its properties are indicated in Table 26 for the coil configuration. The model component is presented on Figure 59(a), and the tested one is displayed in Figure 59 (b). To contrast the simulated values from the real component, the polygonal one and the results using the correction factor from the values of the polygonal model are shown on Figure 60 as well as the validation for the resistance and the inductance. The simulation of the original model has 445331 elements and was performed in 111.23 min and the polygonal model has 5595 (‹2%) elements and was in 1.96 (‹2%) min (CPU time) as shown in Table 28.

| (a) | (b) |
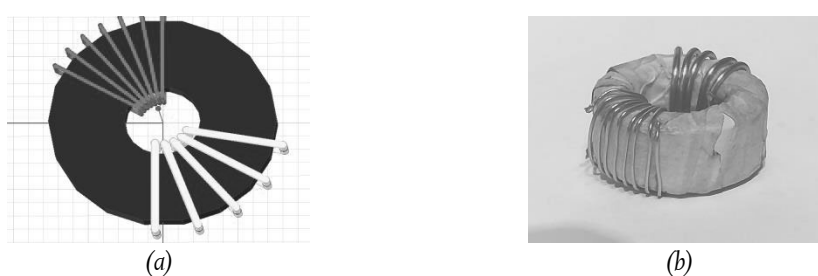
Figure 59. FEM and tested Model. Component IV (a) FEM model; (b) Tested Model.

Table 26. Summary of Component IV data

	Reference	Tx25.15.10
	Material	3C90
Core	μ_r	5500
	B_{max} (mT)	435
	H_{max} (A/m)	250
	Material	Copper
Windings: Primary	Turns	7
	Conductor	AWG18
	Material	Copper
Windows: Secondary	Turns	5
	Conductor	AWG24

Table 27. FEA data for Component IV

	FE Number	CPU Time (m)
Original model	445331	111,23
Polygonal model	5595 (‹2%)	1.96 (‹2%)

Figure 60. Comparison between experimental values and polygonal model a) FEA calculations (R_{11}) of Component IV, (b) FEA calculations (R_{22}) of Component IV, (c) FEA calculations (R_{12}) of Component IV, (d) Estimated R_{cc} of Component IV, (e) FEA calculations (L_{11}) of Component IV, (f) FEA calculations (L_{22}) of Component IV, (g) FEA calculations (L_{12}) of Component IV, (h) Estimated L_{cc} of Component IV.

3.4.2 *Results discussion*

The errors produced depending on the frequency are shown in Table 28, which summarises the error for each of the studied components. The effect of the winding edge and the terminal connection has been removed to determinate the error between the proposed method and the performed experimental values. The analyser´s measurements are similar to the simulation results obtained with the proposed method for all tested components up to low-medium frequencies (-500 kHz). The biggest error 8.7 % at 1.2 GHz for case II, and even in this case the error is much lower than that the obtained with other known methods [59] applied to multi-winding components, that is close to 25 %. In addition, the frequency range is far away for the operation frequency for the interest of this research.

For the four components, the FE number is reduced about 95 % from the circular to the hexagonal model, requiring a negligible computational time as compared to initial simulation using the model without simplifications. Graphically at the figures, the error seems bigger because of the scaling to better show the tendency, but errors in Table 28 for the cases are lower than 5% for all the frequency range.

The values corresponding to the core magnetic field density (Figure 61) for components I, II, III and IV respectively) obtained with the simplified model are very similar to those obtained with the simulation run without any simplification, but requiring much less CPU simulation time. The extrapolated thermal analysis will be also valid using the simplified proposed method. In addition, Figure 58 and 60 allow concluding that a correction factor is required for the resistive parameter but no for the inductive parameter.

Therefore, one of the major original contributions from this thesis is the new proposed methodology to simulate magnetic components in 3D and the parameter extraction and applying the correction factor that has been validated even for 1 GHz.

Table 28. Summary of the Resistance Errors (%)

Error (%)		f (kHz)					
		0.001	5.38	21.51	48.39	537.68	1,209.78
Case I	R_1	1.42	1.29	2.37	3.80	5.1	5.7
	R_2	3.42	2.75	1.84	3.06	4.7	5.2
Case II	R_1	1.16	1.42	1.29	1.44	7.2	7.4
	R_2	2.09	2.55	2.31	2.59	7.6	**8.7**
Case III	R_1	1.64	1.92	1.78	1.40	3.2	4.1
	R_2	2.22	2.59	2.55	1.91	1.35	4.2
	R_3	1.64	1.92	1.78	1.40	3.2	4.1
Case IV	R_1	0.63	0.74	0.75	0.76	0.40	0.23
	R_2	1.19	1.33	1.53	1.64	0.70	0.56
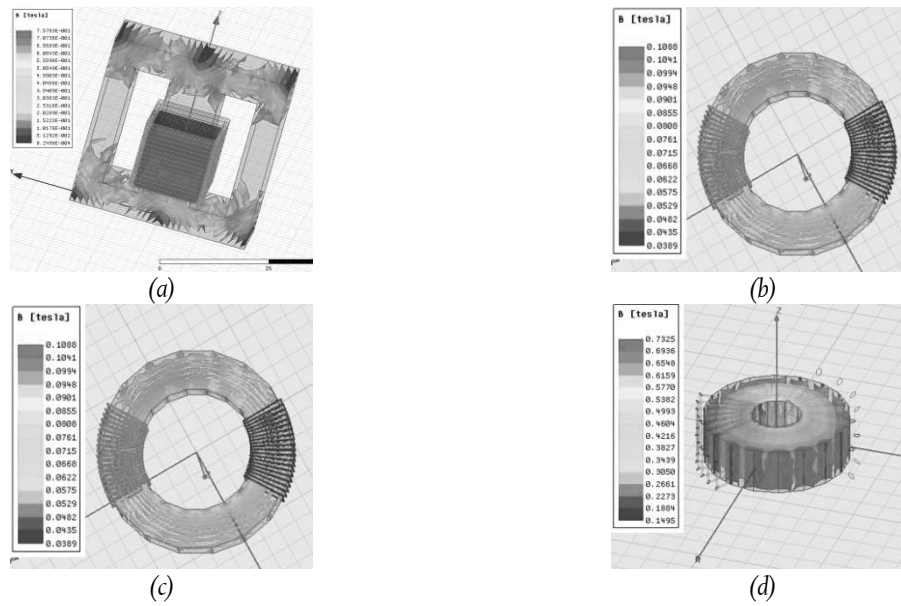
Figure 61. Magnetic field density from FEM (a) Component I (b) Component II (c) Component III (d) Component IV.

3.5 Guide to apply the proposed method for power electronics engineers

In the last section, the developed study by using 3D FEM has been validated to propose the original procedure to model components in 3D in an operative CPU time to be useful in the optimisation process to minimise the winding losses and determine parameters of the equivalent electrical circuit for an inductor or transformer.

This section presents a guide of the procedure to model any magnetic component in 3D in Ansys Maxwell using an example to make easier the understanding. The example selected is an inductor (EE core 42.21.15 with 3C90 material) with 2 windings.

Steps:

1. Open the Ansys Maxwell in the 3D drawing tool in the Eddy Current Solver

2. Draw the Component in three dimensions without any simplifications at this point. The exact geometry of the example is shown in Figure 62 in three dimensions in the software itself or imported from another application.
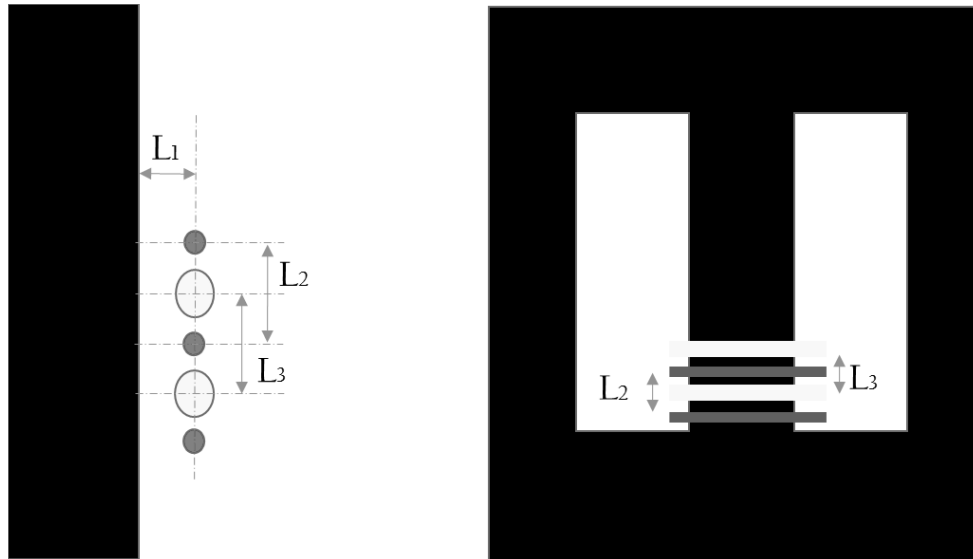
Core:
EE.42.21.15 material: 3C90

Windings:
Primary: 16 turns (AWG18)
Secondary: 15 turns (AWG24)

Distances:
L_1=1.47 mm
L_2=1.90 mm
L_3=1.96mm

Figure 62. Geometry of the example.

3.   Assign the boundaries for the problem. The recommended boundary is a cube over 5 times bigger than the maximum edge of the core keeping the component at the centre of the cube (Figure 63), defining in the border the tangential field as null.
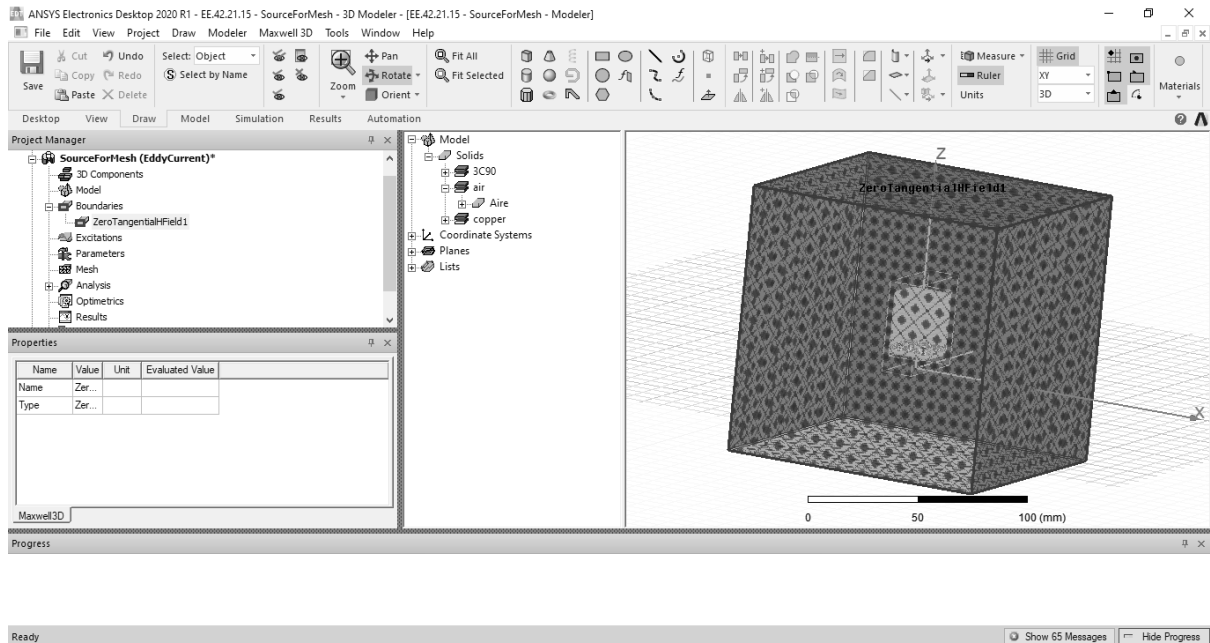
Figure 63. Boundary definition.

(a)   (b)
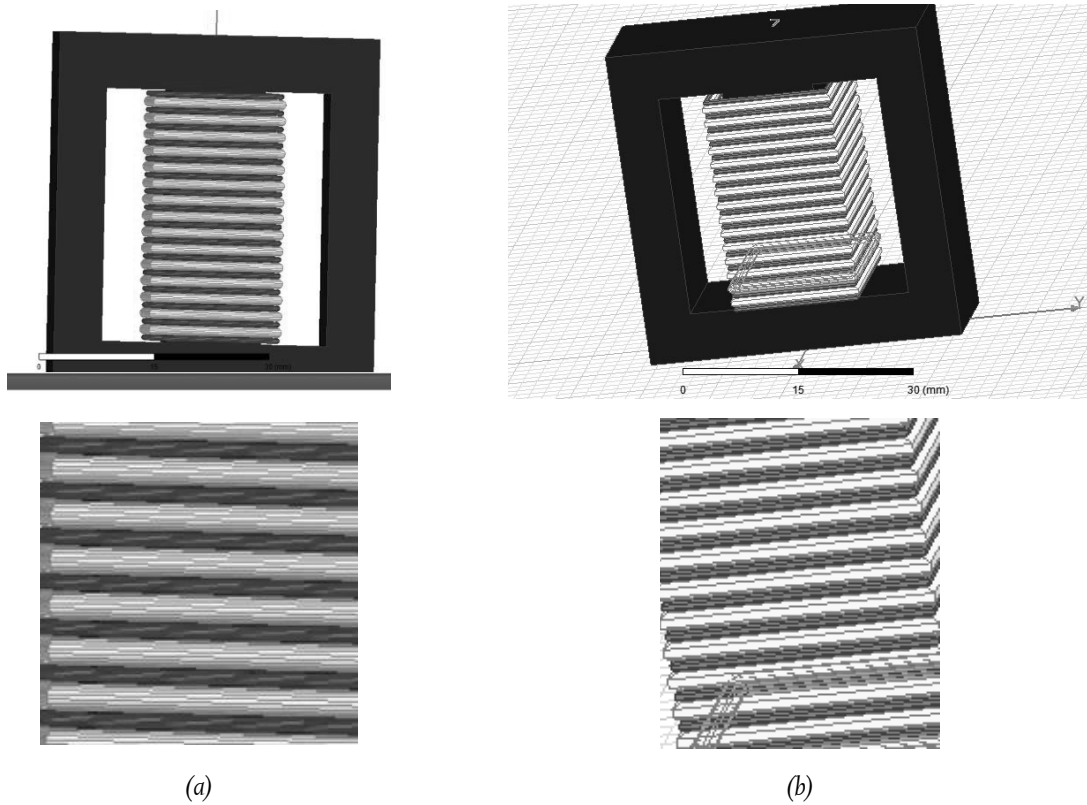
Figure 64. Modification of the winding cross-section (a) Circular (b) Hexagonal.

4. Modify the cross-section of the windings from the circular to hexagonal to reduce the CPU time for the simulation (Figure 64).

5. Define of the material properties in the settings of the software (Figure 65) per each material of the simulation as air/vacuum, 3C90 and copper. Note that in this step, as the hexagonal section has been introduced, the material properties of the copper have to be adjusted according the equations explained in the chapter. For this example, the conductivity and the permeability to be introduced are defined in (77) and (78).

$$\sigma_{Pol} = A_{pol} \cdot \sigma_{Circular} = \frac{S_{Circular}}{S_{hexagon}} \cdot \sigma_{Circular} = \frac{\pi \cdot r^2}{3/2 \cdot \sqrt{3} \cdot r^2} \cdot \sigma_{Copper} \qquad (77)$$

$$\mu_{Pol} = A_{pol} \cdot \mu_{Circular} = \frac{S_{Circular}}{S_{hexagon}} \cdot \mu_{Circular} = \frac{\pi \cdot r^2}{3/2 \cdot \sqrt{3} \cdot r^2} \cdot \mu_{Copper} \qquad (78)$$

Guide to apply the proposed method for power electronics engineers
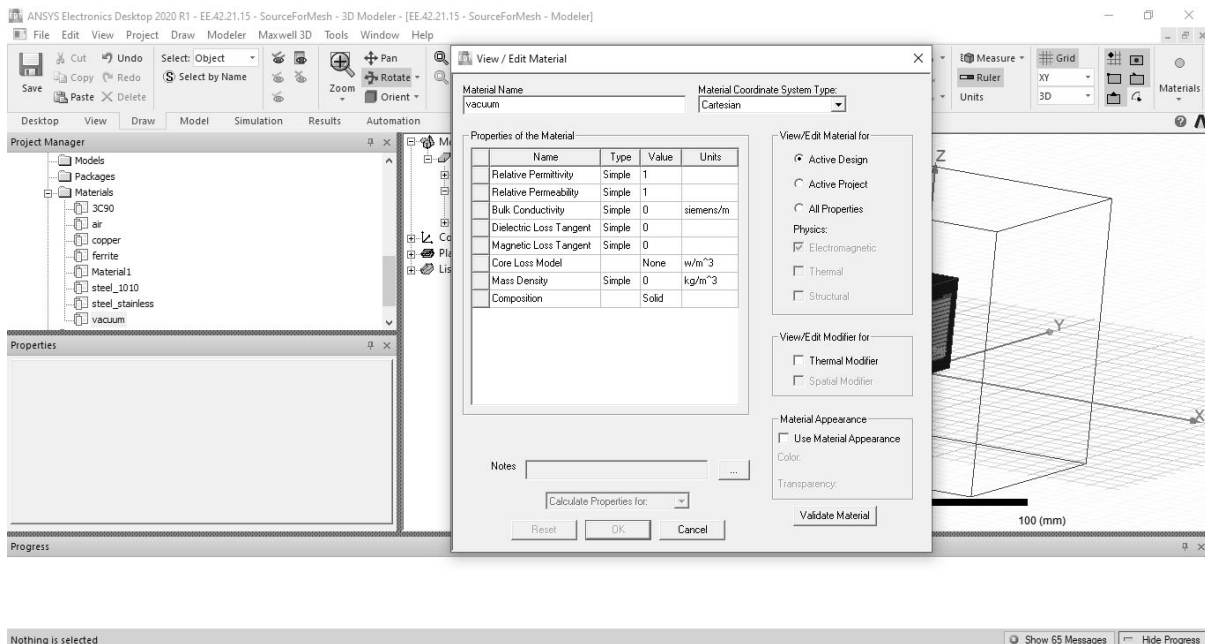
Figure 65. Definition of the material properties

6. Introduce the current in the winding. This step is divided in two sub-steps, the first one being the definition of the current value in the windings being able to define any waveform shape (Figure 66 a). The second step is the introduction of the current in a specific cross-section of the winding to select the orientation of the current (Figure 66 b).
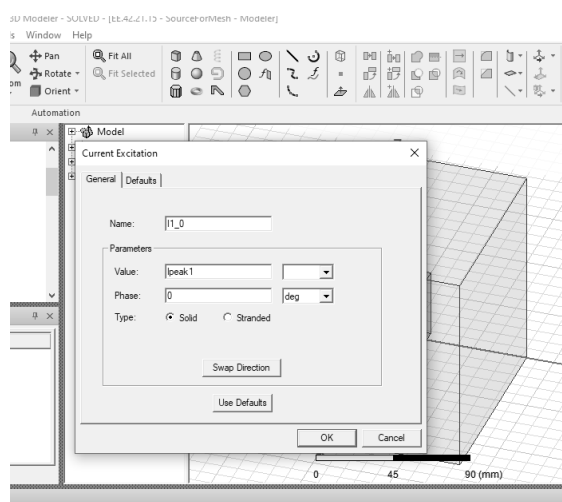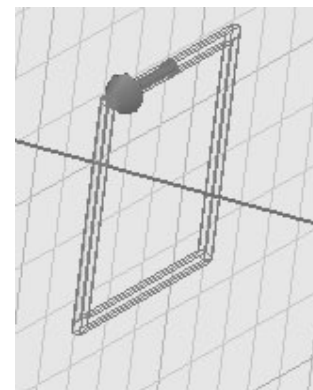
(a)   *(b)*

Figure 66. Introduction of the winding current (a) Definition of the value of the current (b) Winding section to introduce the current.

7. Configure the mesh automatically. The mesh configuration could be one of the most difficult tasks in the simulation process. However, this action is outside of the thesis topic.

8. The Solver setup step is used to defined the energy error of 2%, 25 maximum number of

Chapter 3. Proposed electrical equivalent circuit based on 3D FEM

steps and step refinement of 20%, Also, the frequency sweep has to be defined for the simulation or the frequency operation point of the interest.
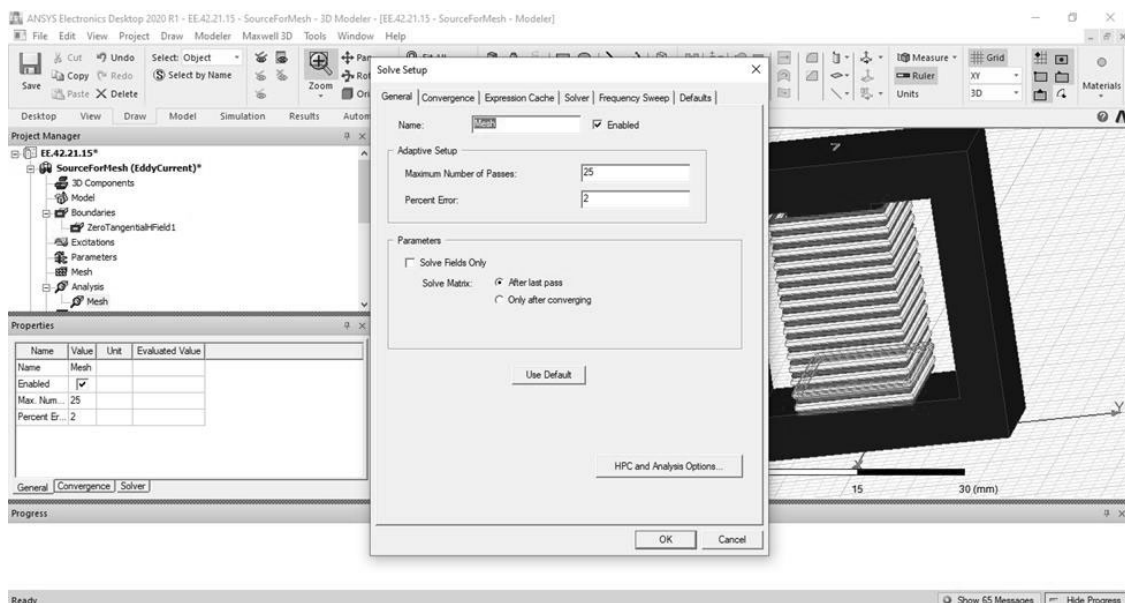
Figure 67. Solver Setup.

In the case that the inductor has more than one winding, it is necessary to create a component named SourceForMesh with all the windings working at the same time in order to extrapolate this mesh of this component in the other simulations analyses in open circuit status to have a common mesh for not introducing additional computation errors. For this example, there will be the SourceForMesh to create the common mesh and Setup1 for analysis for the primary and Setup2 for the secondary.

9. Simulation phase. At this point, the problem is ready to start the simulation, so the software allows checking the geometry and, settings, and the simulation could be started. In the proposed case the CPU time is 3.47 min for the primary and 4.12 min for the secondary.

10. Result-processing is the step to calculate the L and the R of the windings. For this reason is necessary to calculate a map of $\vec{B}$, $\vec{H}$ and $\vec{J}$ in the volume enclosed by the boundaries. Lij and Rij, in this case, are R_{11}, R_{22}, R_{12} and L_{11}, L_{22}, L_{12} being determined by two scripts programmed in JAVA to export the results in txt.files or xlxs.files. The L and R obtained are the electrical parameters from the polygonal model. These scrips are shown in Appendix IV.

$$L_{ij} = \frac{1}{I_o^2} \oiiint_{V_w} \frac{1}{\mu} \cdot Re\left(\vec{B}_{io} \cdot \vec{B}_{jo}^*\right) dv \tag{79}$$

$$R_{ij} = \frac{1}{I_o^2} \oiiint_{V_w} \frac{1}{\sigma} \cdot Re\left(\vec{J}_{io} \cdot \vec{J}_{jo}^*\right) dv \qquad (80)$$

The results for the electrical parameters have been obtained in the frequency operation points where they have been defined in the frequency sweep in the solver setup. For example, if the analysis has been performed for 3 frequency points: 1kHz, 10kHz and 250kHz, the results are the following with the scripts (Table 29).

Table 29. Summary of the Electrical Parameters from Scripts

f_1=1 kHz		f_2=10 kHz		f_3=250 kHz	
$R_{11}(f_1)$,	76.8 mΩ	$R_{11}(f_2)$,	79.75mΩ	$R_{11}(f_3)$,	170.16mΩ
$R_{22}(f_1)$,	19.19mΩ	$R_{22}(f_2)$,	23.25mΩ	$R_{22}(f_3)$,	130.25mΩ
$R_{12}(f_1)$,	95.66mΩ	$R_{12}(f_2)$,	96.09mΩ	$R_{12}(f_3)$,	155.99mΩ

To obtain the correct values, the correction factor has to be applied following the equations (81) -(83):

$$EQ_R = A_{pol} \cdot r_1^{1/2} \cdot f \qquad (81)$$

$$k_{skin} = e^{\left(\frac{EQ_R}{1000}\right)} \qquad (82)$$

$$k_{prox} = e^{\left(\frac{A_{pol}}{1000}\frac{n}{k_C}r^{1/2}\right)\cdot f} \qquad (83)$$

The example used the hexagonal section and two conductors (AWG18 and AWG24), whereby the corrections factors are indicated in Table 30 and 31.

Table 30. Correction factor for AWG18

r=AWG18	f_1=0.001kHz	f_2=10 kHz	f_3=250 kHz
k_{skin}	1.000894	1.0089	1.2504
k_{prox}	1.000149	1.00149	1.03795
$k = ln(e^{k_{skin}} + e^{k_{prox}})$	1.001013	1.0104	1.2883

Table 31. Correction factor for AWG24

r=AWG24	f_1=0.001kHz	f_2=10 kHz	f_3=250 kHz
k_{skin}	1.00641	1.00642	1.17369
k_{prox}	1.000107	1.001068	1.027
$k = ln(e^{k_{skin}} + e^{k_{prox}})$	1.0006	1.00749	1.2007

The final results are, L from the polygonal model and R from the polygonal model multiplied by the correction factor k are shown in Table 30 and 31 that they are shown in Table 32.

Table 32. Numerical Results of the electrical parameters for the example

f_1=1 kHz		f_2=10 kHz		f_3=250 kHz	
$k(f_1) \cdot R_{11}(f_1)$,	76.9 mΩ	$k(f_2) \cdot R_{11}(f_2)$,	80.58 mΩ	$k(f_3) \cdot R_{11}(f_3)$,	219.23 mΩ
$k(f_1) \cdot R_{22}(f_1)$,	19.21 mΩ	$k(f_2) \cdot R_{22}(f_2)$,	23.25 mΩ	$k(f_3) \cdot R_{22}(f_3)$,	156.4 mΩ
$k(f_1) \cdot R_{12}(f_1)$,	95.72 mΩ	$k(f_2) \cdot R_{12}(f_2)$,	96.81 mΩ	$k(f_3) \cdot R_{12}(f_3)$,	187.3 mΩ

4 Core power losses analysis based on FEM

This chapter is dedicated to the core power losses, describing the original per-unit method for the core losses determination and the application for the toroidal cores obtaining an analytical equation for hysteresis and eddy current losses valid for any frequency range. This section finishes with the validation of this method and the particular equation with benchmarking with other methods according to the corresponding frequency range.

4.1 Core power losses

Losses in magnetic cores have been studied because of their particular significance for the component design. Physicists study the characteristics in magnetic materials, while design engineers in power electronics model the core power losses (CPL). Nevertheless, there is a gap between the power losses calculation theories, particularly those focused in the material characteristics, and engineering applications. In consequence the devices designed cannot fully use the material capabilities.

One set of models is based on the Steinmetz equation where the three coefficients are determined by fitting the losses model to the measurement data, this model assumes purely sinusoidal flux densities. An extension of Steinmetz equasion[86] was presented by Jordan in [87] which it is described an iron losses model where the static hysteresis losses (HL) and dynamic eddy current losses (ECL) were separated. Pry and Bean added the excess losses [88], subsequently, Bertotti developed a new theory to calculate the losses by introducing the concept of magnetic objects into the component, which led to the model with excess losses in terms of the active magnetic objects and the domain wall motion [89,90]. The linear magnetization, rotational magnetization and higher harmonics were added afterwards with iron losses separation, being established in [91,92].

Chapter 4. Core power losses analysis based on FEM

In the last decades, the Steinmetz equation has been continuously improved. As in [93] where the Modified Steinmetz equation was presented for arbitrary waveforms and the Generalized Steinmetz equation [94] presenting the idea of the instantaneous iron losses as a single valued function of the flux density. The improved Generalized Steinmetz equation in [95] was developed to avoid the limitation existing in the third higher harmonic. In [96], a new equation named the "improved-improved generalised equation" for rectangular shapes voltages was presented. To obtain a higher accuracy, hysteresis models by Preisach and Jiles-Atherton were developed [35,97]. An improvement for the model of Preisach was presented in [98] including a dynamic part divided in two sections, establishing the maximum and minimum values of the flux density according to the material. A new hysteresis model based on an energy approach where the magnetic dissipation from the macroscopic point of view was represented by a friction-like force was introduced in [99] and some important advances for nonlinear behaviour of the magnetic cores was done in [100]. A new model which describes this switching behaviour implemented in Matlab is in [101]. Analysis for non-sinusoidal signals for specific components has been developed in the last few years [102-107].

The referenced gap is produced because engineers usually design devices based on models with different parameters than physicists use. However, these models are typically only appropriate for a defined frequency range. The practical disadvantage of most of these methods is that require additional measurements for a given material.

The empirical and losses separation models are preferable and best suited for fast and rough iron losses determination. The complex HL models are more adequate for an exact iron losses calculation, but they need more information about the material or make material measurements as well as the flux density waveforms information. Another huge issue is the integration into FE tools. The proposed methodology gives an original equation to determine the CPL for components used in switched mode power supplies (normally in non-saturation state) for any signal based 3D FE analyses.

Ansys Maxwell, in Transient Solver allows studying the CPL including the real hysteresis loop data [76] in the FE tool as an input (not just a material permeability coefficient).This FEM with an energy error of 2% and a standard mesh [77] has been selected to analyse the asymmetric components in 3D for different core material and operations, ranging from 1 kHz to 1 GHz achieving a final equation for the CPL for any Toroidal core component.

This chapter outlines a deep 3D analysis of the core power losses for magnetic components to achieve a quick losses model defined only by geometric and material parameters (winding current is included) to estimate the CPL without any anterior simulation or test. The proposed

model has been validated with experimental results and methods in the frequency range where they are valid giving a very quick process to calculate the CPL with the same accuracy of the current models.

The proposed methodology also opens a new path to analyse the core losses for other different cores used in inductive components of power converters where they are 3D modelled to be analysed as needed. This methodology could use models in 1D or 2D as well. But, 3D models are used in this study to contemplate all the effects in magnetic components that appears in high-low frequency ranges.

4.1.1   Core losses definition

The CPL is mainly classified into three types: HL, ECL and excess losses (P_{ex}):

$$P_{CPL} = P_{HL} + P_{ECL} + P_{ex} \tag{84}$$

Different theories have been developed to include the excess losses. Some studies based on the statistical losses theory derived the excess losses from the flux density change due to the motion of randomly distributed domain walls. On the other hand, in a different approach, excess losses are attributed to the peculiar nature of nonlinear electromagnetic field diffusion in the lamination. However, in this work, the excess losses have been considered negligible, considering only the hysteresis and eddy current losses.

4.2 Hysteresis losses description

When a ferromagnetic material is located in a magnetic field, it is magnetized by induction. If the intensity of the magnetic field $\vec{H}$ is varied, the magnetic flux density $\vec{B}$ in the ferromagnetic material does not change linearly with $\vec{H}$. The susceptibility and the permeability of the material are not constants but vary with the magnetic field and it is also dependent on the magnetic field variations suffered by the material (Figure 68).

The magnetization remaining in the material when the magnetizing field is reduced to zero is called the residual magnetism. The capacity of retaining residual magnetism is called the retentivity of the material. The residual magnetism of a material can be wiped off by applying a magnetizing force in the opposite direction. The value of magnetizing force required to wipe of its residual magnetism is called corrosive force.
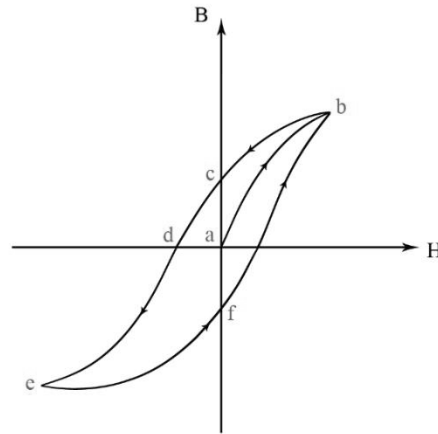
Figure 68. Hysteresis loop [108].

Thus, if $\vec{H}$ reaches the maximum value and returns to the zero, the materials domains that were increased in size and orientation to the magnetic field, struggle to recover the initial state, however, just several ones are available to get back to the initial orientation. The reasoning for this is that the hysteresis is a loop and causes difficulty to move the wall domains according to the magnetic field. So, in the first magnetization the material, the curve follows one path but afterwards, when $\vec{H}$ is increased or decreased, the material follows a different curve because of this phenomenon of the magnetic hysteresis.

4.3 Eddy current losses description

Eddy currents (also called Foucault currents) are loops of electrical current induced within conductors by a changing magnetic field in the conductor as stated by Faraday's law. They can be induced within nearby stationary conductors by a time-varying magnetic field created by an AC electromagnet or by relative motion between a magnet and a nearby conductor. The magnitude of the current in a given loop is proportional to the strength of the magnetic field, the enclosed area and the rate of change of flux, and is inversely proportional to the resistivity of the material.

An eddy current creates a magnetic field that opposes the change in the magnetic field that created it, and thus eddy currents react back on the source of the magnetic field according to the Lenz's law. This effect is employed in eddy current brakes which are used to stop rotating power tools quickly when they are turned off.

The current flowing through the resistance of the conductor also dissipates energy as heat in the material, thus eddy currents are a cause of energy losses in alternating current (AC) inductors, transformers, electric motors and generators, and other AC machinery.
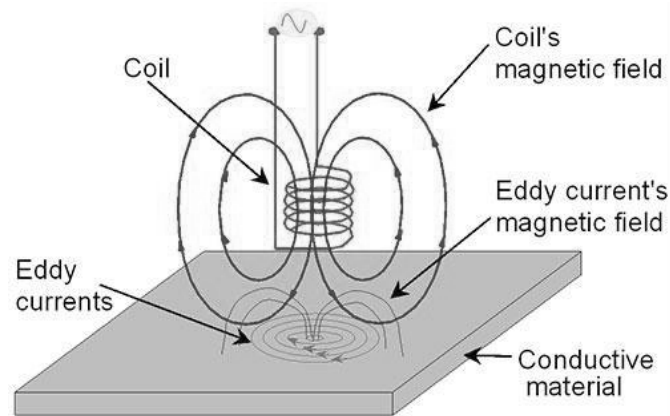
Figure 69. Eddy Current loop [109].

This requires special construction such as laminated magnetic cores or ferrite cores to minimize them. Eddy currents can be also used to heat objects in induction heating furnaces and equipment, and to detect cracks and flaws in metal parts.

A magnet induces circular electric currents in a metal sheet moving past it. Figure 69 shows a metal sheet moving to the right under a stationary magnet.

The magnetic field density $\vec{B}$ of the magnet's north pole N passes down through the sheet. Since the metal is moving, the magnetic flux through the sheet is changing. At the part of the sheet under the leading edge of the magnet (left side) the magnetic field through the sheet is increasing as it gets closer to the magnet. From induction defined by Faraday's law, a circular electric field appears in the sheet in a counterclockwise direction around the magnetic field lines. This field induces a counterclockwise flow of electric current in the sheet that are called eddy currents. At the trailing edge of the magnet the magnetic field through the sheet is decreasing, inducing a second eddy current in a clockwise direction in the sheet (Figure 69).

Due to Ampere's circuital law, each of these circular currents creates a counter magnetic field which due to Lenz's law opposes the change in magnetic field which caused it, exerting a drag force on the sheet. At the leading edge of the magnet by the right-hand rule the counterclockwise current creates a magnetic field pointed up, opposing the magnet's field, causing a repulsive force between the sheet and the leading edge of the magnet. In contrast, at the trailing edge the clockwise current causes a magnetic field pointed down, in the same direction as the magnet's field, creating an attractive force between the sheet and the trailing edge of the magnet. Both forces oppose the motion of the sheet. The kinetic energy which is consumed overcoming this drag force is dissipated as heat by the currents flowing through the resistance of the metal, so the metal gets warm under the magnet.

(a) *(b)*
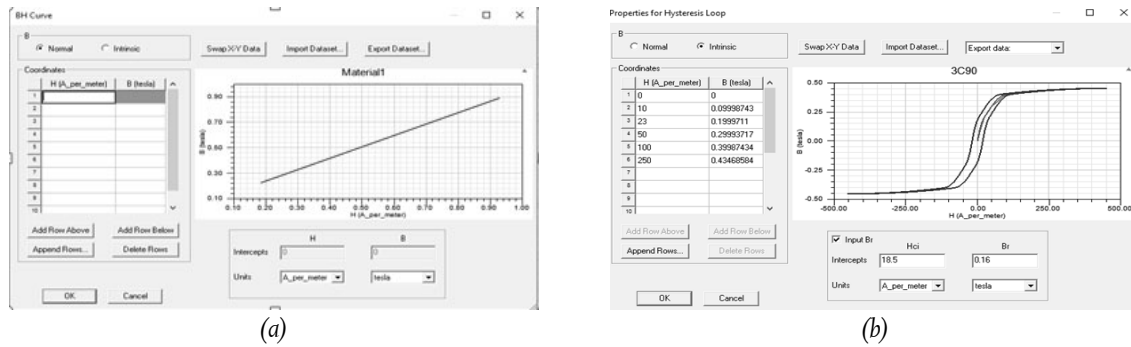
Figure 70. Eddy Current Solver Vs Transient Solver (a) Eddy Current Solver (b) Transient Solver.

4.4 Analysis of losses under finite element tools

The FE analysis has been performed by Ansys Maxwell with 3D models to include all effects involved in low and high frequency. The FEA's have been solved by transient solutions in order to be able to introduce the hysteresis loop data in the software (Figure 70).

The eddy current solver only allows introducing a linear permeability of the material, and in transient solver instead is possible to introduce the material loop data, thus, the coercivity of the material is considered in the FEM.

The component modelled in the FEA software is divided in number of elements (mesh) where the Maxwell's equations are determined using a complex relative permeability that causes that $\vec{B}$ field to lag behind the $\vec{H}$ field similar to a behaviour of a non- linear system. In addition, the characteristics of the magnetic materials are represented with their main parameters: residual flux density B_r, coercive field force H_c, and the maximum energy product $(BH)_{max}$.

Therefore, the magnetic material is a magnetic source similar to the electric source in the electric circuit. According to the frequency and the magnetic field density of a point in the mesh, a fitting curve is developed to determine the (B, H) point used from the hysteresis loop to calculate the system of equations of Maxwell. Hence, the three dimensional vectors $\vec{B}, \vec{H}$ are determined in each point of the mesh and with the Maxwell's equations, $\vec{J}$ is calculated as well.

4.4.1 Analysis of hysteresis losses

The total HL of a component can be calculated by integrating the HL density over a proper volume. Considering a unit volume of core material, starting from point 1 (Figure 71), H is zero and is increased to $H_{max,}$. The energy absorbed by the unit volume is:

$$\Delta W_1 = \int_{-Br}^{Bmax} HdB \tag{85}$$

This amount of energy represents the area in figure 71, if H is decreased from H_{max} to 0, the path taken by the B-H characteristic is from point 2 to the point 3. The energy is represented in Figure 71 (c).

$$\Delta W_2 = \int_{Bmax}^{Br} HdB \tag{86}$$

This energy input is negative since H is positive, but since ΔB is negative, ΔW_2 represents the energy given up a unit volume of the core. If H is now taken from zero to $-H_{max}$, the path 3-5 is traced. The energy put into the core material is represented by the area in Figure 71 (d).
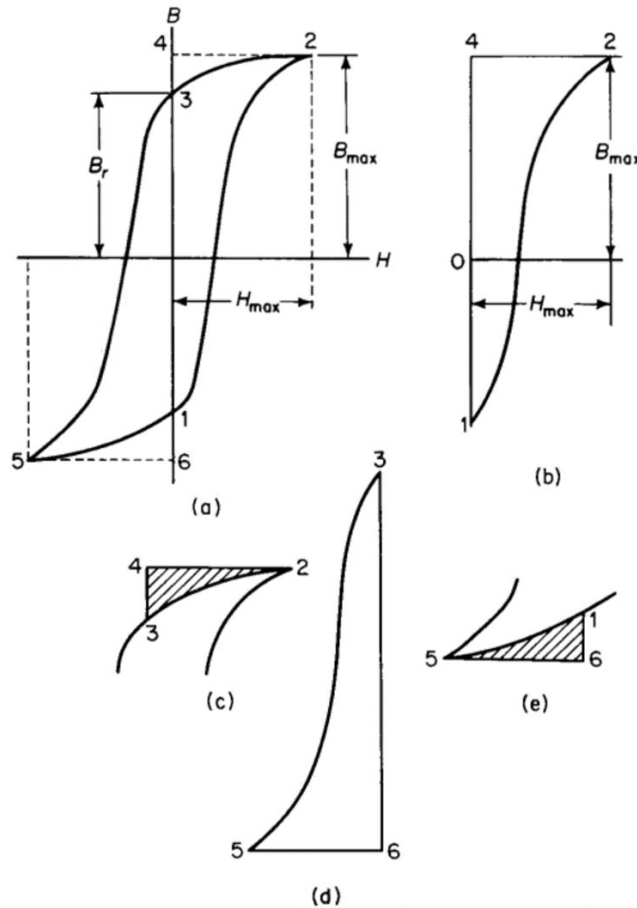
Figure 71. Hysteresis loop and energy absorbed [110].

$$\Delta W_3 = \int_{Br}^{-Bmax} H dB \tag{87}$$

If H is negative and ΔB is negative, the energy is positive. If H is now increased from $-H_{max}$, the cores gives up an amount of energy represented by the shaded areas in Figure 71 (e).

$$\Delta W_4 = \int_{-Bmax}^{-Br} H dB \tag{88}$$

If H is negative and ΔB is positive, the absorbed energy is negative. This means that the core gives up energy. If the sum of the 4 values of energy is taken with due regard for the signs, whether positive or negative, the total energy is presented by the area of the total hysteresis loop. Thus, for a core having a volume, and a uniform flux density B thought the entire volume, the energy losses are:

$$W_{HLu} = W_1 - W_2 + W_3 - W_4 \tag{89}$$

$$W_{HL}(J) = \int_v W_{HLu}\, dv \tag{90}$$

where v is the total volume, in the case of the flux undergoing a cyclic variation at a frequency f, there are hysteresis loops per second, and the power is:

$$P_{HL} = f \cdot W_{HL} \tag{91}$$

Following this equation and translating to the Maxwell Calculator, the magnetic hysteresis losses density (p_{HL}) is given by the following expression:

$$p_{HL} = \frac{1}{2} \cdot \omega \cdot Im(\vec{B} \cdot \vec{H}^*)\ (J/m^3) \tag{92}$$

The hysteresis losses under Finite elements tool are given by:

$$P_i = \frac{1}{2} \cdot \omega \int_v Im(\vec{B} \cdot \vec{H}^*) dv\ (J) \tag{93}$$

where $\vec{B}$ is the magnetic flux density, $\vec{H}^*$ is the complex conjugate of the magnetic field and ω is the angular frequency.

4.4.2 Analysis of Eddy current losses

These losses arise from the fact that the core itself is composed of conducting material, so that the voltage induced in it by the varying flux produces circulating currents in the material. ECL depends upon the rate of change of flux as well as the resistance of the path. It is reasonable to expect these losses to vary as the square of both the maximum flux density and frequency

if the core is solid and made up from ferromagnetic materials, and it effectively acts as a single short circuited turn. Induced eddy currents therefore circulate within the core in a plane normal to the flux, and cause resistive heating of the core material [77].

$$P_{ECL1} = \frac{1}{2\sigma_{core}} \int_v \left(\vec{J} \cdot \vec{J}^*\right) dv \text{(J)} \tag{94}$$

Where $\vec{J}$ is the current density, $\vec{J}^*$ is the complex conjugate of the current density and σ_{core} isthe conductivity in the core. For the surfaces, the eddy current losses are defined according to [51] by:

$$P_{ECL2} = \sqrt{\frac{\omega \mu_o \mu_r}{8\sigma_{core}}} \cdot \int_{S_l} \vec{H}_t \cdot \vec{H}_t^* \, ds \text{(J)} \tag{95}$$

Where $\vec{H}_t$ is the tangential component of the $\vec{H}$ on the boundary, S_l, and $\vec{H}_t^*$ is the complex conjugate tangential component of $\vec{H}$ on the boundary. These losses must be calculated for each surface of the core. In the case of the Toroidal core, there are 4 surfaces (Top, down, inner circular and outer circular ones)

Thus, the total eddy current losses are defined by:

$$P_{ECL} = P_{ECL1} + P_{ECL2} \tag{96}$$

4.5 Per unit CPL method

The analysis of the CPL has been performed with the original methodology based on the concept named per-unit CPL:

$$p_{CL} = \frac{P_{CL}}{P_{CL,RC}} \tag{97}$$

where P_{CL} is the CPL of any core model in a particular frequency and $P_{CL,RC}$ is the CPL for the Reference Component (RC) at the same frequency.

The original methodology consists on the following steps:

1. Selection of the inductor to be studied for optimization (type of core).
2. Selection of the RC (with the same core of the inductor to be studied).
3. Assortment of the materials for the core, calculating the area in the hysteresis loops by a polynomial regression.
4. Division of the CPL in hysteresis losses (HL) and eddy current losses (EDL) independently.
5. 3D FEM analysis by scripts using (92) to determine the HLs of the RC with the different core materials to confirm that the p_{CL} for the different materials has a constant value along the frequency range.

6. As the per-unit HLs are constants, it is possible that they were plotted versus per-unit loop hysteresis surfaces. This gives the opportunity to perform a mathematical equivalence between per-unit hysteresis losses and per-unit loop surfaces

7. A group of geometrical parameters from the core geometry and winding strategy are selected.

8. For each parameter selected in step 7, a parametrical 3D FEM analysis using the RC permuting only this parameter in each analysis. After each analysis series, the per-unit HLs are not depend on the frequency. This fact is the key for this research because the CPL are frequency dependent, however the per-unit losses are not. Therefore, a mathematical regression is developed by means of exponential equation using the per-unit parameter as the coefficient. The exponential is used for two reasons:

    a. the exponential equation gives the unit in DC, in concordance with the proposed method where the per-unit values for the RC correspond to the unit.

    b. one of the targets is the easiness of the equation to be used by power engineers for the optimization of the inductor. If another mathematical expression has been used, the final equation would have been more complex.

9. When a mathematical expression is obtained to determine the influence of each parameter independently, a final equation for estimate the HL can be used for the superposition theorem.

10. This equation is referenced for the RC in per-unit losses, so the final step is to link the equation obtained in step 9 with an equation of HL in function of frequency and this fact is possible because in step 5, the HL(f) was obtained from FEM.

11. The same steps from 5 to 10 have followed for ECL to propose the equation for ECL using (95).

12. The CPL for the component to be studied is the sum of HL (step 10) and ECL (step 11).

Any magnetic component could be studied by this method with the unique condition to select a RC according to the core of the inductor of interest. Additionally, the RC could have any winding strategy because the results will be obtained by normalisation and the coefficients of the equations will be referenced to the losses of the RC, but the final number for CPL will be the same independent of the RC selected for the study.

When the equation has been obtained, the power electronics engineer obtains the HL and ECL for the magnetic component independently achieving:

- The information of the HL and ECL, so the power engineers can make decisions easily for the optimization of the design.

- The final equation can be used repeatedly, so the optimization process is faster than the current methods to calculate the core losses.

4.6 Analysis for toroidal components

Following the previous explained method, the final equation for Toroidal components has been determined, thus, a RC for Toroidal components must be selected for the study.

A Toroidal component C107.65.25 (see dimensions in [26]) with 1 winding (4 turns with 1° of lateral distance) and 3C90 core material for HL study and the same component with 1 winding (3 turns with 1° of lateral distance) and a core made with 3F3 core material (Table 35) are selected for the ECL study.

In both cases, the winding disposition compels the use of a ·3D model because the magnetic field density is not axial symmetric (Figure 72) due to the winding strategy which produces the asymmetry in the magnetic field density. A 2D model does not have enough accuracy to determine $\vec{B}$, a 3D model needs to be precise in the core losses calculation by FEM (Figure 73).

Table 33 shows the dimensions of the Toroidal core for the RC and Table 34 contains the skin effect information for the wiring, AWG24 and AWG18, being relevant that the radius has been selected because the skin effect is the double of another.

(a)   (b)
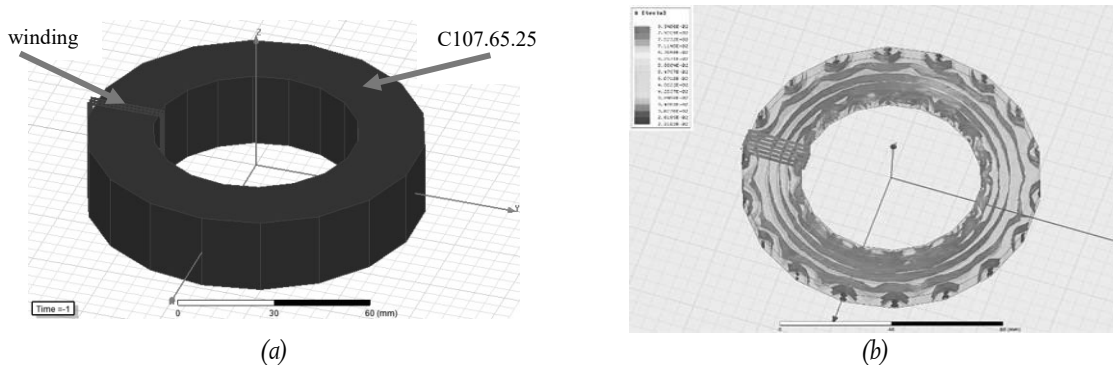
Figure 72. The Reference Component (RC) (a) Component in Pre-modeling (b) Results in result-processing.

Table 33 RC for Toroidal Core

Model	C. 107.65.25
Minor Radius (R)	43 mm
Main Radius (r)	64 mm
Height	25 mm
Width (R-r)	21 mm

Table 34 Skin Effect Information

KHz	δ	AWG24(r=1.02mm) r/δ	AWG18(r=0.510mm) r/δ
0.001	0.0236601	0.00379006	0.00738064
5.37	0.0003227	0.27789185	0.54115781
21.50	0.0001613	0.55582246	1.08239111
48.39	0.0001076	0.83373584	1.62359085
537.67	3.227E-05	2.77912005	5.41197063
1,209	2.151E-05	4.16868094	8.11795762
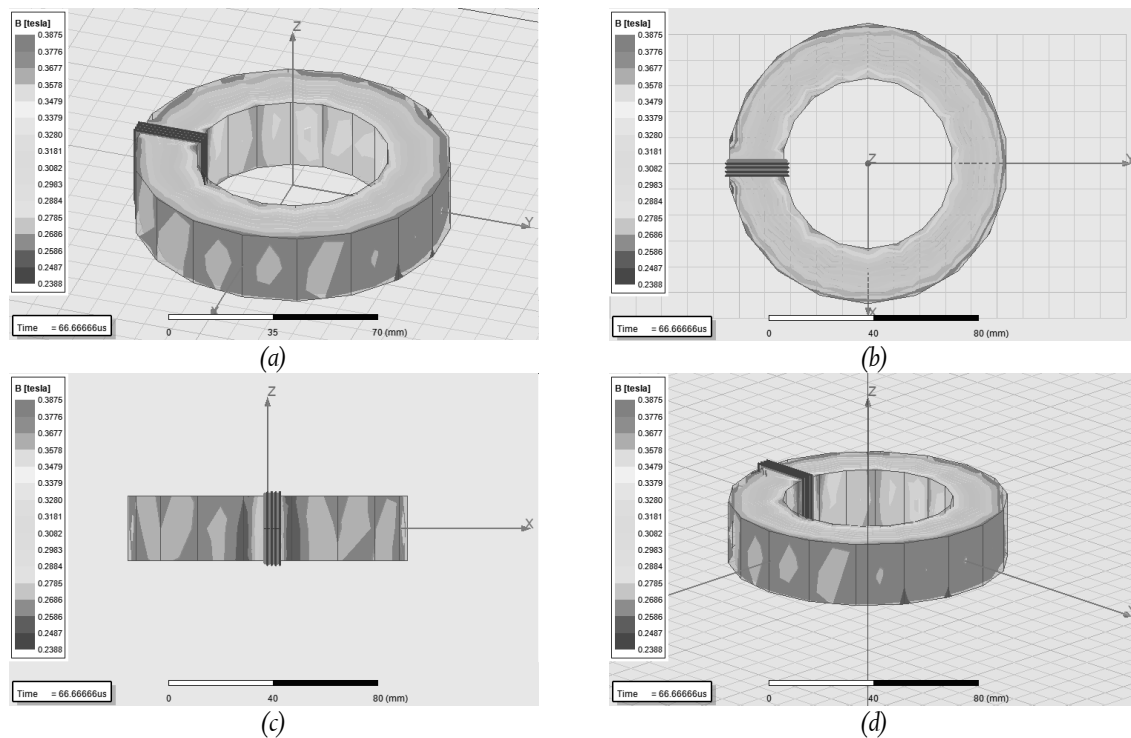
Figure 73. Toroidal Core Magnetic Field Density (a) Standard View (b) Top view (c) Lateral View (d) 3D view.

4.6.1 *Analysis of hysteresis losses*

The per-unit CPL has been used for the HL study using several analysis sequences. The analysis consists of a comparison of the HL defined previously between RC and other different components only varying a given parameter to investigate the parametric influence in the HL. The first parameter in the analysis sequence is the core material. See Table 35 that summarizes the materials used in the sequence, and their different permeabilities, coercivities and hysteresis loop areas, covering the range used in power electronics converters.

The results of the per-unit CPL (Table 36), varying the core material is plotted in Figure 74, giving that the per-unit CPL does not depend on the frequency for any of the analysed core materials.

Figure 75 demonstrates that HL is proportional to the hysteresis loop surface as the theory predicts (84), verifying that the scripts of the FEA tool have been properly used.

$$p_{HL} = \frac{P_{HL,i}}{P_{HL,RC}} = \frac{W_{HL,i}}{W_{HL,RC}} \qquad (98)$$

where S_i is the surface of the hysteresis cycle for the component "i" and S_{RC} is for the RC.

Table 35. Hysteresis Data for different materials

Code		Material	B(mT)	H(A/m)	μr	B_{max}(mT)	H_{max}(A/m)	W(mJ/m³)	p_{HL}
1		3F3	152	18	4000	410	250	429055,5	1.05
2		3C98	138	17	5000	450	275	426047,6	1.02
3		3C90	160	19	5500	435	250	423669,4	1.00
4		4A11	110	32	850	325	1000	43083,0	0.31
5		3F4	155	66	1700	407	1000	30928,1	0.18

Table 36. Per-unit Hysteresis p_{HL} (21) for different materials

Code	Frequency (kHz)					
	0.001	5	80	500	800	1000
1	1.05	1.05	1.06	1.09	1.10	1.10
2	1.02	1.02	1.02	1.01	1	1
3	1	1	1	1	1	1
4	0.32	0.32	0.32	0.34	0.37	0.37
5	0.18	0.18	0.18	0.20	0.21	0.21
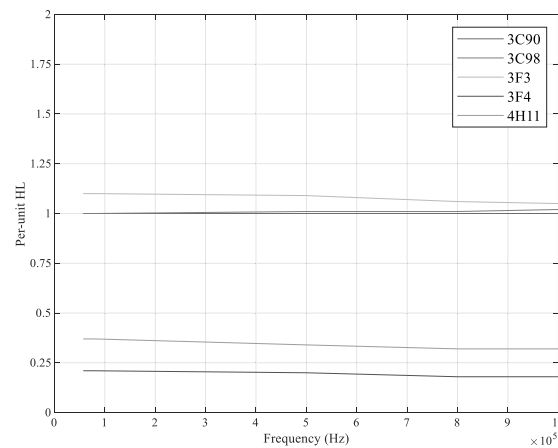
Figure 74. Relationship between frequency and Per-unit HL.
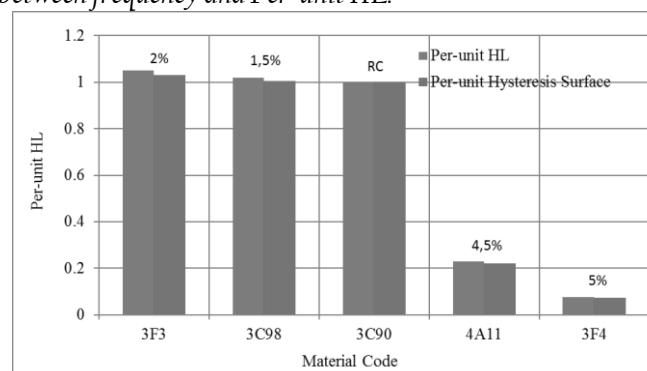
Figure 75. Per-unit hysteresis surface vs Per-unit HL.

The hysteresis loop areas were calculated from [77] with approximations using a polynomial regression. The small discrepancies with materials 4A11 and 3F4 are because their hysteresis loops are narrow and the polynomial approximations with a larger grade are needed (Appendix V).

The hysteresis loop data from [76] is for 25°C, but (98) is also valid for different temperatures. The loop area S_i for a different temperature can be calculated following the manufacturer instructions and the RC remains constant S_{RC} for 25°C and the CPL is calculated using (98) at the new temperature.

If the HL is plotted versus frequency, the power trendlines are similar except for the exponent. (Figure 76). Thus, there is a relationship between $P_{HL,i}$ and frequency that could be represented mathematically with an exponent according to the core material of the magnetic component.
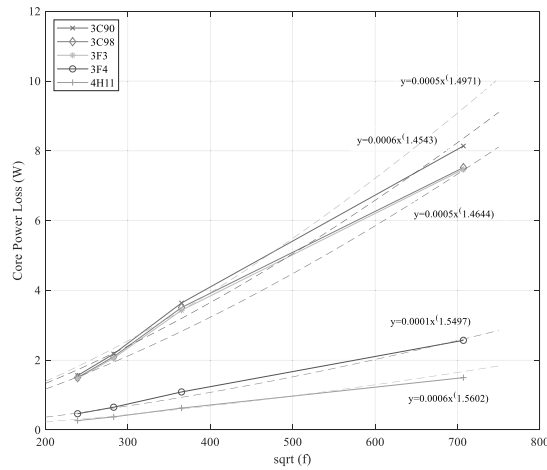
Figure 76. Relationship between frequency and power core losses (HL) per material.

The equation (99) defines the HL with the parameters obtained in the first analysis sequence. These data have been obtained using the RC (Table 35). If another RC would have been used, the relationships and conclusions would have been similar, however for the RC used, the power HL is given by:

$$P_{HL,i}(f) = P_{HL,i} \cdot f^{e^{\frac{0.0691}{S_{RC}} \cdot S_i + 0.7926}} \tag{99}$$

where $P_{HL,i}$ is the HL at 0 Hz, S_{RC} is the surface of the hysteresis cycle for the RC and the S_i is the hysteresis cycle for other material in this work.

4.6.1.1 Core volume influence

The core volume is calculated following equation (100) for Toroidal Cores and the volume can be modified through height, width and radius independently (Figure 77).

$$v = 2 \cdot \pi \cdot R_m \cdot A_c \tag{100}$$
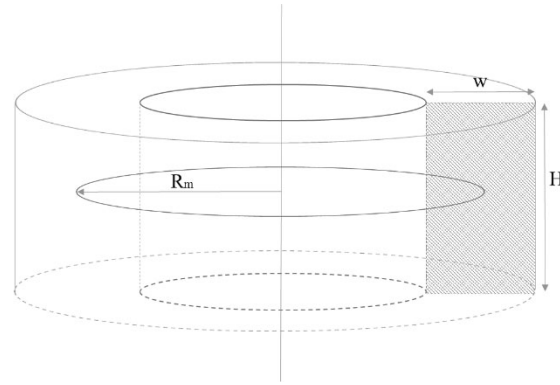
Figure 77. Volume for a Toroidal component.

Table 37 Volume variations from core height

Core Height(mm)	25 (RC)	24	23	22
Volume (mm³)	17.647	16.942	16.2361	15.5301

Table 38 Volume variations from core width

Width(mm)	21 (RC)	20	19	18
Volume (mm³)	17.6479	16.807	15.961	15.1268

Table 39 Per-unit HL vs Volume

	Frequency (kHz)			
Volume (mm³)	500	133.33	80	57.14
17.647	1	1	1	1
16.942	0.98	0.97	0.97	0.97
17.6479	0.97	0.97	0.97	0.97
16.2361	0.94	0.93	0.93	0.93
15.5301	0.89	0.90	0.90	0.90
15.961	0.91	0.91	0.91	0.91
15.1268	0.87	0.87	0.87	0.86

where R_m is the average radius of the Toroidal core and A_c is the surface area of the cross section ($A_c = w \cdot H$) shown in Figure 77. According to our work, this step consists of determining the influence of the parameter and the Core Volume, only varying the height or the width (Figure 78 (a)). The permutations have been described in tables Table 37, Table 38 and Table 39. As the per-unit HL is not dependent of the frequency, Figure 78 (b) is plotted giving the relationship between Per-unit HL and the per-unit Volume defined by (101).

$$\frac{P_{HL,i}}{P_{HL,RC}} = \frac{v_i}{v_{RC}} = \frac{2 \cdot \pi \cdot R_m \cdot A_i}{2 \cdot \pi \cdot R_m \cdot A_{RC}} = \frac{w_i \cdot H_i}{w_{RC} \cdot H_{RC}} \qquad (101)$$

Where v_i is the volume of the Toroidal Core for component i and V_{RC} is the volume for the RC. Another sequence consists on the main radius permutation for the Toroidal Core component having a constant cross-section (Table 39). Equations (102) and (103) define the results

showed in Figure 79 where there are two different scenarios (non-saturation state and saturation state).

$$\frac{P_{HL,i}}{P_{HL,RC}} = \left(\frac{2 \cdot \pi \cdot R_i \cdot A_{RC}}{2 \cdot \pi \cdot R_{RC} \cdot A_{RC}}\right)^{-1.7} = \left(\frac{R_i}{R_{RC}}\right)^{-1.7} \tag{102}$$

$$\frac{B_i}{B_{Sat}} \geq 1 \rightarrow \frac{P_{HL,i}}{P_{HL,RC}} = \left(\frac{2 \cdot \pi \cdot R_i \cdot A_{RC}}{2 \cdot \pi \cdot R_{RC} \cdot A_{RC}}\right)^{-2.95} = \left(\frac{R_i}{R_{RC}}\right)^{-2.6} \tag{103}$$

The first one, when the core is not saturated, the correlation follows (102). The second one, when the core is in saturation ($B_i \geq B_{Sat}$) is according to (103). Then, the Per-unit HL in the range ($0.9 < v_i/v_{RC} < 1.1$) is similar with core saturation and non-saturation. The exponents used were obtained from mathematical regressions.

(a)   *(b)*
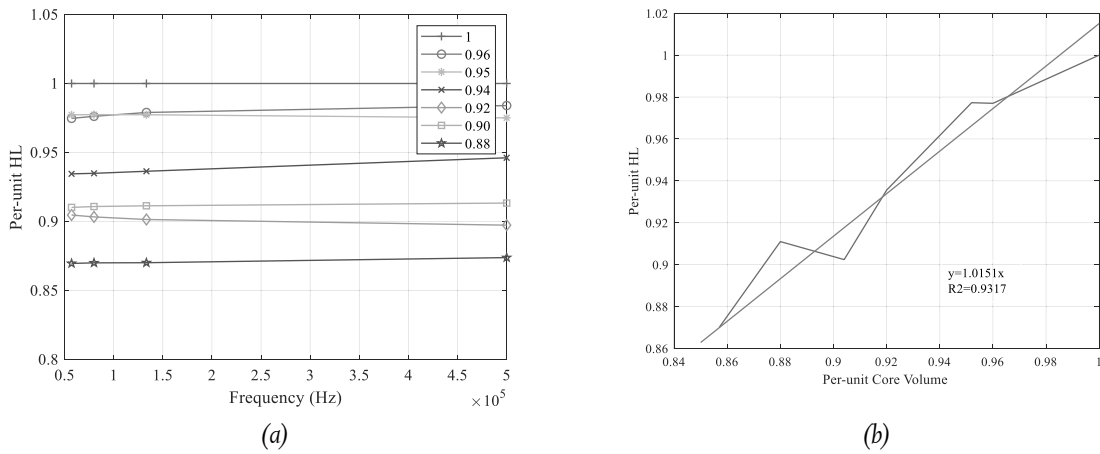
Figure 78. Relationship between Per-unit and Core Volume Per-unit HL vs Frequency (b) Per-unit HL vs Per-unit Volume.
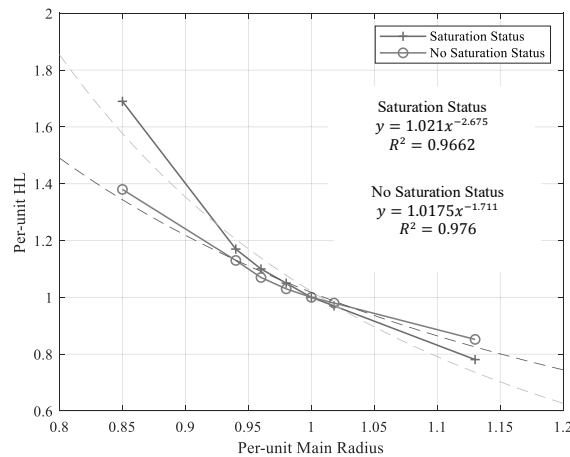
Figure 79. Relationship between Per-unit HL vs Per-unit Volume modifying the Main Radius.

Table 40 Per-unit HL vs Volume modifying the Main Radius

Main Radius(mm)	50	45	43*	42	41	40	35
Volume (mm³)	19.955	17.97	17.647	17.318	16.988	16.658	15.009

4.6.1.2 **Coil parametrical analysis**

4.6.1.2.1 Winding current influence

In this study, the Per-unit HL are constant in the practical current range for the components used in power electronics. If the current is in this range, the Per-unit HL is not dependent of the frequency and, it is possible to establish a relationship between the per-unit HL and per-unit current (Figure 80).

$$\frac{P_{HL,i}}{P_{HL,RC}} \sim \left(\frac{I_i}{I_{RC}}\right)^{2.95} \tag{104}$$

where I_i is the current for the component "i" and I_{RC} is the current for the RC. In theory, with the FEA tool, it is able to determine the case when the current is outside of the regular winding current values (probably with the core in saturation), then, the relationship follows:

$$\frac{B_i}{B_{Sat}} \geq 1 \rightarrow \frac{P_{HL,i}}{P_{HL,RC}} = 0.0002 \cdot f + \left(\frac{I_i}{I_{RC}}\right)^{2.95} \cdot \left(\frac{S_i}{S_{RC}}\right)^{\frac{1}{2}} \tag{105}$$

These assumptions have been checked with other materials, different winding geometries and configurations in addition to these ones. As in the previous sequences, the exponents have been obtained from mathematical regressions (Appendix VI).

4.6.1.2.2 Turn number influence

This analysis sequence modifies the number of turns in the winding (The RC has 4 turns). The same geometrical parameters for the windings were applied. The effects from the winding geometrical configuration are analysed further in next analyses sequences. As other sequences, the Per-unit HL is uniform during the frequency range and this consequence allows us to give the following relationship if the per-unit HL increase is compared with the increase of the number of the turns (Figure 81):
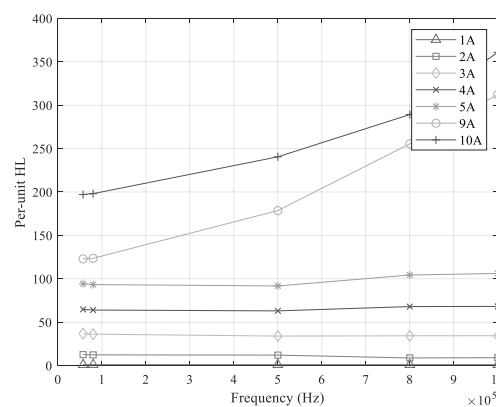
Figure 80. Relationship between Per-unit HL vs Frequency for different currents flowing through the windings.
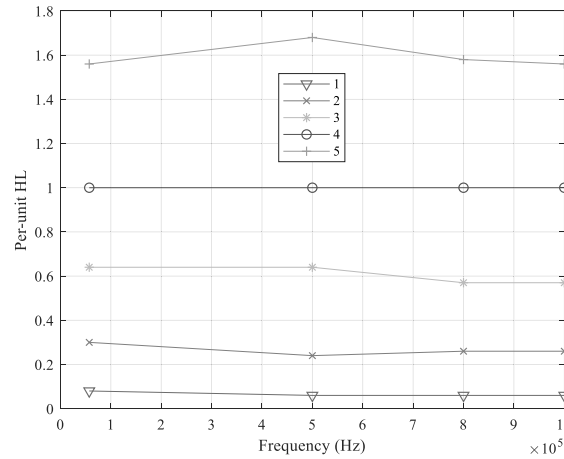
Figure 81. Relationship between Per-unit HL vs Frequency for different number of turns.

$$\frac{P_{HL,i}}{P_{HL,RC}} = 0.06 \cdot \left(\frac{n_i}{n_{RC}}\right)^2 \tag{106}$$

where n_i is the number of turns for the component i and n_{RC} is the number of turns for the RC.

4.6.1.2.3 Multiple windings

These analyses have been developed based on the RC (inductive component with only one winding), however there are inductors in the market with several windings and there are toroidal components working as a transformer. These potential cases have been studied in this section. In order to develop this analysis, an additional winding is added to the RC.

The additional winding has 4 turns (diameter AWG18) with the same lateral distance as the former winding (diameter AWG24). AWG18 has been chosen because the skin effect is double that of AWG24. The simulation under FEA was performed under open circuit condition. Thus, the component works as an inductive component, however, the effect of copper wiring around the winding that is working could be analysed in this sequence. Figure 82 shows the studied configurations (the diameters in the different cases have been modified as well as for other sequences). The relationship between the Per-unit HL and the frequency is defined for the three cases (inductive component, only current from the 1° winding and only current from the 2° winding). The influence of having copper wires without current is negligible from the core losses point of view. The sway of the winding configuration in the HL is about 5% compared with material, volume and other parameters (Figure 83), so the per-unit HL is able to define by (107) that means that there is no additional effect to include not used copper in the model.

$$\frac{P_{HL,i}}{P_{HL,RC}} = 1 \cdot f^{0.0035} \approx 1 \tag{107}$$

(a)   *(b)*   *(c)*
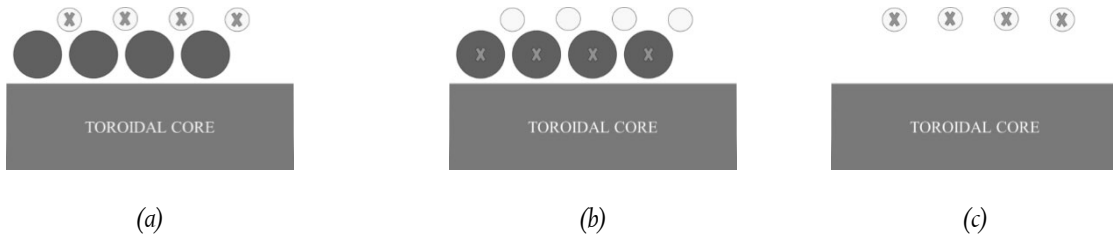
Figure 82. Analysed windings' configurations.
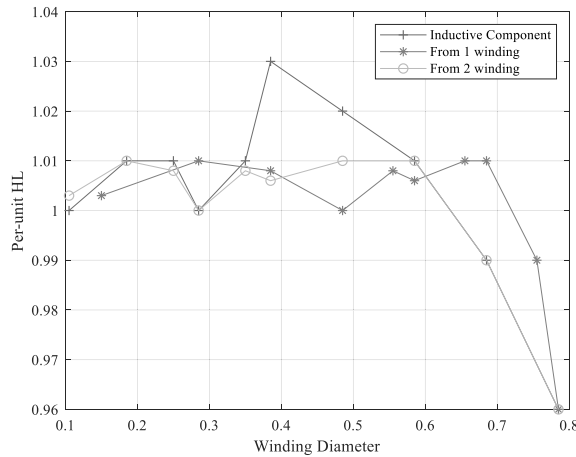
Figure 83. Per-unit HL for multiple windings.

4.6.1.2.4   Winding configuration

Another important set of analyses sequences were studied for other possible winding configurations. The winding cross-section size has an impact on the HL in the case that the diameter of the inductive components is very large. This is due to the fact that some magnetic field density is spread into the wires instead of the core. Nevertheless, the effect is negligible for diameters used for regular manufactured magnetic components. In addition, if the diameter is less than 2.4 times the d_l (RC), this effect is non-existent. The winding position at the Toroidal Core is expected not to have any effect in the HL (Figure 84). The lateral distance between windings has a minimal effect to take account (the analysis have been developed with a constant lateral distance between turns in the winding) being the effect ruled by (108).

$$\frac{P_{HL,i}}{P_{HL,RC}} = e^{-0.004 \cdot \alpha} \tag{108}$$

where α means the angle in degrees between windings (Figure 84).

| (a) | (b) | (c) |
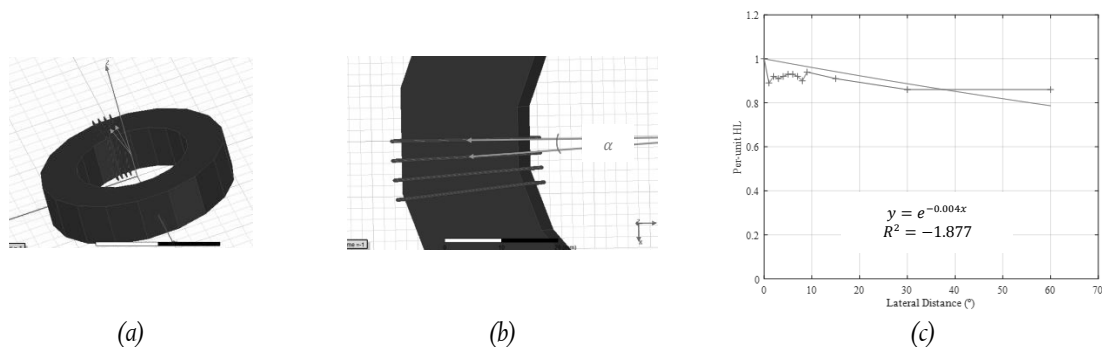
Figure 84. (a) Global View (b) Definion of α (c) Per-unit HL vs Lateral Distance (°).
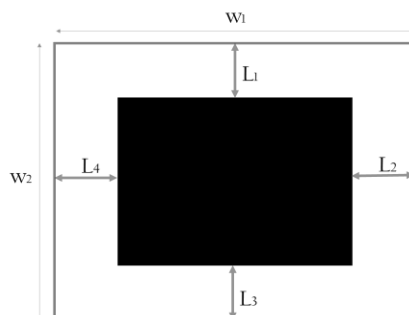
Figure 85. Winding Configuration.

Table 41. Per-unit HL changing the winding geometry

$f(kHz)$	Per-unit vertical distance (23)									
	1,00	1,03	1,05	1,10	1,13	1,17	1,21	1,28	1,7	3,37
5.7	1,00	1,01	1,01	1,01	0,99	1,03	1,02	1,01	1,0	1,02
80	1,00	1,01	1,01	1,01	0,99	1,03	1,02	1,01	1,0	1,02
133.3	1,00	1,01	1,01	1,01	0,99	1,03	1,02	1,01	1,0	1,02
500	1,00	1,02	0,99	1,00	0,98	1,01	1,00	1,00	0,9	1,00
AVERAGE	1,00	1,01	1,01	1,01	0,99	1,03	1,02	1,01	1,0	1,02

Table 42. Per-unit HL changing the winding geometry with different diameters

Radius	$L_1+L_3=L_2+L_4$				
	1.60	2.00	2.20	2.60	3.00
0.285	1.00	1.00	0.98	1.00	0.99
0.385	0.99	1.01	1.00	1.02	1.00
0.485	1.00	0.98	1.00	0.97	0.99

Figure 85 shows a lateral view of the winding, where the black item is the toroidal core, the red line is the turn position, and where L_1, L_2, L_3 and L_4 are the distances between the winding edge and the toroidal core. w_1 and w_2 are the turn edge dimensions for this example. In the market, the manufacturers build the inductors using the same distances for L and w, but FEA is able to use different measurements for L_1, L_2, L_3 and L_4 as well as w_1 and w_2. So, the 4 lateral distances for the winding configuration (vertical or horizontal between the turn edges and the core, Figure 85) could be modified independently with different values in the same winding.

An important conclusion of this analysis sequence is that the Per-unit HL is similar if the sum of the vertical distances (L_1+L_3) has the same value for all potential configurations. A similar conclusion is achieved for horizontal distances (L_2+L_4). The results of the per-unit HL are indicated in Table 41 according to the frequency.

This conclusion is due to the fact that the magnetic field density does not suffer a significant variation inside the core. Table 42 summarizes the per-unit HL results for similar analysis sequences with different coil diameters showing that they are very similar.

In summary, the winding configuration for Toroidal components has not impact on the HL. The main factors are the core material, core volume, the coil current and number of turns in the windings.

4.6.1.3 Hysteresis losses equation

The determination of the mathematical influence of various parameter on HL has been analysed by means of parametrical analyses. This analysis is based on 3D FEM isolating the specific parameter in the sequences. Thus, the relationship between $P_{HL,i}$ and $P_{HL,RC}$ per each involved parameter has been established by mathematical regressions after checking that Per-unit analysis does not depend on frequency. Since the influence of each parameter has been separately determined, the magnetic field density with FEM tool, it is possible to add every influence in only one equation where the correlations obtained from the per-unit method allows defining an algorithm to estimate the HL for Toroidal Components.

For non-saturated inductive components, with a constant lateral distance between windings, the hysteresis losses can be defined using (109) and (110).

$$P_{HL,i} = \left(\frac{0.05}{2} \cdot e^{-0.0004 \cdot \alpha} \right) \cdot \left(n_i^2 \right) \cdot \left(I_i^{2.95} \right) \cdot v \qquad (109)$$

$$P_{HL}(f) = P_{HL,i} \cdot f^{\frac{0.0691}{S_{RC}} \cdot S_i + 0.7926} \qquad (110)$$

$P_{HL,i}$ is the HL of the inductive component, α is the angle between turns (degree) in the winding, n is the number of the turns, I is the winding current and v is core volume.

The previous equations are only valid for inductors with one winding. In the case where the magnetic component has more than one winding, applying the superposition theorem, equations (111) and (112) are obtained to determine HL.

The superposition theorem can be applied to magnetic fields and current but it is not applied to energies or losses because of non-linarites. From a current perspective, the main non-linear part of a magnetic component is the core. However, in this case, the theorem for the magnetic

field, based on [9], is used for toroidal components in non-saturation state and per winding.

$$P_{HL,i} = \left(\sum_j \frac{0.05}{2} \cdot e^{0.0004 \cdot \alpha_j}\right) \cdot \left(\sum_j (n_j^2) \cdot (I_j^{2.95})\right) \cdot v \tag{111}$$

$$P_{HL,i}(f) = P_{HL,i} \cdot f^{\frac{0.0691}{S_{RC}} \cdot S_i + 0.7926} \tag{112}$$

where j is the winding of the magnetic component i in the sum.

In the case of core saturation, the correlations defined in the previous analyses sequences allow defining a mathematical algorithm to estimate the hysteresis core losses. This approach is the same as the case without saturation, but taking into account (103) and (105) in the process.

4.6.2 Analysis of Eddy current losses

To estimate the ECL, several analysis sequences have been launched using the per-unit methodology with each parameter being similar than in the HL analysis.

The only difference in this study is that the RC has been modified, with this study using a Toroidal Component C107.65.25 with 1 winding (3 turns with 1° of lateral distance) made with 3F3 core material to consolidate the posterior validation using different material to confirm the not impact of RC selection.

The first analysis done in the HL was the influence of the material, to confirm if the Per-unit Method is available. In ECL case, it needs a similar confirmation for the Per-unit ECL to demonstrate that does not depend on the frequency. The modification of the RC allows confirming that the conclusions will be similar with different a RC.

The first parameter for the analysis sequences is the core material (Table 43).

Table 43. Data of the different materials used in the core

Code		Material	B(mT)	H(A/m)	μ_r	B_{max} (mT)	H_{max} (A/m)	$\sigma(1/\rho)(\Omega m)$
1		3F3	152	18	4000	410	250	0,50000
2		3C98	138	17	5000	450	275	0,10000
3		3C90	160	18,5	5500	435	250	0,10000
4		3F4	155	66	1700	407	1000	0,10000
5		4A11	110	32	850	325	1000	0,00001
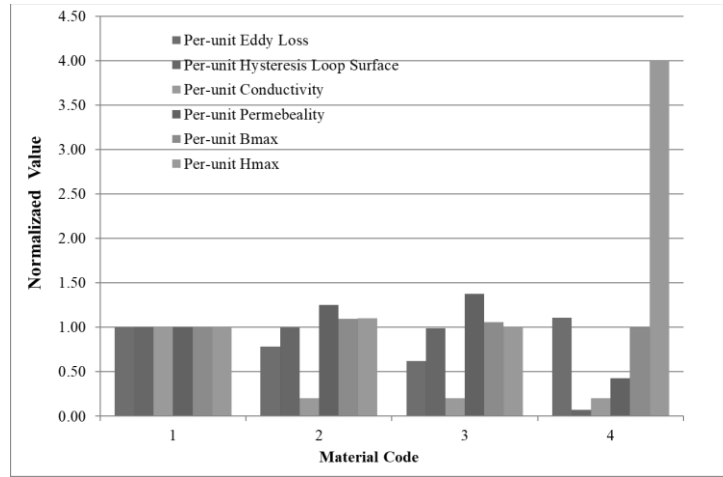
Figure 86. Per-unit Values vs Material.
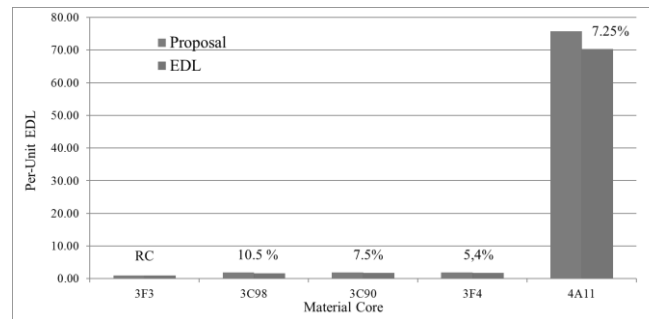
Figure 87. Per-unit ECL vs Material Code.

Table 43 shows the material data for the cores used in the analysis. The results of the Per-unit ECL modifying the material have been plotted in Figure 86 versus different characteristics showing that there is a clear relation between the conductivity and the per-unit ECL while there is not a defined correlation with other parameters.

The equation (112) has been proposed to find a correlation between the per-unit ECL and other equivalent values. This result was obtained by focusing on achieving a good enough and quick approximation (Figure 87) with an accuracy lower than 5% in most of the cases. It is however very complex to obtain an equation for a range of materials because the nature of the eddy currents is material specific. As such, we have continued with this proposal because it is valid (-10%) for all of the materials analysed, and it is very fast to obtain the values from the core manufacturer sheet. The ease of determining these parameters gives the equation an advantage over other more accurate equations.

$$\frac{P_{ECL,i}}{P_{ECL,RC}} = \left(\frac{H_{max_i}}{H_{max_{RC}}}\right)^{0.01} \cdot \left(\frac{\sigma_i}{\sigma_{RC}}\right)^{-0.4} \tag{113}$$

where σ_i is the conductivity of the material i and σ_{RC} is the conductivity for the RC.

4.6.2.1 **Core volume influence**

As explained in the section II, the ECL is divided into internal core losses and the more significant component surfaces losses.

Moreover, the ECL inside the component are insignificant compared to the surfaces losses. Thus, it will only be necessary to run the volume modification sequence for one of the dimensions because the eddy current for the boundary losses are proportional to the boundaries surfaces. The per-unit ECL (for core volume) is invariable during the frequency range as usual in this research for the Per-unit ECL (Figure 88). The per-unit ECL has been plotted versus the Per-unit volume, in Figure 89. Eq. (114) defines the correlation between them.

$$\frac{P_{ECL,i}}{P_{ECL,RC}} \sim \left(\frac{v_i}{v_{RC}}\right)^{1.05} \tag{114}$$

If other analysis sequences to modify the core volume would have developed like in the HL analysis, the same conclusion would have been achieved. The nature of the HL is different than ECL because the HL is linked to the hysteresis loop surface area and the ECL is linked to the component surface area. This assumption is valid not only for Toroidal components; but it can be generalized for any magnetic component in power electronics.
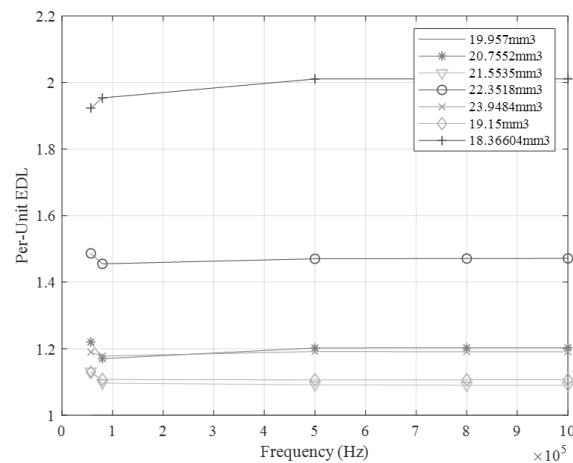
Figure 88. Per-unit ECL vs Frequency for different Core Volumes (in mm³).
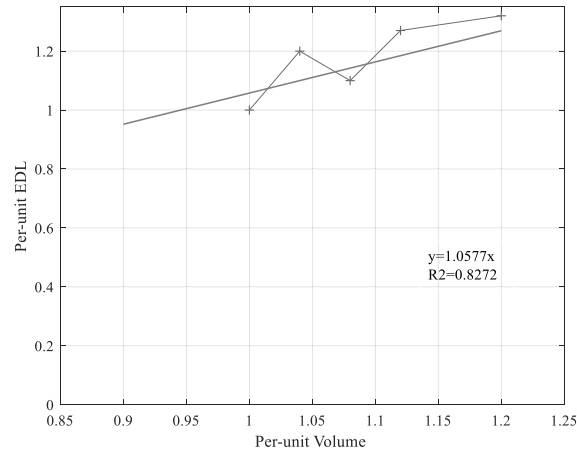
Figure 89. Per-unit ECL vs Per-unit Core Volume.

4.6.2.2 Winding current influence

Following the same process used to obtain for the HL, the influence of winding current and turns number parameters are analysed by running sequences. The p*er-unit ECL* is constant with the frequency in both sequences again. Figure 90 corresponds to the coil current series and Figure 91 conforms to the winding number series obtaining the following relationships:

$$\frac{P_{ECL,i}}{P_{ECL,RC}} \sim \frac{1}{2} \cdot \left(\frac{I_i}{I_{RC}}\right)^{1.2} \tag{115}$$

$$\frac{P_{ECL,i}}{P_{ECL,RC}} = 1.18 \cdot \left(\frac{n_i}{n_{RC}}\right)^{1.8} \tag{116}$$
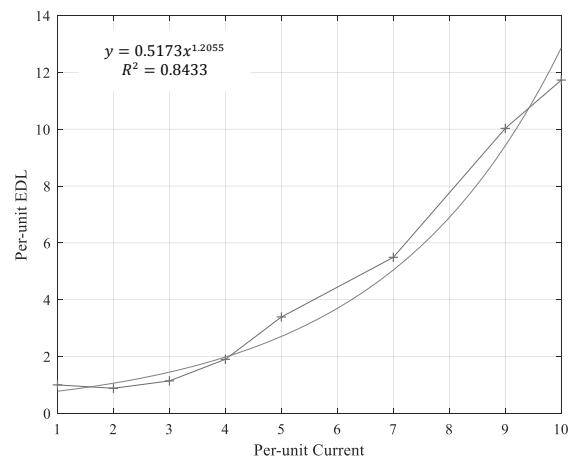
Figure 90. Per-unit ECL vs Per-unit Current.

$$y = 1.177x^{1.8361}$$
$$R^2 = 0.9647$$
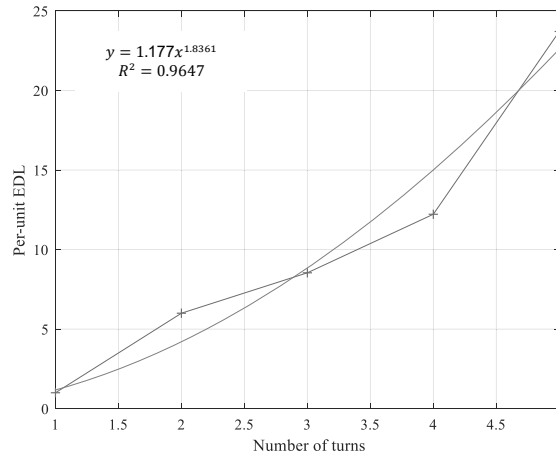
Figure 91. Per-unit ECL vs turn number.

4.6.2.3 Winding position influence

The lateral distance between windings sequence performed considers the same lateral distance between them, this being the general assumption in the manufacturing design.

In this sequence, several lateral distances were checked, the *Per-unit ECL* has a permanent value during the frequency range analysed. There are several configurations which are not usual for power converters, but they are analysed by FEA to achieve a mathematical correlation.

The main factor that impacts for the ECL are the current loops created due to the magnetic field. The winding position, as expected, does not modify the magnetic field inside the core significantly, in consequence, the value of the per-unit ECL is not influenced by this parameter modification. Even the correlation, it is equal to the HL analysis (Figure 92):

$$\frac{P_{ECL,i}}{P_{ECLRC}} = e^{-0.004 \cdot \alpha} \tag{117}$$

$$y = e^{-0.0004x}$$
$$R^2 = 0.95$$
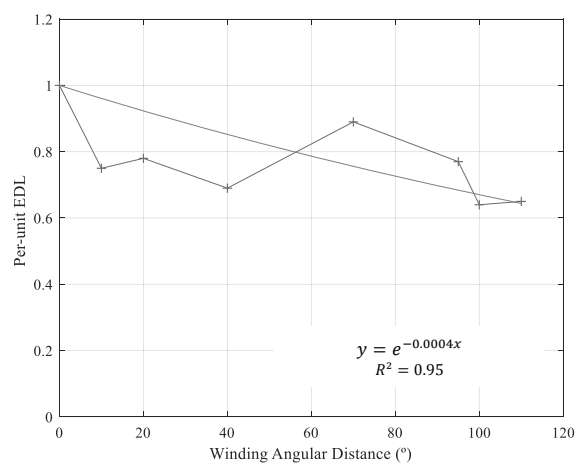
Figure 92. Per-unit ECL vs. winding lateral distance.

4.6.2.4 **Eddy current losses equation**

The relationship between $P_{ECL,i}$ and $P_{ECL,RC\,for}$ each involved parameter has been analysed, as the HL analysis was performed, obtaining an equation to estimate the ECL for Toroidal Components using the known effect of each parameter. Following the same considerations for the HL and using the superposition theorem with the same limitations.

Considering a constant lateral distance between windings and non-saturation status, the eddy current losses can be defined as:

$$P_{ECL,i} = (13.15 \cdot e^{-0.0004 \cdot \alpha}) \cdot (n_i^{1.8}) \cdot (I_i^{1.2}) \cdot v \tag{118}$$

$$P_{ECL}(f) = P_{ECL,i} \cdot f^{0.18\left(\frac{Hmax_i}{Hmax_{RC}}\right)^{0.01} \cdot \left(\frac{\sigma_i}{\sigma_{RC}}\right)^{-0.4} + 0.1138} \tag{119}$$

where $P_{ECL,i}$ the EDL of the inductive component, α is the angle between turns (degree) in the winding, n is the number of the turns, I is the winding current and v is core volume.

The superposition theorem is used similarly to the HL analysis; this theorem is able to apply to magnetic fields and current densities [9]. Thus, if the Toroidal core component has more than one winding, the ECL are defined as:

$$P_{ECL,i} = \left(\sum_j 13.15 \cdot e^{0.0004 \cdot \alpha_j}\right) \cdot \left(\sum_j (n_j^{1.8}) \cdot (I_j^{1.5})\right) \cdot v \tag{120}$$

$$P_{ECL}(f) = P_{ECL,i} \cdot f^{0.18\left(\frac{Hmax_i}{Hmax_{RC}}\right)^{0.01} \cdot \left(\frac{\sigma_i}{\sigma_{RC}}\right)^{-0.4} + 0.1138} \tag{121}$$

Where j is the winding of the magnetic component and i is in the sum.

In the case of core saturation, the correlations defined in the previous analyses sequences allow defining a mathematical algorithm to estimate the hysteresis core losses. This is the same method defined for the case without saturation, but using the same equations as in HL.

4.7 Validation of the obtained core losses equation

Component I (Table 44) core losses were obtained with the proposed methodology using (111) and (120). The results were compared with:

a. the experimental measurements made in [111],

b. an analytical assessment different from the Steinmetz equation presented in [112], and

c. the CPL of Component I calculated with Ansys Maxwell using the scripts where the actual material was simulated and a total of 435635 FE were used.

Our results are in good agreement with the experimental results [111] for 400 to 700 kHz as shown in Figure 93. The results from 100 to 300 kHz match the mathematical results from [112]

in an acceptable way. Finally, differences between the simulations and the proposed equations (99) and (108) are under 5%.

The analysis of Component II has been done using Ansys PExprt [113] (Table 45) and compared with the results obtained using the proposed expressions. As shown in Figure 94 the results obtained using the proposed equations (99) and (108) agree with the results obtained from Ansys PExprt. It is important to note that the core material is not in the list included in Table 35 and Table 43 used to obtain our equations (Table 44 shows the material features for 3C92). For the Component II, Ansys PExprt has been used instead of Ansys Maxwell to globalize the results for other FEMs. This tool is used as Maxwell for analysis of multi-winding transformers, inductors and flyback components. Additionally, this tool is able to optimize the design determining the core size, shape and air-gap and winding strategy for a given power converter topology.

Table 44. Data of 3C92 (Component II)

Code		Material	B(mT)	H(A/m)	μ_r	B_{max}(mT)	H_{max}(A/m)	W(mJ/m³)	p_{HL}
1		3F3	152	18	4000	410	250	429055.5	1.05
2		3C98	138	17	5000	450	275	426047.6	1.02
3		3C90	160	19	5500	435	250	423669.4	1.00
4		4A11	110	32	850	325	1000	43083.0	0.31
5		3F4	155	66	1700	407	1000	30928.1	0.18
		3C92	143	18.5	5000	475	250	213616.92	0.51

Table 45. Component data I

VALIDATION COMPONENT I (using ANSYS)			
Core	Denomination	C107.65.25	
	Material	3F3	
Winding	Turns	3	
	Winding Configuration	Lateral distance 4°	
	Winding Current (A)	1	
	Winding Conductor Material	Copper	
	Winding Conductor gauge	AWG18	
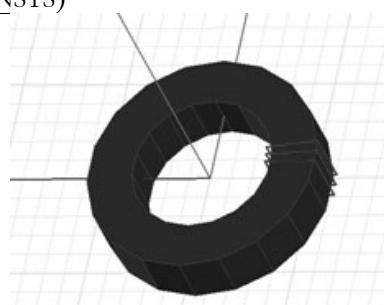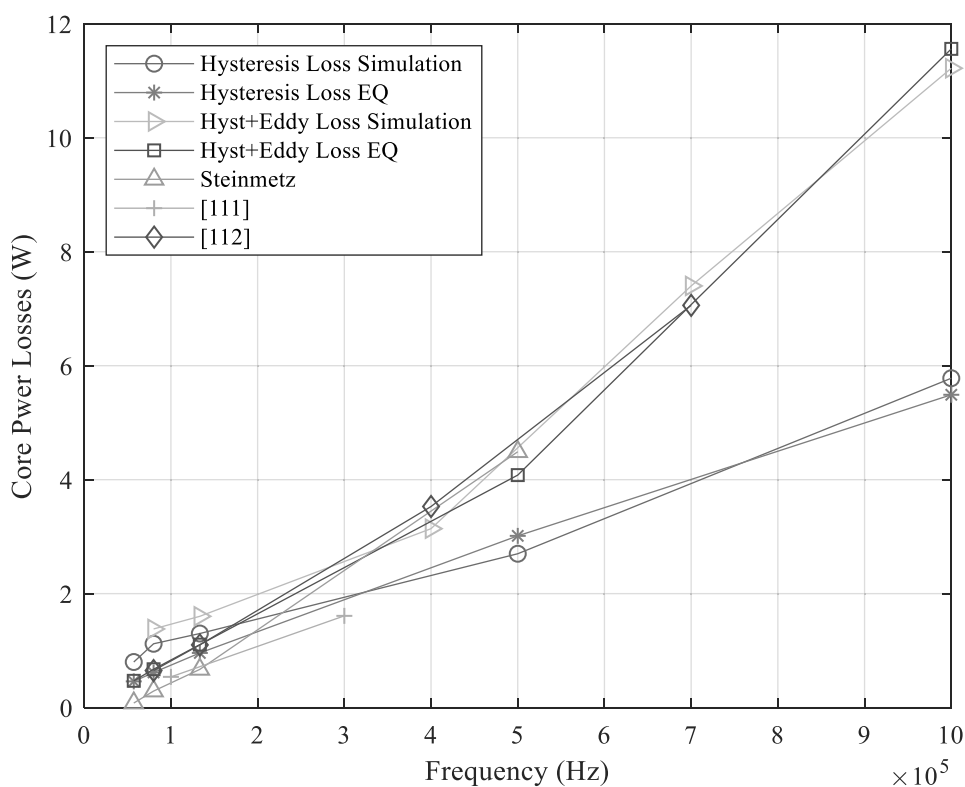
Figure 93. FEM and experimental values for the Component I.

Component I has been modelled in Ansys Maxwell with a 3D model because the winding strategy produces an inaccurate result using 2D modeling methods. As it was explained at the beginning of the chapter, the current CPL calculations are only valid in limited frequency range and the benchmarking has been developed using methods which are accurate in a variety of ranges. The results obtained from the equations confirming that this proposed method is a good approach.

Table 46. Component data II

VALIDATION COMPONENT II (using PExprt)		
Core	Denomination	TX.10/6/4
	Material	3C92
Winding	Turns	5
	Winding Configuration	Lateral distance 72°
	Winding Current (A)	1
	Winding Conductor Material	Copper
	Winding Conductor gauge	AWG13
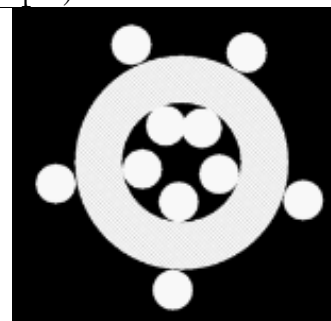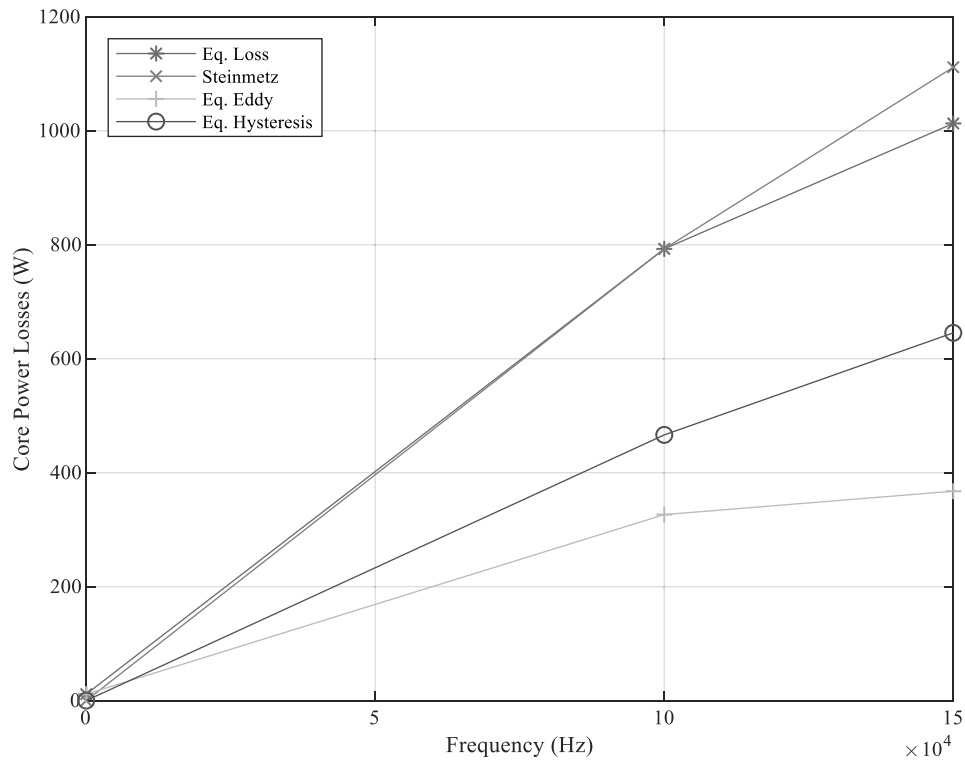
Figure 94. FEM and experimental values for the Component II.

The component II has been validated with PExprt where the Steinmetz equation is used for the CPL determination, this is the reason for the frequency range used for this validation. As it is said this validation is very useful because the material core is outside of the material list used on the methodology demonstrated that all material can be used with the proposed method as well as other FEMs

5 Conclusion and next steps

The optimization of a power converters depends on the different interdisciplinary constrains such as the product cost and energy efficiency imposed by the market and the dimension (weight and volume) requirements. Some of this constraints are closely related with the magnetic components inside the power converters, due to losses that have on the required volume due to the thermal conditions to survive in the environment. However, the main requisite for the magnetic component is the efficiency given by the electrical parameters. This is the reason which there are several equivalent circuits in the art to determine these parameters being more and more important to predict the power losses of the inductive component, factor that could be limit even the capabilities operations of the power converter. The FEM was introduced in the electrical and electronic engineering to earn precision in these parameter calculations, nevertheless some 3D models are needed because there are some high frequency effects that cannot be analyzed with 2D models and the magnetic field distributions due to the core geometries and/or winding strategies are asymmetric. Currently, the computer limitations do not to allow simulating complex magnetic components in 3D or the needed CPU time is not operative for the design engineers for an optimization process.

Thus, the accuracy to determine the losses of the magnetic component is crucial for the design as well as the CPU time to be operative for the optimization process. Then, a 3D equivalent model based on 3D FEM is interesting if the FEA is quick and accurate.

5.1 Major contributions

As it has been explained in the thesis, the power losses determination is a complex task divided in the calculation of the winding losses and the core losses of a magnetic component. Thence, the first major contribution is equivalent circuit based on energies validated for 3D FEM models where an original method to simplify the component in the FEM process

achieving more than 95% CPU time saved and obtaining the electrical parameters as the winding resistance and inductance with similar accuracy by material adjustments in the FEM and the novel correction factor which has been split in two terms according to the skin and the proximity effects.

This contribution has been validated experimentally with an error about 5% for any magnetic component from 1 kHz to 1 GHz being the only limitation that the core has to be in non-saturation because the superposition theorem was used being not an issue because it is the regular state in operation conditions for the power converters.

The core losses determination is another complex hard for the power engineers being fundamental the determination of the magnetic field density in the core, thus, a precise magnetic field density map of the core is imperative to obtain an accurate value of the losses.

An original method using 3D FEM has been proposed in this work by the pioneer per-unit method allowing analysing the influence of each parameter in the losses of the core.

This new methodology gives the process to analyse the hysteresis and eddy current losses separately giving a final equation for each kind of core. This methodology has been used for Toroidal Components because these ones are very common in power electronics and the determination of the losses need of a 3D FEM model because of the winding strategy defining the core power losses for Toroidal components without needing any magnetic field calculation, only material data from the manufacturer sheet and the geometry of the winding strategy.

5.2 Minor contributions

In the process to achieve the major contributions of this thesis, other minor contributions for the art have been obtained as:

- The computer limitations definition that have been explained to understand the reasons to be able to use FEM in 3D or 2D depending of the symmetric of the magnetic component and the simplifications could be used for reducing the computing time when analyzing the magnetic field produced in the magnetic component. Also it has been described the relationship between the computer capacity and the FEs used in the software simulation.

- A quality electromagnetic analysis been performed to the magnetic component in this thesis to have an accuracy magnetic field produced into and outside of the magnetic component and the windings. It has been presented the incidence of geometrical variations of the magnetic component for resistance, inductance and core losses for the inductive component by parametrical analyses.

5.3 Next Steps

The next research line of this work will be to improve and spread the per-unit method to other magnetic components with different cores to define the equation for the power losses.

An original idea to spread this new 3D model for other magnetic components would be to identify a geometrical coefficient in the presented equations depending of the core geometry. This will mean that depending of the magnetic component was analysed, the geometrical coefficient was used in the same equations and procedures presented in this thesis.

Furthermore, this model could be used for any magnetic component to reduce the simulation times and saving money for the design engineers in power electronics.

Another advantage of this proposal would be that we could use this model to test new 1D/2D models for other magnetic components without using testing or 3D real simulations.

6 Publications and Activities

Description of the activities, seminars and publications developed in this Doctoral Thesis.

6.1 Publications

- JOURNAL PUBLICATIONS

		JCR	SCOPUS
Paper-A	**J. R. González-Teodoro**, E. Romero-Cadaval, R. Asensi. "Review of Core Power Loss Analysis Using Finite Element Methods", Int J Magnetics Electromagnetism, vol. 5, Issue. 2. (16/10/2019) doi: /10.35840/2631-5068/6523	2019 Impact Factor:0.44*(to be indexed in the Quartile Rank in next years)	
Paper-B	**J. R. González-Teodoro**, E. Romero-Cadaval, R. Asensi, R. Prieto and V. Kindl, "New electrical parameters extraction method based on simplified 3D model using finite element analysis", COMPEL - The international journal for computation and mathematics in electrical and electronic engineering, vol. 39, no. 2, pp. 297-316. (29/11/2019). doi:10.1108/COMPEL-02-2019-0075	Computer, Interdisciplinary Applications 108/109 (Q4) Engineering, Electrical and Electronic 248/266 (Q4) Mathematics Applied 227/260 (Q4)	Applied Mathematics 273/510 (Q3) Computer Science 390/636 (Q3)
Paper-C	**J. R. González Teodoro**, Enrique Romero-Cadaval and Rafael Asensi. "Per-unit Hysteresis and Eddy Loss Method based on 3D Finite Elements for Non-Symmetric Toroidal Magnetic" IEEE Access, vol. 8,pp. 34919-34928 (19/02/2020) https://doi.org /10.1109/ACCESS.2020.2975063	Computer, Information Systems 26/90 (Q1) Engineering, Electrical and Electronic 61/266(Q1) Telecommunications 19/88 (Q2)	General information 47/299 (Q1) Computer Science 45/221 (Q1) Material Science 155/460 (Q2)
Paper-D	**J. R. González-Teodoro**, E. Romero-Cadaval, R. Asensi and V. Kindl. "Determination of Wire Resistance Caused by Skin Effect Using Modified 3D Finite Element Model", Springer Electrical Engineering. vol.102, pp 1513-1520 (20/3/2020) doi: 10.1007/s00202-020-00975-y	Engineering, Electrical and Electronic 208/266 (Q4)	Applied Mathematics 181 /510(Q2) Electrical and Electronic Engineering 326/ 670(Q2)

| Paper-E | **J.R. González Teodoro,** Vladimir Kindl, Enrique Romero-Cadaval and Rafael Asensi, "Equivalent Electrical Model of an Inductor Excited by a Triangular Current including Saturation", Komunikace journal Vol .3 pp.15-22, 07/08/2020. doi: 10.26552/com.C2020.3.15-22 | Mechanical Engineering 181/510(Q2) Electrical and Electronic Engineering 348/670(Q3) |

- CONFERENCE PUBLICATIONS

Paper-F	**J. R. González Teodoro**, Vladimir Kindl, Enrique Romero-Cadaval and Rafael Asensi, "Analysis of Skin Effect in Single Wire Resistance by Finite Element Methods", IEEE Proceedings, 14th International Conference on Compatibility, Power Electronics and Power Engineering, Setubal, 2020. doi: 10.1109/CPE-POWERENG48600.2020.9161540	IEEE Proceedings
Paper-G	**J. R. González Teodoro**, Enrique Romero-Cadaval and Rafael Asensi, "Simplificaciones para modelar componentes magnéticos", Seminario anual de automática, electrónica, industrial e instrumentación, Córdoba, junio 2019. ISBN: 978-84-17171-49-0	Conf. Proceedings
Paper-H	**J. R. González Teodoro**, Enrique Romero-Cadaval and Rafael Asensi. "Análisis del Efecto Pelicular y de Proximidad en Componentes Inductivos utilizando Modelado", Seminario anual de automática, electrónica, industrial e instrumentación, Barcelona, Julio 2018. ISBN: 978-84-947311-2-9	Conf. Proceedings

- PER-REVIEWED CONFERENCES

Poster-A	**J. R. González-Teodoro**, Y. Zhai, E. Romero-Cadaval, R. Asensi, R. Feder, "Simplifications in 3D modeling in electromagnetic analysis" New Jersey Entrepreneurial Network Conference 2018	New Jersey Entrepreneurial Network (USA) , 05/05/2018
Poster-B	**J. R. González-Teodoro**, Y. Zhai, E. Romero-Cadaval, R. Feder, "Simplifications in magnets components for 3D electromagnetic analysis" Princeton Research day 2018	Princeton University, NJ (USA), 010/05/2019
Poster-C	**J. R. González-Teodoro**, E. Romero-Cadaval, R. Asensi, "Método de estimación de las pérdidas de los conductores y del núcleo de los componentes inductivos asimétricos mediante la técnica de análisis de elementos finitos 3D", III congreso luso-extremeño de ciencias y tecnología. Noviembre 2019. ISBN: 978-972-134-8	Universidad de Évora, (Portugal). 25-26.11.2019

- CONFERENCES

Poster-1	**J. R. González-Teodoro**, E. Romero-Cadaval, R. Asensi, "Análisis de pérdidas de histéresis en componentes inductivos" Jornadas Doctorales de la UNEX 2018	Universidad de Extremadura, 23/11/2018
Poster-2	**J. R. González-Teodoro**, E. Romero-Cadaval, R. Asensi, "Optimización de componentes inductivos asimétricos mediante la técnica de análisis de elementos finitos 3D" Jornadas Doctorales de la UNEX 2019	Universidad de Extremadura, 29/11/2019

6.2 Activities

- International Mentions

Mention 1	Doc. Ing. Bohumil Skala, Ph.D.	University of West Bohemia (CZ) Innovation Centre for Electrical Engineering
Mention 2	Doc. Guillermo Frank, Ph.D.	Consejo de investigaciones científicas (AR) Departamento de Física
Mention 3	Doc. David Carrillo. Ph.D.	CERN (CH) Electrical Engineering Section
Mention 4	Doc. Emmanuel Faelle. Ph.D.	ESS (SE) Physics Department
Mention 5	Doc. Brian Johnson. PhD.	University of Washington (US) Electrical Engineering Department

- INTERNATIONAL STAY

In the Engineering department at the Princenton Plasma Physicis Lab

- SEMINAR SPEAKER

Seminar A	Maxwell for Everybody. Getting to Started with Maxwell	Princeton University, New NJ (USA), 22.02.2018
Seminar B	Electromagnetic Analysis under FEA and computational limitations	Princeton University, New NJ (USA), 24.06.2018
Seminar C	Análisis electromagnéticos en 3 dimensiones	Universidad de Sevilla 22.10.2019
Seminar D	Magnetic Component Modeling based on 3D FEM	Universidad de Extremadura WEBINAR

- SEMINARS

Seminar 1	Use of Oscilloscope to get experimental results to compare with Maxwell.	Princeton University, New NJ (USA), 18.10.2017
Seminar 2	Asymmetric Distribution of Toroidal Eddy Current ATEC to explain AVDE load in JET and ITER.	Princeton University, New NJ (USA), 17.10.2017
Seminar 3	ITER procedures for electromagnetic analyses.	Princeton University, New NJ (USA), 17.10.2017
Seminar 4	Description the design and accomplishments of IBES to a PPPL colloquium	Princeton University, New NJ (USA), 17.10.2017
Seminar 5	Use of Maxwell	Princeton University, New NJ (USA), 17.10.2017
Seminar 6	Programming for Everybody (Getting Started with Python)	Online (University of Michigan) 13/12/2017

Seminar 7	Differential Power, a fundamental limit of power conversion	Centro de Electrónica Industrial. Politécnica de Madrid, 18/10/2019
Seminar 8	Partículas atmosféricas emitidas promotores de combustión interna	Universidad de Extremadura, 23/09/2019
Seminar 9	Biomonitorización de contaminantes orgánicos mediante vegetación	Universidad de Extremadura, 23/09/2019
Seminar 10	Desarrollo de un nuevo método analítico para la determinación óptica de BC en muestras de nieve, aplicado a la criosfera de Los Andes	Universidad de Extremadura, 23/09/2019

- TRAININGS

Training 1	SOFT 1 English Advanced Workshop	Universidad de Extremadura, Academic Year 2018-2019
Training 2	SOFT 52CC Tips para hablar en público	Universidad de Extremadura, Academic Year 2018-2019
Training 3	SOFT 95 Profesores Noveles	Universidad de Extremadura, Academic Year 2018-2019
Training 4	SERVIER: How to write great papers and get published	Universidad de Extremadura, 17.06.2019
Training 5	SOFT 5 Diseño Pedagógico y elaboración de recursos didácticos para asignaturas en campus virtual UEX	Universidad de Extremadura, Academic Year 2019-2020
Training 6	SOFT 71BA Robótica educativa adaptada al currículo de educación primaria	Universidad de Extremadura, Academic Year 2019-2020
Training 7	SOFT 80 Virtualización de contenidos prácticos	Universidad de Extremadura, Academic Year 2019-2020

6.3 Short Curriculum Vitae

	EDUCATION	
	Ntra. Sra. del Carmen (H.H. Maristas)	Badajoz (ES)
1987-1999	Medium-High School	
	Universidad de Extremadura	Badajoz (ES)
1999-2006	Bachelor and Master of Science in Industrial Engineering	
2008-2010	DEA: Analysis to improve the lab Benito Mahedero's cryogenic system	
	Universita degli studenti di Parma	Parma (IT)
2005-2006	Final Project: The problem of torsion in beams with thin walled sections	
	Wrexham University	Wrexham (UK)
2006	Courses in Aeronautical Engineering	
	San Jorge University. SEAS	Distance Learning
2007-2008	Post-grade in CATIA 3D	
	Universidad católica de Ávila	Ávila (ES)
2019-2020	Master's in secondary teacher training (Physics & Chemistry)	

Chapter 6

PROFESIONAL EXPERIENCE

	European Spallation Source Bilbao	Bilbao(ES)
2020	Lead Engineer	
	Princeton University	Princeton (US)
2016-2018	Lead Engineer	
2013-2016	Rucker. International Termonuclear Experimental Reactor In Vessel Engineer	Cadarache (FR)
	CIEMAT	Madrid (ES)
2011-2013	Researcher	
	Empresarios Agrupados. Central Nuclear de Almaraz	Almaraz (ES)
2007-2011	Electrical Engineer	

- PUBLICATIONS

FUSION	
Paper- 4	**J. R. González-Teodoro**, Matthew Clough, Alex Martin, Nick Woods, Alejandro Suarez, Gonzalo Martinez, Gicquel Stefan and Ma Yunxing, "Distribution of the In-Vessel Diagnostics in ITER Tokamak", Fusion Engineering and Design Vol. 114, 2016, pp 180-1286. doi: 10.1016/j.fusengdes.2016.12.009
Paper-5	**J. R. González-Teodoro**, Patrick Martin, Trevor Edlington, Alex Martin, Charles Millot, Tétény Baross, Miklós Palánkai,Sandor Szalardy, Andras Korossy-khayll and DanielNagy, "In-Vessel Electrical Integration in ITER-Requirements and Solutions", Fusion Engineering and Design Vol.127, pp.99-105, 2017. doi:10.1016/j.fusengdes.2017.12.001
Paper-6	**J. R. Gonzalez-Teodoro**, Y. Zhai, R. Feder, M. Gomez, A. Zolfaghari and D. Johnson, "Progress on the Design Development for Hard Core Components for USDA Diagnostics at ITER," in IEEE Transactions on Plasma Science, vol. 46, no. 6, pp. 2231-2237, June 2018. doi: 10.1109/TPS.2018.2795750
Paper-7	N. D. Atnafu, A. Brooks, D. Cai, J. Dellas, S. Gerhardt, J. Menard, M. Ono, G. Labik, P. Titus and **J. R. González-Teodoro**, "NSTX-U In-Vessel Control Coils' Design Concept," in IEEE Transactions on Plasma Science, vol. 46, no. 5, pp. 1528-1533, May 2018. doi: 10.1109/TPS.2018.2822555
Paper-8	Y. Zhai, Allan Basile, R. Feder, W. Wang, Jinping Chen, Andrei Khodak, J. Klabacha, D. Johnson, M. Hause, M. Mesineo, H. Zhang, **J. R. González-Teodoro**, Julio Guirao and Silvia Iglesias,"Design and Analysis Progress of ITER Diagnostic Equatorial Port #09," in IEEE Transactions on Plasma Science, vol. 46, no. 5, pp. 1254-1261, May 2018. doi: 10.1109/TPS.2017.2788188
Paper-9	Gonzalo Martínez, Alex Martin, Christopher Watts, Evgeny Veshchev, Roger Reichle, Pavel Shigin, Flavien Sabourin, Stefan Gicquel, Raphael Mitteau, **J. R. González- Teodoro** "Diagnostic integration solutions in the ITER first wall", Fusion Engineering and Design Vol. 98-99, 2015, pp 1548-1551. doi: 10.1016/j.fusengdes.2015.06.046
FISSION	
Paper- 10	J. Cabrera and **J.R. González-Teodoro**, "Requirements for the installation to the new megaphony and interphony system", RSNE´2009 Spanish Nuclear Society Meeting 35.

BOOK CHAPTER-1	J. R. González Teodoro. Chapter 8, Science Basic and Nuclear Technology Book (https://www.sne.es/images/stories/recursos/publicaciones/Varios/LibroCBCTN-ed2.pdf) Depósito legal: M-24599-2013

DIVULGATION	
ARTICLE-1	**J.R. González Teodoro**, C. Vázquez-Rodriguez and G. Jimenez Varas, "¿Deberían cerrar las centrales nucleares españolas", Digital Journal The conversation, 25 marzo 2019 **Republicado en UPM digital**.
ARTICLE-2	Santiago Cambero and **J.R. González Teodoro**, "Como sobreviviremos en 2030" Digital Journal The conversation, 5 mayo 2019. **Republicado en ABC.**
ARTICLE-3	**J.R González Teodoro** and Miguel Jurado Vargas, "¿Es la fusión nuclear la energía del futuro?" Digital Journal The conversation, 10 abril 2019. **Republicado en El Comercio.**
ARTICLE-4	**J. R. González Teodoro** and F. García Caro, "Como lograr que el turismo siga siendo un motor económico… sin calentar el planeta", Digital Journal The conversation,4 noviembre 2019. **Republicado en la SER digital.**
ARTICLE-5	**J. R. González Teodoro** and F. García Caro, "La computación cuántica nos echa una mano", Digital Journal The objetive, 17diciembre 2019.
ARTICLE-6	**J. R. González Teodoro** and F. García Caro, "Vuele con moderación", Digital Journal The conversation, 26 febrero 2020.
ARTICLE-7	**J. R. González Teodoro** and L.I. Hojas Hojas, "¿Sobrevivirán las viejas profesiones a la creciente automatización?", Digital Journal The conversation, 1 marzo 2020. **Republicado en LA RAZON.**

- ACTIVITIES

-Volunteer with Spanish Red Cross in Spain (International Cooperation and Environmental Projects)

-Volunteer with Red Cross in Aix en Provence

-Volunteer with PSE "Pour un Sourire d'Enfant" in Cambodian (4 weeks)

-Collaboration in a book for the Nuclear Young People Association

- AWARDS

1) ITER Award Cross Functional category, In Vessel Configuration

2) Prize for the best recharge system for the 20R1 Nuclear Power Plant Almaraz

3) Finalist in Renault formula 1 grant, (into 30 people, Spain)

7 References

[1]   D. W. Hart, "Power Electronics," in *Introduction*, ISBN:978-0-07-338067-5, Mc Graw Hill, 2010.

[2]   "An introduction to magnetic components," https://www.newelectronics.co.uk/, [Online]. Available: https://www.newelectronics.co.uk/electronics-technology/an-introduction-to-magnetic-components/75414/. [Accessed 01 04 2020].

[3]   "http://www.mitsubishielectric.com/," http://www.mitsubishielectric.com/, [Online]. Available: http://www.mitsubishielectric.com/semiconductors/triple_a_plus/technology/01/index.html. [Accessed 30 03 2020].

[4]   S, "Boost Converter," electrical4u, [Online]. Available: https://www.electrical4u.com/boost-converter-step-up-chopper/. [Accessed 01 04 2020].

[5]   J. C. R. Caro, F. Peng, H. Cha and C. Rogers, "Z-Source-Converter-Based Energy-Recycling Zero-Voltage Electronic Loads," *IEEE Transactions on Industrial Electronics,* vol. 56, no. 12, pp. 4894 - 4902, 2010.

[6]   "Universal DC / DC converter," http://danyk.cz/, [Online]. Available: http://danyk.cz/univ_m_en.html. [Accessed 30 03 2020].

[7]   "High Density 30W DC-DC PMBus Buck Converter with Inductor Mounted Over the Converter to Save Space," Texas Instrument, [Online]. Available: http://www.ti.com/tool/PMP10364. [Accessed 30 03 2020].

[8]   "Single Phase EE 28 Transformer, 60 VA," Indiamart, [Online]. Available: https://www.indiamart.com/proddetail/ee-28-transformer-16239436748.html. [Accessed 30 03 2020].

[9]   R. e. a. Asensi, "Modelling high-frequency multiwinding magnetic components using finite element analysis," *IEEE Transactions on Magnetics,* vol. 43, no. 10, pp. Vol. 43, No. 10, 2007.

[10]   R. P. J. C. O. G. a. J. U. R. Asensi, "Integrating a model for high frequency magnetic components in a power electronics CAD system," *IEEE Internaqtional Telecommunications and ENergy Conference,* 1995.

[11]   R. P. J. C. O. G. a. J. U. R. Asensi, "A CAD tool for magnetic components modelling," *Applied Power Electronics Conference,* 1996.

[12]   R. e. a. Prieto, "Interleaving techniques in magnetic components," *IEEE APEC,* pp. 931-936, 2007.

[13]   R. A. J. C. O. G. a. J. U. R. Prieto, "Model of the capacitive effects in magnetic components," *IEEE Power Electronics Specialists Conference,* 1995.

[14]   R. A. J. C. O. G. a. J. U. R. Prieto, "New modelling strategy for high frequency magnetic components," *21th IEEE International Conference on Industrial Electronics, Control and Instrumentation,* 1995.

[15]   J. C. a. J. U. R. Prieto, "PEmag, CAD para modelado y simulación de componentes magnéticos," *Revista Indumática,* 1998.

[16]   D. Cheng, Fundamentals od Engineering Electromagnetics, Addison-Wesley Publishing Company, 1993.

[17]   K. Karsai, Large Power Tranformers, Elservier, 1987.

[18]   Relibond, "ReliBond ApS," ReliBond ApS, 26 03 2020. [Online]. Available: http://www.relibond.com/cu-enamelled/.

[19]   P. G. a. F. L. A.W. Lotfi, "Proximity Effects in Coils for High Frequency Power Applications," *IEEE Transactions on Magnetics,* vol. 28, no. 5, p. 12691271, 1995.

[20]   A. L. a. F. Lee, "Proximity Losses in Short Coils of Circular Cylindrical Windings," *IEEE PESC Record,* pp. 1253-1260, 1992.

[21]   "Circuiteglobe," Circuiteglobe, 26 03 2020. [Online]. Available: https://circuitglobe.com/proximity-effect.html.

[22]   K. N. a. M. Kuo, "Effects of Air Gaps on Windings Loss in High-Frequency Planar Magnetics," *IEEE PESC Record,* pp. 1112-1119, 1988.

[23]   M. C. D. A. O. Z. William G.Hurley, "Magnetic Circuit Design for Power Electronics," in *Power Electronics Handbook*, Elservier, 2018.

[24]   "http://www.engineer.plus/blog/2016/10/18/transformer-2d-vs-3d-modeling/," 26 03 2020. [Online]. Available: http://www.engineer.plus/blog/2016/10/18/transformer-2d-vs-3d-modeling/.

[25]   F. L. R. R. a. D. N. G. Skutt, "Leakage Inductance and Termination Effects in a HighPoer Planar Magnetic Structure," *Seminar VPEC,* pp. 71-78, 1994.

[26]   A. P. J. D. J. A. a. F. N. J.M. Lopera, "A Complete Trasnformer Electric Model, Including Frequency and Geometry Effects," *IEEE PESC Record,* pp. 1247-1252, 1992.

[27]   H. O. a. T. W. V.A. Niemela, "CrossCoupled Secondaries Model for Multiwinding Trasnformers with Parameters Calculated from ShortCircuit Impedances," *IEEE PESC Record,* pp. 780-785, 1990.

[28]   G. S. A. U. Y. C. T. W. H. O. a. R. W. V.A. Niemela, "Calculating the ShortCircuit Impedances of a Multiwinding Trasnformer from its Geometry," *IEEE PESC Record,* pp. 607-617, 1989.

[29]   A. L. a. F. Lee, "Two Dimensional Field Solution for High Frequency Transformer".

[30]   J. C. R. P. J. Uceda, "Review of current modeling tecniques for high frequency magnetic components," *Power Electronics and Motion Control,* 1996.

[31]   M. C. Murat Tören, "A Comparison of the Programmes Using Finite Element Software in," *International Journal of Applied Mathematics, Electronics and Computers,* no. ISSN: 2147-82282147-, 2016.

[32]   E. S. a. S. G. Renuka Rajput-Ghoshal, "jlab," 2 April 2018. [Online]. Available: https://www.jlab.org/sites/default/files/magnet-group/training-presentations/opera_vs_maxwell_april_2nd_2018.pdf. [Accessed 22 05 2020].

[33]   R. S. a. R. S. S. M.A. Coulson, "Representation of Magnetic Characteristics, Including Hysteresis , Using Preisach´s Theory," *Proceedings of IEEE,* vol. 124, no. 10, p. 895898, 1977.

[34]   T. D. a. I. Mayergoyz, "On Numerical Implementation of Hysteresis Models," *IEEE Transactions on Magnetics,* vol. 21, no. 5, p. 18531855, 1985.

[35]   D. J. a. D. Atherton, "Theory of ferromagnetic hysteresis," vol. 61, no. 1-2, pp. 48-60, 1986.

[36]   B. S. a. J. S. D.L. Atherton, "A New Approach to PReisach Diagrams," *IEEE Transactions on Magnetics,* vol. 23, no. 3, pp. 1856-1865, 1987.

[37]   D. J. a. J. Thoekle, "Theory of Ferromagnetic Hysteresis. Determination of Model Parameters from Experimental Hysteresis Loop," *IEEE Transactions on Magnetics,* vol. 25, no. 5, pp. 3934-3936, 1989.

[38] R. Erickson, "Introduction to Power Electronics ECEN 4797/5797," 05 12 2018. [Online]. Available: https://ecee.colorado.edu/~ecen5797/course_material/Lecture40.pdf. [Accessed 23 04 2020].

[39] J. Ferreira, "Appropriate Modeling of Conductive Losses in the Design of Magnetic Components," *IEEE PESC Record,* pp. 780-785, 1990.

[40] P. B. a. J. V. Vlerken, "Modeling of Electromagnetic Systems," *IEEE Transactions on Magnetics,* vol. 27, no. 6, pp. 4509-4514, 1991.

[41] Y. Z. a. K. M. Smedley, "Analysis and Design of a Single-Switch High Step-Up Coupled-Inductor Boost Converter," *IEEE Transactions on Power Electronics,* vol. 35, no. 1, pp. 535-545, 2020.

[42] A. D. e. al., " Modelling and estimation of leakage phenomena in magnetic circuits," Vols. 23-27, no. pp. 213-226, 1986.

[43] N. K. M. K. D. Murthy-Bellur, "Transformer winding loss caused by skin and proximity effects including harmonics in pulse-width modulated DC–DC flyback converters for the continuous conduction mode," *IET Power Electronics,* vol. 4, no. 4, pp. 363-373, 2011.

[44] J. Rosa, "Calculation of Flux Linkages in Multiwinding Trasnformers," *IEEE PESC Record,* pp. 639-644, 1986.

[45] P. Szczerba, S. Ligenza, P. Trojan and C. Worek, "Practical Design Considerations of Inductor AC Resistance Calculation Methods," in *20th International Symposium on Power Electronics (Ee)*, Novi Sad, Serbia, Serbia, 2019.

[46] A. G. G. E. L. R. Jordi-Roger Riba, "A Computer Model for Teaching the Dynamic Behavior of AC Contactors," *IEEE Transactions on Education ,* vol. 2, no. 53, pp. 248-256, 2010.

[47] D. Honorio and A. F. ,. B. O. ,. J. O. P. P. Luiz Henrique S. C. Barreto, "Modular transformer in isolated multiport power converters," in *IEEE Southern Power Electronics Conference (SPEC)*, Puerto Varas, Chile, 2017.

[48] K.-T. K. ,. J.-H. P. ,. S.-J. L. ,. T.-K. C. Yoon-Sun Lee, "Characteristic analysis and design of novel high-frequency shell-type coaxial transformer," *IET Power Electronics,* vol. 13, no. 12, pp. 2027-2034, 2017.

[49] K. D. T. N. Ming Lu, "Analytical Calculation of Proximity-Effect Resistance for Planar Coil With Litz Wire and Ferrite Plate in Inductive Power Transfer," *IEEE Transactions on Industry Applications,* vol. 55, no. 3, pp. 2984-2991, 2019.

[50] S. S. J. L. J. Liu, "Accurate Expressions of Mutual Inductance and Their Calculation of Archimedean Spiral Coils," *Energies,* vol. 12, no. 10, p. doi:10.3390/en12102017, 2019.

[51] R. Batcher, "Rapid Determination of Distributed Capacity of Coils," *Proceedings of the IRE,* pp. 301-324, 1921.

[52] A. J. Palermo, "Distributed Capacity of Single-Layer Coils," *Proceedings of the IRE,* vol. 22, no. 7, pp. 897-905, 1934.

[53] J. Morecroft, "Resistance and Capacity of Coils at Radio Frequencies," *Proceedings of the IRE,* p. 261289, 1922.

[54] H. Zuhrt, "Einfache Näherungsformeln für die Eigenkapazität mehrlagiger Spulen," *Elektrotechnische Zeischirgt,* vol. 27, pp. 662-665, 1934.

[55] Z. Qin, Z. Shen and F. Blaabjerg, "Modelling and analysis of the transformer current resonance in dual active bridge converters," in *IEEE Energy Conversion Congress and Exposition (ECCE)*, Cincinnati, OH, USA, 2017.

[56] i. J. C. 1. M. R. M. K. Piotr Musznicki, "Adaptive estimation of the transformer stray capacitances for DC–DC converter modelling," *IET Power Electronics,* vol. 9, no. 15, pp. 2865-2870, 2016.

[57] I. Iatcheva, "Application of field modeling and determination of parameters in electrical engineering education," *International journal for computation and mathematics in electrical and eletronic engineering,* vol. 37, no. 5, pp. 1585-1596, 2018.

[58] Y. O. e. al., "Improvement of topology optimization method based on level set function in magnetic field problem," vol. 37, no. 2, pp630-644, 2016.

[59] D. S. Kiselev, "Actual problems of electronics instrument engineering," in *13th International Scientific Technical Conference (APEIE)*, 2016.

[60] A. B. Messaoud, "Multimodel approach for modeling of nonlinear systems:validities' optimal computation," *International Journal for computation and mathematics in electrical and electronic engineering,* vol. 37, no. 1, pp. 153-175, 2018.

[61] O. Aljohani, "HIgh frequency power trasnformer modeling for frequency response analysis studies," in *International conference on confition monitoring and diagnostics (CMD)*, 2016.

[62] R. Phukan, "A new frequency simulation model for multi-winding trasnformers used in switched-mode power supplies," in *IEEE Energy conversion congress and Exposition (ECE)*, 2016.

[63] K. Niyomsatian, "Experimental extraction of winding resistance in litz-wire trasnformers-influence of winding mutual resistance," *IEEE transactions on power electronics,* p. Early access, 2018.

[64] O. Bottesi, "Finite Element small-signal simulation of electromagnetic devices considering eddy current in the laminations," *IEEE transactions on magnetics,* vol. 53, no. 5, 2017.

[65] Y. Liu, "A simplified finite element model of hybrid excitation synchronous machine with radial/axial flux paths via magnetic equivalent circuit," *IEEE transactions on magnetics,* vol. Early access, 2017.

[66] Y. Zhong, "An improved magnetic circuit of a 3-DOF magnetic bearing considering leakage and cross coupling effects," *IEEE transactions on magnetics,* vol. Early access, 2017.

[67] L. D'Angelo, "Quasi 3D Finite Element Method for simulating cyclindrical induction heatind devices," *IEEE jounral on multiscale and multiphysics computational techniques,* vol. 2, 2017.

[68] M. Jafari, "Modeling of magnetic flux in multi-winding toroidal core high frequency trasnformers using 3D reluctance network model," in *IEEE PEDS*, 2015.

[69] Z. Zhengyuan, "Deformation simulation and analysis of power trasnfomer windings," in *IEEE PES Asia-Pacific power and energy conference*, China, 2016.

[70] K. Pluk, "3D hybrid analytical modeling: 3D fourier modeling conbined with mesh -based 3D magnetic equivalent circuits," *IEEE transactions on magnetics,* vol. 51, no. 12, 2015.

[71] C. H. ,. X. L. ,. L. H. ,. X. F. Li Tong, "FEM analysis on the losses characteristic and temperature distribution of laminated core in MCR," in *IEEE Sustainable Power and Energy Conference (iSPEC)*, Beijing, China, , 2019.

[72] H. K. Chisepo, C. Gaunt and L. D. Borrill, "Measurement and FEM analysis of DC/GIC effects on transformer magnetization parameters," in *IEEE Milan PowerTech*, Milan, Italy, 2019.

[73] J. R. Gonzalez-Teodoro, "Simplifications in 3D high-low frequency models of multiwinding magnetic components (EE & Toroidal cores)," *International Journal of Magnetics and Electromagnetism,* vol. 1, no. 3, 2016.

[74] J. R. Gonzalez-Teodoro, "Study of limitations in magnetic components modeling 3D," *Conference SSAEI,* 2014.

[75] J. R. E. R.-C. R. A. Gonzalez-Teodoro, "Simplificaciones para modelar componentes magneticos en 3D (nucleos EE)," *Conference SSAEI,* 2018.

[76] Ferroxcube, Data Handbook, 2017.

[77] Ansys, "Material property data for ansys.," www.matweb.com/index.aspx, 2018.

[78] A. Maxwell, "http://ansoft-maxwell.narod.ru/," Ansoft Maxwell, 2005. [Online]. Available: http://ansoft-maxwell.narod.ru/en/CompleteMaxwell3D_V11.pdf. [Accessed 22 05 2020].

[79] H. Zhang, "New analytical equations for skin and proximity effects in interconnects operated at high frequency," in *IEEE Electron devices technology and manufacturing conference (EDTM)*, 2017.

[80] R. D. e. al., "Skin effect compartive analysis in electric cables using coimputational simulations," Niteroi, 2018.

[81] H. Igarashi, "Semi-analytical approach for finite element analysis of multi turn coil considering skin and proximity effects," *IEEE transactions on magnetics,* vol. 53, 2017.

[82] C. Bednarz, "Efficient multiport equivalent circuit and proximity effect in parallel conductors with arbitrary cross sections," *IEEE transactions on electromagnetic compatibility,* vol. PP, no. 99, 2018.

[83] V. Belevitch, "The lateral skin effect in a flat conductor," *Philips tech,* vol. 6/7, no. 18, pp. 221-231, 1971.

[84] P. Dowell, "Effects of eddy currents in trasnformer windings," vol. 113, no. 8, pp.1387-1394, 1966.

[85] J. Ferreira, "Improved analytical modeling of conductive losses in magnetic components," vol. 9, no. 1, pp. 127-131, 1994.

[86] C. P. Steinmetz, "On the law of hysteresis," *Procedings IEEE,* vol. 72, no. 2, pp. 196-221, 1984.

[87] H. J. e. al., "Die ferromagnetischen Konstaten für scwache Wechselfeder," vol. 1, no. pp.8, 1924.

[88] R. P. a. C. Bean, "Calculation of the energy loss in magnetic sheet materials using a domain model," vol. 29, no. pp. 533-535, 1958.

[89] G. B. e. al., "General properties of power losses in soft ferromagnetics materials," vol. 24, no. 1,pp. 621-630, 1988.

[90] G. e. al., ""Physical interpretation of eddy current losses in ferromagnetic materials II, analysis of experimental results," vol. 57, no. 6, pp. 2118-2126, 1985.

[91] T. K. e. al., "Relation between rotational and alternating losses in electrical steel sheets," vol. 160, no. pp. 145-146, 1996.

[92] L. M. a. J. Scheinder, "Magnettechnik-Grundlagen, Weksoffe, Anwendugen," no. 2006, 2006.

[93] J. R. e. al., "Claculation of losses in ferro and ferromagnetic materials based on the modified Steinmetz equation," Vols. 37 (4), pp. 1055-1061, 2001.

[94] J. L. e. al., "Improved calculation of core loss with no sinosoidal waveforms," 2001.

[95] K. V. e. al., "Accurate prediction of ferrite core loss with no sinousoidal waveforms using only Steinmetz equations parameters," Vols. pp.36-41, 2002.

[96] J. B. J. K. a. A. E. J. Mullethaler, "Improved Core-Loss Calculation for Magnetic Components Employed in Power Electronics Systems," vol. 27, no. 2, pp.964-973, 2012.

[97] F. P. e. al., "Über die magnetische Nachwirkung," vol. 94, no. 5, pp. 277-302, 1935.

[98] C. Group, "Flux 10-2D/3D Applications User´s guide," 2007.

[99] M. H. e. al., "An energy-based harmonic constituve law for magnetic cores with hysteresis," vol. 44, no. 6, pp.922-925, 2008.

[100] S. S. a. K. H. D. Eggers, "Advanced Iron-Loss Estimation for Non-linear Material behaviour," vol. 48, no. 11, pp. 3021-3024, 2012.

[101] D. L. a. R. D. Doncker, "Simulation of power losses with MATLAB/Simulink using advanced power devices models," no. pp. 71-75, 2002.

[102] S. Bang, "An improved empirical formulation for magnetic core losses estimation under non-sinuoidal induction," *IEEE transactions on power electronics,* vol. 32, no. 3, 2017.

[103] Y. Shuichao, "Core loss calculation of the soft ferrite cores in high frequency trasnformer under non-sinusoidal excitation," in *20th International conference on electrical machines and systems (ICEMS)*, 2017.

[104] Y. Shuichao, "Comparative analysis of core loss calculation methods for magnetic materials under non-sinusoidal excitations," *IEEE transactions on magnetics,* vol. 54, no. 11, 2018.

[105] S. Shimokawa, "Fast 3D optimization of magnetic cores for loss and volume reduction," *IEEE transactions on magnetics,* vol. 54, no. 11, 2018.

[106] A. K. S. e. al., "Investigation of Conduction and Switching Power Losses in Modifed Stacked Multicell Converter," vol. 63, no. 12, 2016.

[107] L. Y. e. al., "A simplified analytical calculation model of average power loss for modular multilevel converter," vol. 66, no. 3, 2019.

[108] H. l. website, "https://www.codecogs.com/library/physics/magnetism/magnetic-hysteresis.php," [Online].

[109] P. Mannion, "The difference between inductive proximity, displacement, and eddy-current sensors," EE NEWS Analog, 2016 4 6. [Online]. Available: https://www.eenewsanalog.com/news/difference-between-inductive-proximity-displacement-and-eddy-current-sensors-0/page/0/1. [Accessed 21 04 2020].

[110] Kharagpur, "Magnetic circuits and core losses," in *Magnetic circuits and core losses*, EE II, Version 2, p. Module 6.

[111] H. Yehui, "Evulation of magnetic materials for very high frequency power applications," *IEEE transactions on power electronics,* vol. 27, no. 1, pp. 425-435, 2012.

[112] C. J. Dunlop, "Doctoral Thesis: Modeling magnetic core loss for sinusoidal waveforms," Naval Postgraduate School, Monterey, California, 2012.

[113] "https://www.ansys.com/es-es/products/electronics/ansys-pexprt," [Online].

[114] J.-L. Coulomb, "Framework for the optimization of online computable models," *International Journal for computation and mathematics in electrical and electronic engineering,* p. 33(3), 2014.

[115] Y. Okamoto, "Improvement of topology optimization method based on level set function in magnetic field problem," *International journal for computation and mathematics in electrical and electronic engineering,* vol. 37, no. 2, pp. 630-644, 2018.

[116] M. Chen, "A systematic approach to modeling impedances and current distribution in planar magnetics," *IEEE transactions on Power Electronics,* vol. 31, no. 1, pp. 560-580, 2016.

[117] M. Lu, "An analytical method to calculate winding resistance for planar coil with ferrite plate and litz wire in inductive power transfer," in *IEEE Energy conversion congress and exposition (ECCE)*, 2017.

[118] H. A. Wheeler, "Skin resistance of a trasmission line conductor of polygon cross section," *Proceedings of the IRE,* vol. 43, no. 7, 1955.

[119] T. Asada, "A study on basic characteristics on the proximity effect on conductors," *IEEE transactions on power delivery,* vol. 32, no. 4, 2017.

[120] A. Payne, Skin Effect, proximity effect and the resistance of rectangular conductors, 2016.

[121] P. Wilson, "Advanced modeling and simulation techniques for magnetic component optimization," in *7th International conference on power electronics mand variable speed drives*, 1998.

[122] B. 0. A. B. 51, Reglamento eletronico de baja tension e instrucciones tecnicas complementarias.

[123] R. Utkarsh, "Skin effect modeling in conductors of arbitrary shape through surface admittance and the contour integral method," *IEEE transactions on microwave theory and techniques,* vol. 64, pp. 2708-2717, 2016.

[124]   X. Nan, "An improved calculation of," in *IEEE 34th the nnual conference of power electronics specialist*, 2003.

[125] G. Antonini, "Internal impedance of conductors of rectangular cross section," *IEEE transactions on microwave theory and techniques,* vol. 47, no. 7, 1999.

[126] D. K. e. al., "Comparison of approaches and the software for 3D finite element modeling of harmonic electromagnetic fields," Novosibirsk, 2016.

[127] G. V. P. e. al., "Operating Point Resolved Loss Calculation Approach in Saturated Induction Machines," vol. 64, no. 3, 2017.

[128] P. D. M. Merda, Course subjet: Electromagnetic waves Therory, Sulemen Demiel University. Elektronik ve Haberlegne Muhendisligi, 1992.

[129] J. R. e. al., "Calculation of losses in ferro and ferromagnetic materials based on the modifed Steinmetz equation," vol. 37, no. 4, pp. 1055-1061, 2001.

[130] K. K. a. N. Murakami, "Analysis of High-Frequency Resistance in Transformers," *IEEE PESC Record,* p. 618624, 1989.

[131] G. a. P. Venkatraman, "Analyisis and Measurement of HighFrequency Effects in HighCurrent Trasnformers," *IEEE APEC Record,* pp. 354-364, 1990.

[132] J. Lopera, "Elementos magnéticos en alta frecuencia: estudio, modelado y criterios de diseño," Tesis Doctoral Universidad de Oviedo, 1993.

[133] H. O. a. T. W. V.A. Niemela, "Frequency Independent Element Cross Coupled Secondaries Model for Multiwinding Trasnformers," *IEEE PESC Record,* pp. 1261-1268, 1992.

[134] S. E.-H. a. E. Chang, "Magnetics Modeling for Computer-Aided Design of Power Electronics Circuits," *IEEE PESC Record,* pp. 635-645, 1989.

[135] V. N. G. S. a. T. W. A.M. Urling, "Characterizing High Frequency Effects in Tranformers Windings- a Guide to Several Significant Articles," *IEEE PESC Record,* pp. 373-385, 1989.

[136] V. N. a. T. W. H.A. Owen, "Enhanced Cross-Coupled Secondaries Model for Multiwinding Trasnformers," *IEEE PESC Record,* pp. 1269-1276, 1992.

[137] W. a. P. McNamara, "Characterization of Trasnformer Cores using a New Mutual Impedance Formula," *EPE Record,* vol. 2, pp. 452-457, 1991.

[138] W. a. D. Wilcox, "Calculation of Leakage Inductance in Transformer Windings," *IEEE Transactions on Power Electronics,* vol. 9, no. 1, pp. 121-126, 1994.

[139] W. G. H. a. M. Duffy, "Calculation of Self and Mutual Impedances in Planar Magnetic Structures," *IEEE Transactions on Power Electronics,* vol. 9, no. 1, pp. 121-126, 1994.

[140] A. F. a. S. Stigant, The J. et P. Transformer Book, J.et P. Books, 1973.

[141] J. Collins, "An Accurate Method for Modeling Transformer Winding Capacitances," *IEEE IECON Record,* pp. 1094-1099, 1990.

[142] A. G. a. M. S. L.F. Casey, "Issues Regarding the Capacitance of 1-10MHz Transformers," *IEEE APEC Record,* pp. 352-359, 1990.

[143] M. K. a. G. G. A. Massarini, "Lumped Parameters for Single and Multiple Payer Inductors," *IEEE PESC Record,* pp. 295-301, 1996.

[144] E. R.-C. R. A. Jorge Rafael González-Teodoro, "Análisis del efecto pelicular y de proximidad en componentes inductivos utilizado modelado en 3D," in *Conference SAAEI 2019*, 2019.

[145] T. M. U. W. P. R. a. L. M. O. G. Ned Mohan, Electrónica de Potencia, Convertidores, aplicaciones y diseño, México: McGraw-Hill. ISBN 987-970-10-7248-6, 2009.

[146] V. A.I, " Physics of Oscillations and Waves," in *Skin Depth and Waveguides*, 978-3-319-72313-6, Springer, 2018.

[147] C. l. P. Arroyo, "Design Methodology of a Trasnformer with an integrated inductor for avionic applications," Universidad Politécnica de Madrid (TFG), Madrid (ES), 2016.

APPENDIX I

<u>List of Tables:</u>

Appendix

List of Figures:

APPENDIX II

<u>*The convergence criteria in Ansys Maxwell*</u> [77]

The maximum energy error is defined as:

$$max\left[\left|S_{ij}^N - S_{ij}^{N-1}\right|\right]$$

Where "i" and "j" cover all matrix entries.

The following fields show how close the solution is to meeting the convergence -criteria entered under:

- *Target Error: Displays the target change in the S-parameters — the delta S you would like to achieve for the solution, entered via the Setup Solution.*

- *Energy Error: Displays the maximum change in the S-parameters from the most recent solution and the previous solution.*

- *Delta Energy: Displays the change in the total energy over the last two passes.*

When the Delta energy falls below the target error value, Maxwell stops the adaptive solution process, even if the specific number of adaptive passes has been not reached. After a solution is completed, use the energy error value to determine if additional passes are need to increase the accuracy the solution, if the value of energy error is still declining from pass to pass, additional passes may increase the accuracy the solution. So, with these definitions, it is possible to understand that the FE numbers that is known is the last pass that the program has been able to manage, and the software has stopped when the program has increased the FE numbers to try to improve the accuracy

APPENDIX III

Computer Resource using to calculate the computer limitations

There are two main computing data for this research: software and hardware.

-Software: Maxwell Ansoft.

-Hardware: 2 computers have been used:

1. - Inter Core ^{TM} i7 920 @ 267 GHz (32, 00 GB)

2. - AMD APU with Radeom ^{TM} HD graphics 1.65 GHz (4, 00 GB)

The only relevance data for the hardware is the RAM memory from the point of view of the finite element number processed by the computer. Other computer features are used defines the process speed for the simulation.

Maximum FE number by computer

A simple analysis has been developed to demonstrate that there is an evident computational limitation depending of the hardware used in the FE analysis. The limitation is due to FE number needed in the simulation using 4 GB. The convergence is not successful is the FE needed for the complete simulation exceed the maximum FE number managed by the compute RAM.

The example to demonstrate this evidence is the simulation of a transformer component (EE.42.21.15) with two different windings using the same hardware:

First winding   AWG 18

Second winding   AWG 24

As it explains, the principal factor to define the FE in a simulation of an inductive component or transformer with EE or Toroidal core is the cross-section wiring for the windings [74].

The analysis consists on the simulation of the same core adding the maximum number of windings, using different cross-sections.

Appendix

*Original Model (Circular cross-section in the winding)*

The following picture represents the increase of FE number when the turns for the winding are increased using a circular cross-section is issued in the component model.
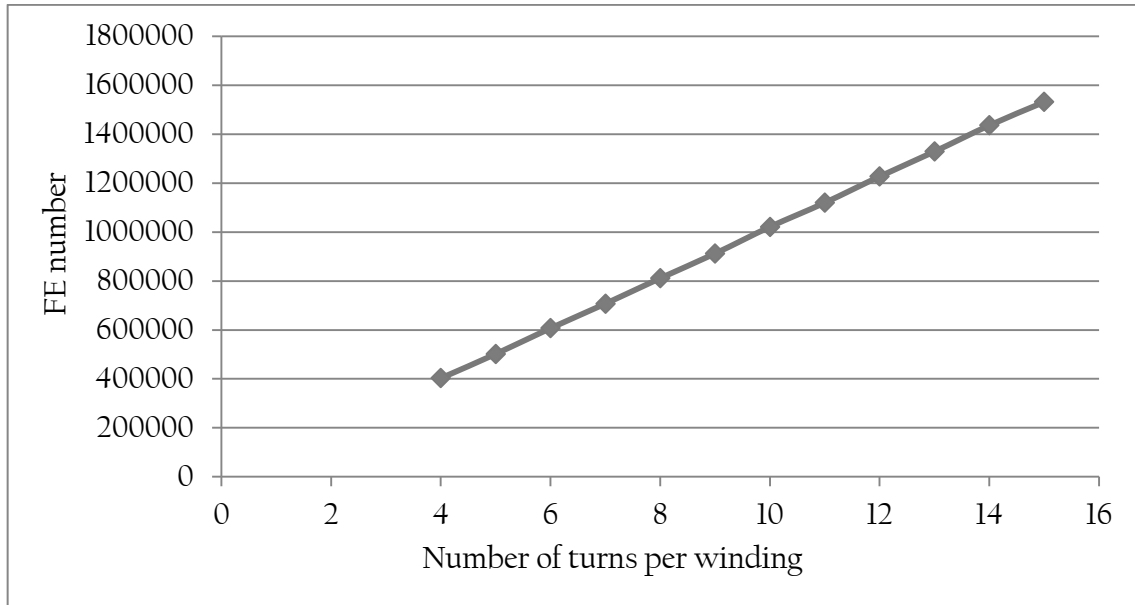
The limitation is 15 turns in each side with 1531421 tetras.

Polygonal Model (Polygonal cross-section ,18 edges)

The following picture represents the increase of FE number when the turns for the winding are increased for this sequence.
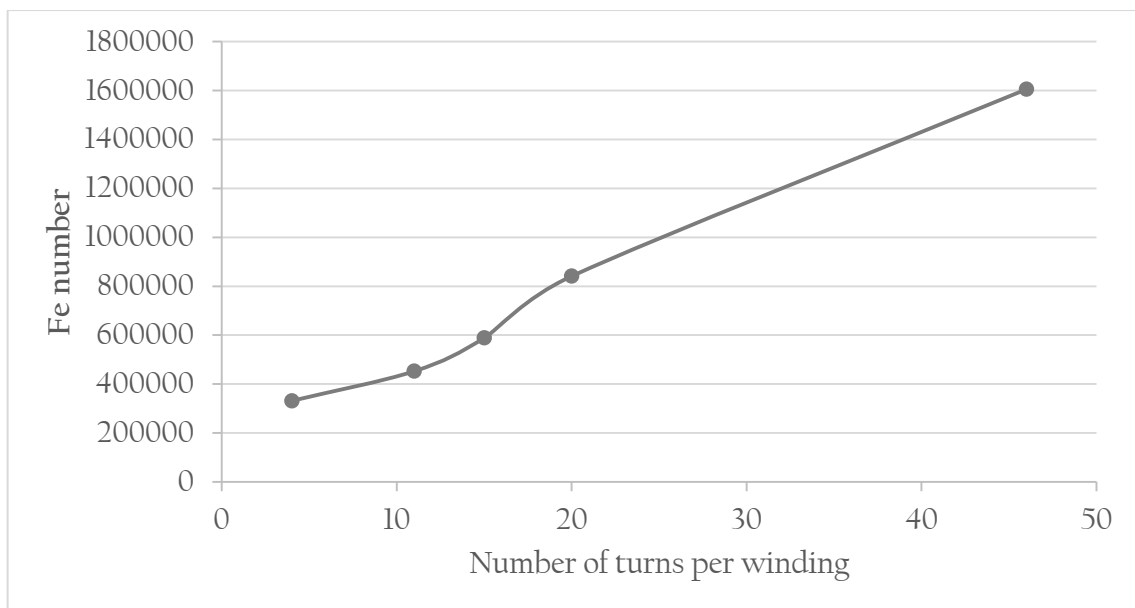
The maximal model was one with: 46 turns (AWG 18) or 24 (AWG24) with 1,604,918 tetras.

Appendix

<u>*Polygonal Model (Polygonal cross-section, hexagonal section)*</u>

A model with 42 turns (AWG 18) or 20 (AWG24) was not been able to manage the computer with 1,421,500 tetras.

The RAM is the main feature to define the maximum number of the FE that it is processed in the analysis. The maximum number of windings in the model depends on the FE number of the model according to the convergence criteria using a regular mesh and energy error of 2%.

Conductor Cross Section	Maximum Fe
Circular	1,531,421
Polygonal 18 edges	1,604,918
Polygonal 6 edges	1,421,500

APPENDIX IV

Scripts used in Ansys Maxwell for electrical parameter extraction procedure

To read the data:

```
' //////////////////////////////////////////
' Maxwell Vbs created by PExprt(TM) Version 7.1.0.4
' © 2012 UPM-SAS IP, Inc.
' //////////////////////////////////////////
Dim oAnsoftApp
Dim oDesktop
Dim oProject
Dim oDesign
Dim oEditor
Dim oModule
Dim f, frq(5)
Dim w1, w2, ip(1, 1)
Set oAnsoftApp = CreateObject("AnsoftMaxwell.MaxwellScriptInterface")
Set oDesktop = oAnsoftApp.GetAppDesktop()
Set oProject = oDesktop.SetActiveProject("P")

frq(0) = "1.0Hz"
frq(1) = "5376.0Hz"
frq(2) = "21507.0Hz"
frq(3) = "48391.0Hz"
frq(4) = "537678.0Hz"
frq(5) = "1209776.0Hz"

For w1 = 0 To 1
  For w2 = 0 To 1
    If w1 = w2 Then
      ip(w1, w2) = "1A"
    Else
      ip(w1, w2) = "0A"
    End If
  Next
Next

For f = 0 To 5
  For w1 = 0 To 1
    Set oDesign = oProject.SetActiveDesign("Setup" + CStr(w1 + 1))
    Set oModule = oDesign.GetModule("FieldsReporter")

    oModule.EnterQty "J"
    oModule.CalculatorWrite "J" + CStr(w1 + 1) + "_" + CStr(f + 1) + ".reg", _
      Array("Solution:=", "Setup" + CStr(w1 + 1) + " : LastAdaptive"), _
      Array("Freq:=", frq(f), _
        "Ipeak1:=", ip(w1, 0), _
        "Ipeak2:=", ip(w1, 1), _
        "Phase:=", "0deg")
```

```
    oModule.EnterQty "H"
    oModule.CalculatorWrite "H" + CStr(w1 + 1) + "_" + CStr(f + 1) + ".reg", _
      Array("Solution:=", "Setup" + CStr(w1 + 1) + " : LastAdaptive"), _
      Array("Freq:=", frq(f), _
        "Ipeak1:=", ip(w1, 0), _
        "Ipeak2:=", ip(w1, 1), _
        "Phase:=", "0deg")
  Next
Next
```

To process the data for introducing in the Excelsheet to continue the calculations:

```
'''''''''''''''''''''''''''''''''''''''''''
' Maxwell Vbs created by PExprt Version 7.0.20
' Copyright UPM-SAS IP, Inc. 1992-2010
' '''''''''''''''''''''''''''''''''''''''''''
Dim oAnsoftApp
Dim oDesktop
Dim oProject
Dim oDesign
Dim oEditor
Dim oModule
Dim f, frq(5)
Dim w1, w2
Set oAnsoftApp = CreateObject("AnsoftMaxwell.MaxwellScriptInterface")
Set oDesktop = oAnsoftApp.GetAppDesktop()
oDesktop.RestoreWindow
Set oProject = oDesktop.SetActiveProject("Project2")
Set oDesign = oProject.SetActiveDesign("SourceForMesh")
Set oModule = oDesign.GetModule("FieldsReporter")


frq(0) = 1.0
frq(1) = 5376.0
frq(2) = 21507.0
frq(3) = 48391.0
frq(4) = 537678.0
frq(5) = 1209776.0

For f = 0 To 5
  For w1 = 0 To 1
    For w2 = w1 To 1
      oModule.CalculatorRead "J" + CStr(w1 + 1) + "_" + CStr(f + 1) + ".reg", _
        "Mesh : LastAdaptive", "Fields", _
        Array("Freq:=", "1MHz", _
          "Ipeak1:=", "1A", _
          "Ipeak2:=", "1A", _
          "Phase:=", "0deg")
      oModule.CalculatorRead "J" + CStr(w2 + 1) + "_" + CStr(f + 1) + ".reg", _
```

```
      "Mesh : LastAdaptive", "Fields", _
       Array("Freq:=", "1MHz", _
         "Ipeak1:=", "1A", _
         "Ipeak2:=", "1A", _
         "Phase:=", "0deg")
      oModule.ClcMaterial "Conductivity (cond)", "div"
      oModule.CalcOp "Conj"
      oModule.CalcOp "Dot"
      oModule.CalcOp "Real"
      oModule.EnterVol "AllObjects"
      oModule.CalcOp "Integrate"
      oModule.ClcEval "Mesh : LastAdaptive", _
       Array("Freq:=", "1MHz", _
         "Ipeak1:=", "1A", _
         "Ipeak2:=", "1A", _
         "Phase:=", "0deg")
      oModule.CalculatorWrite "R" + CStr(w1 + 1) + "_" + CStr(w2 + 1) + "_" + CStr(f + 1) + ".reg", _

       Array("Solution:=", "Mesh : LastAdaptive"), _
       Array("Freq:=", "1MHz", _
         "Ipeak1:=", "1A", _
         "Ipeak2:=", "1A", _
         "Phase:=", "0deg")
      oModule.CalcStack "clear"
    Next
   Next
Next

For f = 0 To 5
 For w1 = 0 To 1
  For w2 = w1 To 1
    oModule.CalculatorRead "H" + CStr(w1 + 1) + "_" + CStr(f + 1) + ".reg", _
      "Mesh : LastAdaptive", "Fields", _
      Array("Freq:=", "1MHz", _
        "Ipeak1:=", "1A", _
        "Ipeak2:=", "1A", _
        "Phase:=", "0deg")
      oModule.ClcMaterial "Permeability (mu)", "mult"
      oModule.CalculatorRead "H" + CStr(w2 + 1) + "_" + CStr(f + 1) + ".reg", _
      "Mesh : LastAdaptive", "Fields", _
      Array("Freq:=", "1MHz", _
        "Ipeak1:=", "1A", _
        "Ipeak2:=", "1A", _
        "Phase:=", "0deg")
```
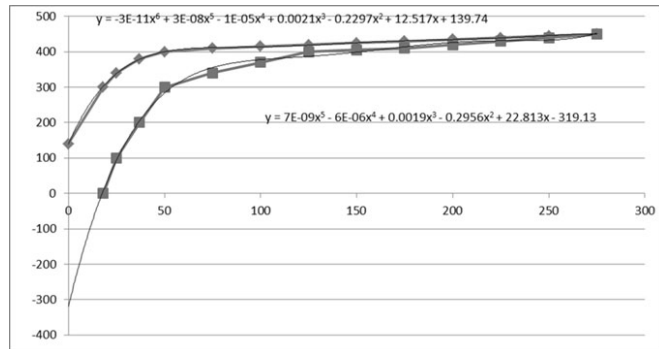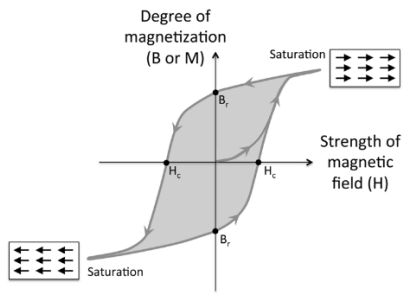
APPENDIX V

Surface Calculation for Hysteresis loop

The data of the hysteresis loop cycles for the material used in the thesis are from the Ferroxcube datasheet [76]. The areas of the hysteresis loop have been calculated with polynomial grade 6 in Excel and performing the according integrals.

APPENDIX VI

Current Impact in HL analysis

The analysis sequences depending on the coil current. The pictures showed represent the behaviour of the HL when the core is saturated. The correlation of HL with core saturated is similar even the current is increased.
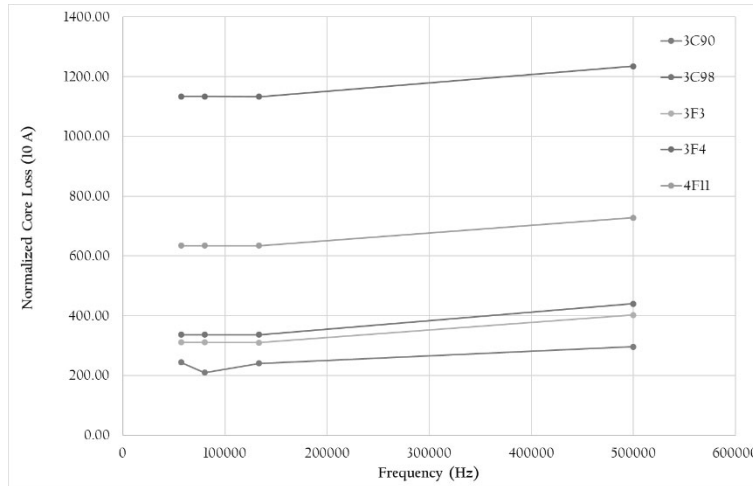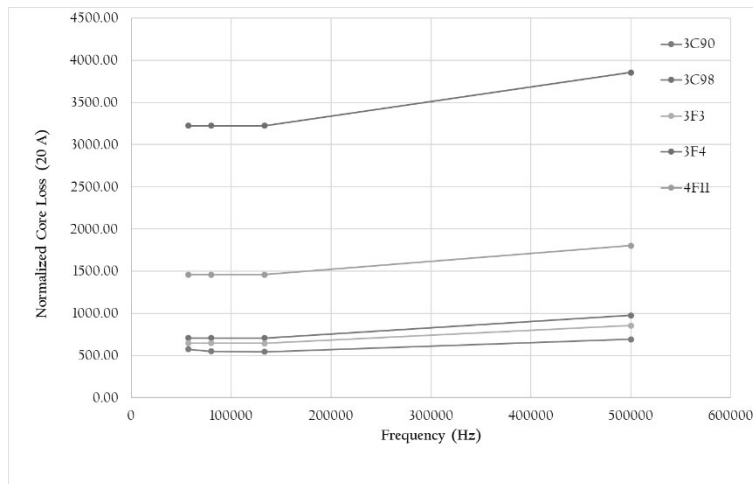

Fig. Appendix VI.1 Current 10 A

Fig. Appendix VI.2 Current 20 A

UNIVERSIDAD DE EXTREMADURA